Amphiphilic Block Copolymer Micelles: Creation of Functional Nanocavities and Their Use as Nanocontainers for Controlled Release

by

ANDREW CRAIG MILLER

B.S., Chemical Engineering
University of Illinois, 2003

Submitted to the Department of Chemical Engineering
in partial fulfillment of the requirements for the degree of

DOCTOR OF PHILOSOPHY IN CHEMICAL ENGINEERING

at the

MASSACHUSETTS INSTITUTE OF TECHNOLOGY

August 2008

Signature of Author: ______________________________
Department of Chemical Engineering
August 13, 2008

Certified by: ______________________________
Robert E. Cohen
Professor of Chemical Engineering
Thesis Supervisor

Certified by: ______________________________
Paula T. Hammond
Professor of Chemical Engineering
Thesis Supervisor

Certified by: ______________________________
Darrell J. Irvine
Professor of Materials Science and Engineering and Biological Engineering
Thesis Supervisor

Accepted by: ______________________________
William M. Deen
Professor of Chemical Engineering
Chairman, Committee for Graduate Students

Amphiphilic Block Copolymer Micelles: Creation of Functional Nanocavities and Their Use as Nanocontainers for Controlled Release

by

Andrew Craig Miller

Submitted to the Department of Chemical Engineering on August 14, 2008 in partial fulfillment of the requirements for the degree of Doctor of Philosophy in Chemical Engineering

ABSTRACT

Block copolymers in solution can self-assemble in to a variety of morphologies, with features on the nanometer length scale. This has lead to significant recent research into this assembly process and a wide range of potential applications. The exchange of block copolymer molecules between micelles and solution is very slow compared to the exchange kinetics observed for low molecular weight surfactant micelles. A favorable result of these slow exchange kinetics is the ability to retain a micellar morphology during casting from selective solvents onto solid substrates; this morphology becomes kinetically trapped in the final thin film upon solvent evaporation, even in cases for which the copolymer composition would suggest a transition to a different equilibrium heterogeneous phase. Control of the structural parameters of the micellar thin films, including micelle core size, micelle corona size and distance between adjacent micelle cores is important for thin film applications.

Here we demonstrate the ability to control these structural parameters using polystyrene-block-poly(acrylic acid) (PS-*b*-PAA) as a model block copolymer system that assembles into spherical micelles in toluene. Several strategies were employed: varying the block copolymer molecular weight, adding PS homopolymer into the micellar solution, and also by the combination of different micellar solutions. Patterning of micelle films on the micron length scale is accomplished via two PDMS stamp-based soft lithographic techniques.

PS-*b*-PAA spherical micelle thin films cast from toluene can undergo rearrangement upon exposure to solvents selective for the PAA block. The solvent swells the PAA micelle core and ruptures the glassy PS corona, a process we termed cavitation. Here we have investigated the conditions required for this cavitation process to occur and the end-state polymer morphology of close-packed films of PS-*b*-PAA micelles following treatment with a series of short alkyl chain alcohols or aqueous solutions of varying pH and ionic strength. In addition to the effects of solvent conditions, we show that the cavitation process is influenced by the molecular weight of the PS block and is thermally reversible. Following cavitation, the nanopatterned regions of exposed PAA are available for conjugation chemistry, demonstrated here through selective linking of a fluorescently labeled protein. Cavitation was also observed in polystyrene-*block*-poly(2-vinyl pyridine) (PS-*b*-P2VP) spherical and cylindrical micelles.

Biocompatible oils are used in a variety of medical applications ranging from vaccine adjuvants to vehicles for oral drug delivery. To enable such nonpolar organic phases to serve as reservoirs for delivery of hydrophilic compounds, we explored the ability of block copolymer micelles in organic solvents to sequester proteins for sustained release across an oil-water interface. Self-assembly of the block copolymer, poly(ε-caprolactone)-*block*-poly(2-vinyl pyridine) (PCL-*b*-P2VP), was investigated in toluene and oleic acid, a biocompatible naturally-occurring fatty acid. Micelle formation in toluene was characterized by dynamic light scattering (DLS) and atomic force microscopy (AFM) imaging of micelles cast onto silicon substrates. Cryogenic transmission electron microscopy confirmed a spherical morphology in oleic acid. Studies of homopolymer solubility implied that micelles in oleic acid consist of a P2VP corona and a PCL core, while P2VP formed the core of micelles assembled in toluene. The loading of two model proteins (ovalbumin (ova) and bovine serum albumin (BSA)) into micelles was demonstrated with loadings as high as 7.8 % wt of protein per wt of P2VP in oleic acid. Characterization of block copolymer morphology in the two solvents after protein loading revealed spherical particles with similar size distributions to the as-assembled micelles. Release of ova from micelles in oleic acid was sustained for 30 hours upon placing the oil phase in contact with an aqueous bath. Unique to the situation of micelle assembly in an oily phase, the data suggest protein is sequestered in the P2VP *corona* block of PCL-*b*-P2VP micelles in oleic acid. More conventionally, protein loading occurs in the P2VP *core* of micelles assembled in toluene.

Thesis Supervisors:	Robert E. Cohen St. Laurent Professor of Chemical Engineering
	Darrell J. Irvine Eugene Bell Associate Professor of Tissue Engineering
	Paula T. Hammond Bayer Chair Professor of Chemical Engineering

ACKNOWLEDGEMENTS

There are many people that deserve the utmost thanks for their friendship, advice, and support during my time at MIT. Without each of you I would not have been able to accomplish the work described here.

First, I would like to thank my advisors, Prof. Robert E. Cohen, Darrell J. Irvine and Paula T. Hammond. Prof. Cohen has been a constant source of encouragement and his genuine excitement for research has been a source of inspiration. Prof. Irvine has been a very dedicated advisor and has pushed my research in new directions. Prof. Hammond always has a new viewpoint from which to look at things. Having three research advisors can appear challenging, but I have benefited greatly from having access to each of my advisors. Their ability to work together has been paramount to my success. Thank you for your time and support. I would also like to thank my thesis committee members, Linda G. Griffith and K. Dane Wittrup. My work has benefited from their time and suggestions.

I have had the pleasure of working directly with many other graduate and undergraduate students in the past 5 years. I thank each of you for working with me and I would like to thank a few people specifically: Ryan Bennett, for helping me when I was just a fledgling graduate student to get my research off the ground; Naomi Kohen, who took time during her hectic undergraduate schedule to do some insightful research; Xingfang Su, for doing mouse skin experiments on a short time line so I could take one more step to finishing my thesis and Anna Bershteyn, without your tireless efforts on the cryoTEM, I would still be doing experiments right now. I have had numerous helpful interactions with many people over the years, ranging from a question during a group meeting talk to running some samples for me. For that I would like to thank Eric Verploegen, Ryan Waletzko, Byeong-Su Kim, Jodie Lutkenhaus, Sanjoy Sircar, Eric Williamson, Heejae Kim, Ben Wang, Adam Nolte, Daeyeon Lee, Shujun Chen, Amanda Engler, Kevin Krogman, Maria Foley, Yana Wang, and Junsang Doh. Unfortunately, I am sure I have left many off of this list.

I have made many friendships here at MIT that have made my time here enjoyable and given me memories that I will take with me forever. I could not possibly thank each you of here.

My family is foundation that has allowed me to be where I am today. I thank my parents, Dennis and Kay for supporting me, encouraging me and giving me the opportunity to pursue my interests. I thank my brothers, Eric and Doug, and Sister-in-law Sarah who were there when I needed to talk and encouraged me with their own successes. And my grandparents, Ralph and Arlene, for being an example of what you can become in life. I would also like to thank my new family; Rose, Peter, Becky, and Gerard for welcoming me into their family and making me feel like a part of it.

Finally, I would like to thank my wife, Michelle. I could not have accomplished this without her love and support. She has given me times where MIT seemed infinitely far away, but also told me to do work when I need to work. She has always been at my side and I look forward to sharing the rest of our lives together.

Table of Contents

List of Figures

List of Tables

Chapter 1 INTRODUCTION AND BACKGROUND

1.1. Block Copolymers and Their Micelles

Diblock copolymers are macromolecules consisting of two polymer chains made of different repeat units, covalently coupled to each other at a single jointing point. This covalent junction and the different chemical nature of the two blocks leads to the ability to self-assemble in to a variety of morphogies. The length scale of these ordered morphologies matches the length scale of the polymer chains themselves, which generally range from 1-100 nm. Multiblock copolymers and branched architectures formed from when more than two chains coming together at a single jointing point, further enrich the ordered structures that can be formed.

These morphologies can be formed in the bulk polymer state or in solution. Block copolymer solution behavior depends not only on the interaction between the two polymer blocks, but also on their interaction with the solvent. If the solvent is selective for one block, order structures will be formed with this polymer block on the exterior of the structure, and the other block on the interior, 'protected' from the solvent. If one block is hydrophobic and the other hydrophilic, the copolymer is referred to as amphiphilic. This assembly is driven by enthalpic forces, as it is entropically unfavorable to form these ordered structures.[1] The exchange of block copolymer molecules between micelles and solution is very slow compared to the exchange kinetics observed for low molecular weight surfactant micelles.[2] Block copolymer also exhibit lower critical micelle concentration compared to low molecular weight surfactants.[2] A favorable result of these slow exchange kinetics is the ability to retain a micellar morphology during casting from volatile selective solvents onto solid substrates; this morphology becomes kinetically trapped in the final thin film upon solvent evaporation, even in cases for which the copolymer composition would suggest a transition to a different equilibrium heterogeneous phase. Because these structures are often kinetically trapped, this allows the opportunity to vary structural parameters such as the characteristic shape, size, and spacing of the array features.

1.2. Ultrathin Block Copolymer Micellar Thin Films

Due to their inherent nanometer length scale and the ability to control structural parameters, ultrathin block copolymer micellar thin films have been investigated for a applications including including data storage,[3] nanolithography,[4-12] and deposition of metal nanoparticle arrays such as gold catalyst particle arrays for zinc oxide nanowire synthesis,[13] iron oxide nanoparticles for carbon nanotube synthesis[14] and magnetic applications,[15] zinc oxide nanoparticles for optical devices[16] and nickel[17] or gold[18-20] arrays for protein binding. These applications have focused on the ability of amphiphilic block copolymers in organic solvents to sequester metal salts, which can subsequently be reduced to metal nanoclusters and act as lithographic masks, catalysts, or electromagnetic particles.

Each polymer block contains a distinct chemical functionality, which in the above applications is used to selectively load metal ions. Another approach would be to create functionalized films patterned on the nanometer length scale by selectively coupling molecules to one polymer block. One potential stepping stone to this approach was previously demonstrated in our lab by Boontongkong[21] using the PS-*b*-PAA block copolymer system. A PS-*b*-PAA polymer with PS and PAA block molecular weights of

M_n = 16 400 g/mol and M_n = 4 500 g/mol respectively formed kinetically trapped spherical inverse micelles in toluene after a suitable heating and cooling cycle described earlier,[21] which were then spin-cast onto a planar substrate to create a quasi-hexagonal array of PS-*b*-PAA micelles. When films of PS-*b*-PAA were exposed to highly alkaline aqueous solutions with monovalent cations, the PAA domains swelled and ruptured the glassy PS corona, a process we termed cavitation. This presumably exposes the carboxylic acid groups to solution and would allow for their functionalization.

1.3. Control over Size, Spacing and Patterning of Block Copolymer Micelle Thin Films

For the applications of micelle thin films listed above, the ability to control the structural parameters of the film, including micelle core size, micelle corona size and distance between adjacent micelle cores is essential. In chapter 2 we demonstrate the ability to control these structural parameters using PS-*b*-PAA as a model block copolymer system with a variety of strategies: varying the block copolymer molecular weight, adding homopolymer of PS into the micellar solution, combining of different micellar solutions and casting from dilute solutions. These afford control of the micelle film parameters on the nanometer length scale. The ability to pattern micelle films on the micron length scale could also be of potential use for certain applications such as creating functionalized surfaces for cell attachment where patterning the micellar film on cellular length scale could be desired.

Soft lithography[22-25] is a technique that relies on using an elastomeric polymer to replicate a hard master, has emerged successfully as a fast, inexpensive, and straightforward route for patterning substrates.[26] We demonstrate the use of two soft lithographic techniques to pattern PS-*b*-PAA micelle films in chapter 2.

1.4. Cavitation and the Creation of Functional Nanocavities

Building on the cavitation phenomena demonstrated by Boontongkong,[21] we studied this rearrangment process in detail in chapter 3. AFM imaging was used to determine the effect of a series of alkyl-alcohcols, pH and ionic strength of aqueous solutions and block copolymer molecular weight on cavitation. Visualization of PAA chain rearrangement was also demonstrated using TEM. This rearrangement was shown to be reversible upon thermal annealing. As mentioned above, micelle thin films could be used as template for creation of patterned 2-D arrays via selective functionalization of one polymer block. We selectively functionalize the PAA domains of PS-*b*-PAA thin films using EDC chemistry with a biotin linker molecule and subsequently, the protein streptavidin. This confirms the availability of the carboxylic acid moieties of the PAA domains to post-cavitation chemistry. Combining this with the work in chapter 2 demonstrates the potential of this copolymer micelle system to pattern a variety of molecules using straight-forward conjugation chemistry and control of the size and spacing of conjugated groups on the nanometer and micron length scale.

1.5. Block Copolymer Micelles as Nanocontainers for Controlled Release

Block copolymers have been investigated for drug delivery applications for several reasons, including (1) the capacity to solubilize molecules in solvents in which they would be otherwise insoluble, (2) the polymer's ability to protect the therapeutic molecule from environmental conditions, and (3) that ligands can be directly attached to the polymer to provide tissue targeting. This approach has been extensively studied for water soluble copolymer assembly encapsulating small molecule therapeutics.[27-30] Micellar systems assembled in organic solvents have been used as carriers of hydrophilic molecules. Micelles formed in biocompatible oil phases could be of interest in biomedical applications as carriers for therapeutic molecules, imaging agents, or vaccine adjuvants. However, very few studies of micelle systems in biocompatible oil phases for drug delivery have been reported.

In Chapter 4 we focused on micelles formed from a block copolymer system poly(ε-caprolactone)-*block*-poly(2-vinyl pyridine) (PCL-*b*-P2VP), containing a biodegradable hydrophobic block (PCL) and a pH responsive block (P2VP). We examined micelle assembly in two different oil phases, toluene (as a model volatile nonpolar solvent) and oleic acid, a naturally occurring fatty acid. Oleic acid is biocompatible oil used in oral drug delivery,[31-36] buccal delivery,[37] transdermal drug delivery,[38-41] and as a vaccine adjuvant.[42] We characterized the assembly of PCL-*b*-P2VP micelles observing different micellar structures in the two solvents. In toluene, the micelles consist of P2VP cores with PCL corona, while in oleic acid our results suggest PCL blocks are in the micelle core with P2VP forming the corona. Two proteins, ovalbumin (ova) and bovine serium albumin (BSA), were loaded into the organic phase micelles and the release of ova from PCL-*b*-P2VP micelles when put into contact with an aqueous reservoir was investigated. These results highlight the potential of block copolymers as carriers for sustained release of hydrophilic drug cargos from biocompatible oils.

Chapter 2 STRATEGIES FOR CONTROLLING THE SIZE, SPACING AND PATTERNING OF INVERSE MICELLAR THIN FILMS

2.1. Planar Arrangement of Inverse Micellar Thin Films on the Nanometer length Scale

2.1.1. Introduction

In the past decade, the use of self-assembling systems for the fabrication of materials on the nanometer scale has been an active area of research,[43] with possible applications in areas such as data storage, electronics, and molecular separation.[4] Block copolymers thin films are nanoscale self-assembling systems[7, 44-48] that have been exploited due to their intrinsic nanometer feature size, their ease of synthesis, and their rich phase behavior.[49, 50] Block copolymer lithography[7] is an example that uses the heterogeneous morphology of block copolymer thin films to transfer periodic arrays of features onto a substrate on a nanometer length scale. Generally, solvent cast block copolymer films are annealed on the substrate to generate an equilibrium morphology and to reduce the occurrence of unwanted grain boundaries and other defects.

A related but different route for patterning on the nanoscale employes amphiphilic block copolymer micellar solutions to produce ultrathin nanostructured films. These micellar systems, frequently based on poly(styrene-*block*-X- vinylpyridine) (X = 2 or 4), have been utilized for various applications, including nanolithography based on gold-loaded micelles,[51] deposition of gold nanocluster arrays for ZnO nanowire growth[13] and protein binding,[52] deposition of ZnO nanoclusters arrays for optical devices,[16] and deposition of iron oxide nanocluster arrays for carbon nanotube growth[14] and magnetic applications.[15] Work in our research group used block copolymer micellar thin films based on poly(styrene-*block*-acrylic acid) to create arrays of PAA domains that could be cavitated to expose free carboxylic acid groups.[21] These systems have also been used to generate planar arrays of various inorganic nanoclusters,[21] including iron oxides suitable for catalyzing carbon nanotube growth.[53, 54] One advantage of the micellar route to generate such planar nanoarrays arises from the fact that these systems are often trapped in a nonequilibrium state, facilitating the opportunity to vary structural parameters such as the characteristic shape, size, and spacing of the array features.

In this chapter, we focus on strategies to vary the size and spacing of spherical block copolymer micellar domains on planar surfaces as well as routes that allow for nanocluster synthesis within the spherical domains. Our specific approach capitalizes on the ability of the amphiphilic block copolymer, poly(styrene-*block*-acrylic acid) (PS/PAA), to form quasi-hexagonal planar arrays of PAA spheres in a matrix of PS. As shown previously,[21, 53] it is possible to exploit the metal-binding properties of the carboxylic acid groups in chemical synthesis schemes that are confined to nanometer-scale reaction zones. By cavitating the micelles and exposing the carboxylic acid groups to solution, this opens up another potential functional handle for these nanoscale reaction zones. Application of these nanoreactor synthesis protocols ideally requires a measure of control over the size, spacing, and packing arrangement of these reaction zones on the planar substrate. The present work addresses some of these issues using a variety of strategies, including varying the block copolymer molecular weight, adding homopolymer of PS into the micellar solution, and also by the combination of different micellar solutions. For ease of characterization we utilized transmission electron microscopy (TEM) to study and quantify the effects of the variations of the micellar solutions on the resulting metal nanocluster arrays. In some cases, atomic force microscopy (AFM) is used to confirm our TEM results.

2.1.2. Experimental Section

2.1.2.1. Materials

Poly(styrene-*block*-acrylic acid) (PS-*b*-PAA) (M_n (PS) = 16 400 g/mol, M_n (PAA) = 4 500 g/mol, PDI = 1.05), PS-*b*-PAA (M_n (PS) = 66 500 g/mol, M_n (PAA) = 4 500 g/mol, PDI = 1.07), and PS-*b*-PAA (M_n (PS) = 11 000 g/mol, M_n (PAA) = 1 200 g/mol, PDI = 1.11), Poly(ε-caprolactone)-*block*-poly(2-vinyl pyridine) (PCL-*b*-P2VP) (M_n (PCL) = 35 400 g/mol, M_n (P2VP) = 20 900 g/mol, PDI = 1.8), Poly(styrene-*block*-2-vinyl pyridine) (PS-*b*-P2VP) (M_n (PS) = 55 000 g/mol, M_n (P2VP) = 50 000 g/mol, PDI = 1.11), and Polystyrene (PS) (M_n = 8 500 g/mol, PDI = 1.06) were purchased from Polymer Source, Inc along with their molecular characterization data. The following chemicals were also used as received: anhydrous iron(III) chloride ($FeCl_3$) obtained from Sigma-Aldrich Co., lead(II) acetate trihydrate ($PbAc_2$) obtained from Sigma-Aldrich Co., sodium hydroxide (98.9%) obtained from Mallinckrodt, and toluene (HPLC grade, 99.8%) obtained from Sigma-Aldrich Co. The silicon nitride membrane window substrates were purchased from Structure Probe, Inc. Each substrate (surface area ~ 4.5 mm^2) consisted of a 100-nm-thick amorphous, low-stress Si_3N_4 membrane supported on a 0.2-mm-thick silicon wafer that had been back-etched in the center to create the electron transparent Si_3N_4 window (surface area ~ 0.2 mm^2). The use of the electron-transparent silicon nitride substrates allows for direct TEM characterization without disturbing the spin-cast films. Each substrate was rinsed with toluene prior to film casting. All aqueous solutions were made using deionzed water (> 18 MΩ cm, Millipore Milli-Q).

2.1.2.2. Sample Preparation

To produce the micellar arrays, we employed a variety of synthesis procedures that capitalize on the micellar organization of PS-*b*-PAA in toluene solution. A summary of the processing routes is shown in Figure 2-1 and outlined below.

In route i, three different molecular weights of PS-*b*-PAA (listed in the Materials section) were mixed with toluene at a concentration of 12.5-15 mg/mL. For the case of PS-*b*-PAA (16.4-*b*-4.5), the solution initially appeared slightly cloudy. After heating this solution to 145 °C for 20 min, the solution became optically clear, and it remained clear after cooling to room temperature. Previous work[21] has shown that this transition in solution optical properties is the result of a change from (equilibrium) cylindrical to (kinetically trapped) spherical block copolymer micelles. For the case of PS-*b*-PAA (11.0-*b*-1.2) and PS-*b*-PAA (66.5-*b*-4.5), the same heating and cooling procedure was followed, and optically clear final solutions were obtained. The as-prepared solutions for these two copolymers were much less cloudy than the initial PS-*b*-PAA (16.4-*b*-4.5) solution. The PAA micelle cores were selectively loaded with the chosen metal by adding the metal species to the micellar solution at a ratio of 5.4 metal ion equivalents per carboxylic acid group (metal loading ratio). Thin films were then created by spincasting the metal-loaded micellar solutions onto the planar substrates at between 6000 and 8000 rpm for 1 min at room temperature. Dilute solutions (1 mg/mL, 0.1 mg/mL, 0.01 mg/mL) of PS-*b*-PAA 16.4-*b*-4.5 were also used to create micellars film spin cast at

1600 rpm to determine the effect of varying the solution concentration on micelle spacing.

In route ii, PS-*b*-PAA (16.4-*b*-4.5) was mixed with toluene at a concentration of 12.5-15 mg/mL. The chosen metal was then added to the micelle solution to load metal ions into the micelle core. Thin films of each solution were then produced by spin-casting the solution onto the substrates.

In route iii, PS homopolymer (M_n = 8500 g/mol) was added to the micellar solutions (metal loading ratio 5.4) based on the PS-*b*-PAA (16.4-*b*-4.5) system. Homopolymer was added in quantities leading to solutions in which the molar ratio of molecules of PS homopolymer to PS-*b*-PAA block copolymer [PS: PS-*b*-PAA] was equal to 4 and 10, respectively. To reduce the viscosities of these solutions to acceptable levels for spin-casting, the solutions were diluted with toluene from 13 mg of PS-*b*-PAA/mL in toluene to 5 mg of PS-*b*-PAA/mL in toluene. Thin films were then produced by spin-casting these solutions onto substrates.

In route iv, metal-loaded micellar solutions were combined with either an unloaded micellar solution (micelle solution that bypassed the metal loading step) or a micelle solution that had been loaded with a different metal species. In the first example, a micelle solution of PS-*b*-PAA (16.4-*b*-4.5) with a metal loading ratio of 5.4 was mixed in a 1:1 volume ratio with an unloaded micelle solution of the same PS-*b*-PAA copolymer. After the combined solutions had been mixed for 15 sec, a thin film was spin-cast onto a substrate. In the second example, micelle solution loaded with different metal species could be mixed and then spin cast onto the substrate. These results are not included here but are published elsewhere.[55]

In each of the routes above, there exists the possibility of bypassing the metal loading step (step ii in Figure 2-1) to create arrays of PAA domains within a PS matrix. From previous research it is known that treating these films in a basic solution containing a monovalent cation results in significant swelling of the PAA domains,[21] which eventually leads to localized cavitation that exposes the interior of the PAA domains to the surface. This process is investigated in detail in Chapter 3.

In each of the routes listed above, the polymer thin film may be removed by oxygen plasma etching (rf plasma, 8-12 MHz) for 15 min, leaving only the inorganic species remaining on the substrate. The inorganic nanocluster arrays were then characterized using TEM and atomic force microscopy (AFM).

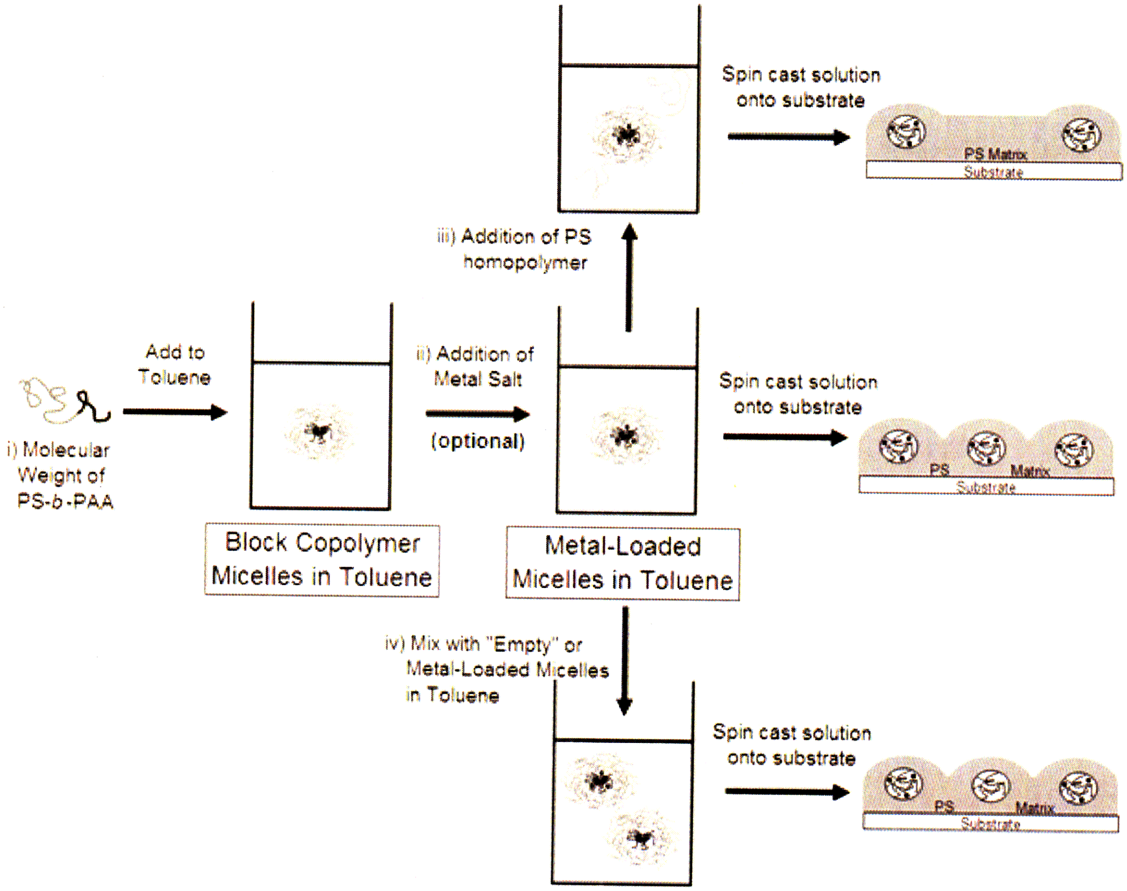

Figure 2-1: Diagram of synthesis procedures for modification of block copolymer micellar thin films.

2.1.2.3. Microscopy

TEM was performed on a JEOL 200CX operating at 200 kV and a JEOL 2000FX operating at 200 kV. AFM was performed on a Digital Instruments Dimension 3000 Nanoscope IIIA scanning probe microscope operating in tapping mode using a silicon cantilever. Dynamic light scattering (DLS) was performed on a BI-9000AT digital autocorrelator (Brookhaven Instruments Corp.) using a 514 nm laser, at $\theta = 90°$ and a temperature of 25 °C.

2.1.3. Results and Discussion

2.1.3.1. Variation of PS-*b*-PAA Molecular Weight

The TEM images in Figure 2-2A through C demonstrate the effect of the molecular weight of PS-*b*-PAA on the size and spacing of the PAA domains, and consequently on the size and spacing of metal nanoclusters formed. In Figure 2-2A, micelles formed from PS-*b*-PAA (M_n (PS) = 11 000 g/mol, M_n (PAA) = 1 200 g/mol) with a $FeCl_3$ loading ratio of 1.7 were used to create iron oxide nanoclusters with diameters of 4.7 ± 0.6 nm, center-to-center spacings of 12 – 15 nm, and an areal density of approximately 3×10^{11} nanoclusters per cm^2. In Figure 2B, micelles formed from PS-*b*-PAA (M_n (PS) = 16 400 g/mol, M_n (PAA) = 4 500 g/mol) with a $FeCl_3$ loading ratio of 1.7 were used to create iron oxide nanoclusters with diameters of 16 ± 1.6 nm, center-to-center spacings of approximately 45 ± 4 nm, and an areal density of approximately 6×10^{10} nanoclusters per cm^2. As expected, similar to results we have observed for metal nanocluster arrays created from different metal loading ratios,[55] decreasing the molecular weight of the PAA segment while also decreasing the molecular weight of the PS segment causes a decrease in the diameter of the resulting metal nanoclusters and a reduction in the center-to-center spacing. In Figure 2-2C, micelles formed from PS-*b*-PAA (M_n (PS) = 66 500 g/mol, M_n (PAA) = 4 500 g/mol) with a $FeCl_3$ loading ratio of 1.7 were used to create iron oxide nanoclusters with diameters of 11 ± 1.1 nm, center-to-center spacings of approximately 57.6 ± 8.2 nm, and an areal density of approximately 4.3×10^{10} nanoclusters per cm^2. Results from Figure 2-2B and C show that the diameter of the nanoclusters decreases approximately 30% by increasing the PS segment molecular weight. We believe that this decrease in nanocluster diameter is an effect of the decrease in the aggregation number of the micelles, which is a steric effect caused by the increased size of the PS segment in the shell of the micelles.[17] The results from Figure 2-3B and C also demonstrate that by increasing the PS segment of the block copolymer four-fold, the center-to-center spacing of the PAA domains in the thin film is increased by approximately 30%, although this increase is not as significant as first expected. This can also be explained by the decrease in aggregation number of the micelles caused by the PS segment increasing from 16 400 g/mol to 66 500 g/mol. The decreased aggregation number of the micelles leads to a lower density of PS segments per volume in the shell of the micelle, so as the toluene evaporates the center-to-center spacing of the PAA domains becomes shorter than would be expected by comparing hydrodynamic radii. The three TEM images in Figure 2-2 demonstrate a method for controlling the size and spacing of the PAA micellar domains, which leads to control over the size and spacing of metal nanocluster arrays, as summarized in Table 2-1.

The variation of center-to-center spacing between the metal nanoclusters caused by the alteration of the block copolymer molecular weight was verified using DLS. An average hydrodynamic radius of each micellar solution was measured and is shown in Table 2-2. As expected, the micelles formed from PS-*b*-PAA (M_n (PS) = 11 000 g/mol, M_n (PAA) = 1 200 g/mol) have the smallest hydrodynamic radius ($R_h \sim 27$nm), which is roughly two times the measured center-to-center spacing of the PAA domains for this system. The micelles formed from PS-*b*-PAA (M_n (PS) = 16 400 g/mol, M_n (PAA) = 4 500 g/mol) have a hydrodynamic radius of 44 nm, which is similar to the measured center-to-center spacing for this system. The micelles formed from PS-*b*-PAA (M_n (PS) = 66 500 g/mol, M_n (PAA) = 4 500 g/mol) have a hydrodynamic radius of 96 nm, which is nearly two times the measured center-to-center spacing of 57.6 nm for this system. A key feature of these block copolymer micelles is the ratio of the molecular weights of the PS segment and the PAA segment. Depending on this ratio, four different regimes of micellar behavior were proposed by Zhulina and Birshtein.[18] A scaling relationship for the total micellar radius, specific to the regime where micelles have corona segments much longer than core segments, was later developed by Halperin.[19] This scaling relationship shows that the total micellar radius (R) scales as $(N_{PAA})^{4/25}$ $(N_{PS})^{3/5}$, where N_{PAA} denotes the number of repeat units of the PAA segment, and N_{PS} denotes the number of repeat units of the PS segment. Our hydrodynamic radius data from DLS agrees very closely with the scaling relationship from Halperin. It should be noted that although we have seen good agreement with the scaling relationship of Halperin, his scaling theory predicts that the aggregation number and the core radius of the micelles should be independent of the PS segment length in this regime. In the previous paragraph, we demonstrated a decrease in the size of the core radius by increasing the PS segment length while keeping the PAA segment length constant. We believe this discrepancy is due to the micelles formed from PS-*b*-PAA (M_n (PS) = 16 400 g/mol, M_n (PAA) = 4 500 g/mol) not meeting all the conditions required for this regime, namely that $N_{PS} >> N_{PAA}$ doesn't hold for this molecular weight block copolymer.

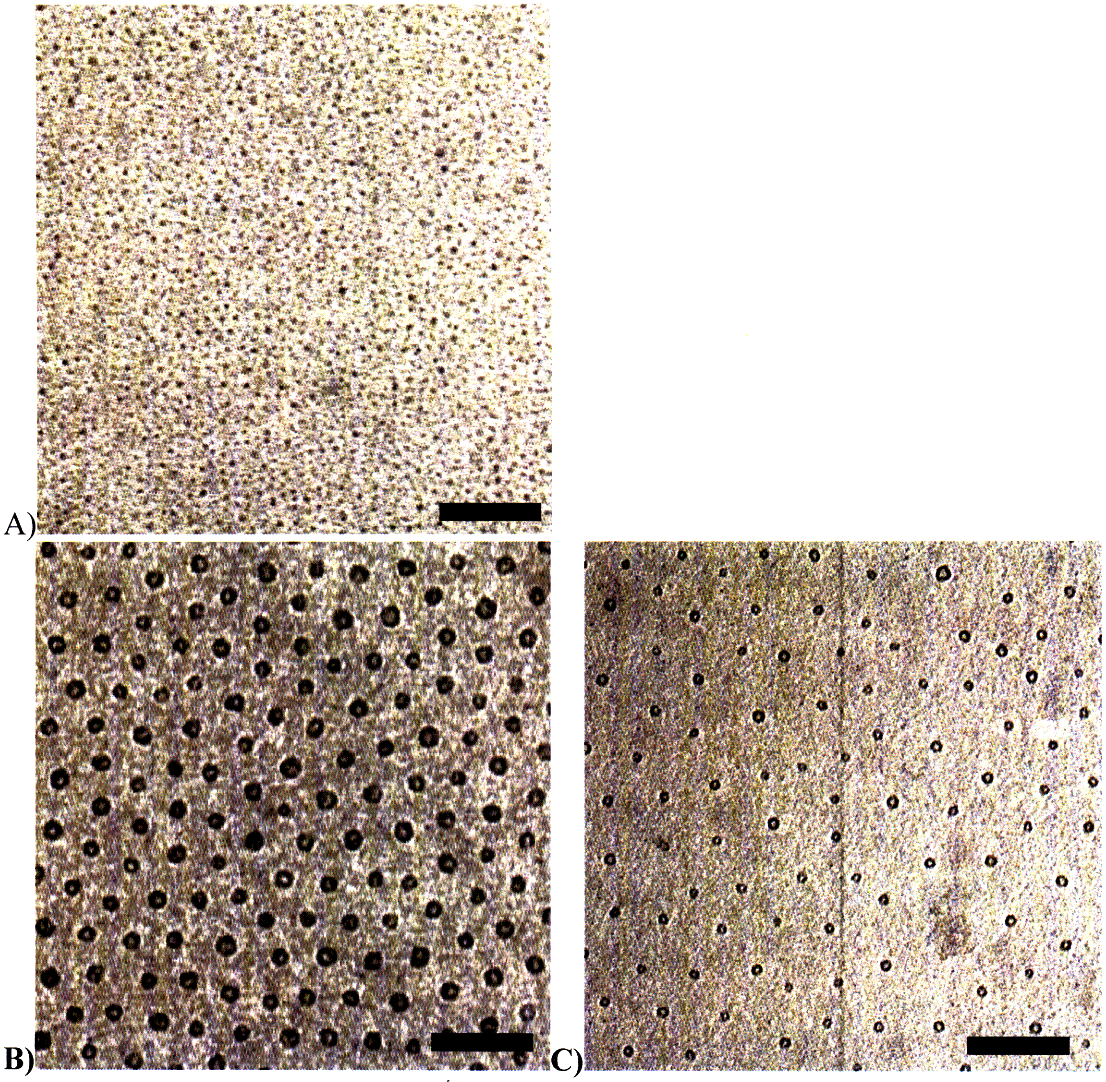

Figure 2-2: TEM images of iron oxide nanocluster arrays synthesized from micellar thin films with a metal loading ratio of 1.7 and PS-b-PAA with a molecular weight of: (A) M_n (PS) = 11 000 g/mol, M_n (PAA) = 1 200 g/mol; (B) M_n (PS) = 16 400 g/mol, M_n (PAA) = 4 500 g/mol; (C) M_n (PS) = 66 500 g/mol, M_n (PAA) = 4 500 g/mol. Scale bar = 100 nm.

PS	PAA	Hydrodynamic Radius (R_h)	Diameter	C-to-C spacing		Spatial Density
				(Measured)[a]	(FFT)[b]	
(g/mol)	(g/mol)		(nm)	(nm)	(nm)	(part/cm^2)
11 000	1 200	27 nm	4.7 ± 0.6	13 ± 1.7	12	3.0E+11
16 400	4 500	44 nm	16.0 ± 1.6	44.9 ± 4.0	39.5	6.0E+10
66 400	4 500	96 nm	11.2 ± 1.1	57.6 ± 8.2	56	4.3E+10

Table 2-1: Effect of varying the molecular weight of PS-b-PAA on diameter, center-to-center spacing, and spatial density of iron oxide nanocluster arrays.

[a]Physically measured from TEM images. [b]Determined from Fast Fourier Transfrom (FFT) of TEM image.

From the TEM images in Figure 2-2, it is apparent that the nanoclusters have a higher contrast around the exterior and considerably less contrast within the center of the nanocluster. We feel confident that this effect is caused by phase contrast in TEM imaging and is not representative of the actual structure of our nanoclusters. Because these nanoclusters offer very little amplitude contrast, we are forced to take steps to increase the contrast in order to produce useful images. We accomplish this by underfocusing our sample in order to image the nanoclusters using phase contrast. When the nanoclusters are overfocused, the center of the nanoclusters appears dark and the exterior appears bright, which is a common indicator of phase contrast effects. When the nanoclusters are in focus, this effect is eliminated, but the images are extremely difficult to view due to the lack of contrast. This explanation is also confirmed by the annular dark field (ADF) image of the nanoclusters (images shown here[55]). If the nanoclusters were hollow, we would observe a bright ring with a dark center for each nanocluster in the ADF image; however, it is clear from the ADF image that each nanocluster appears as a uniform bright circle. We also imaged these nanoclusters using AFM (image not shown), which confirmed that the nanoclusters were approximately spherical in shape and did not contain a cavity as the TEM images in Figure 2-2 might suggest.

2.1.3.2. Addition of PS homopolymer to PS-*b*-PAA Micellar Solutions

Although the spatial density of the PAA domains can be controlled through the variation of molecular weight (as shown in Figure 2-2), there is an unavoidable coupling of areal density with the size of the nanoclusters. Therefore, a more general approach allowing independent control of these two parameters was sought. By adding PS homopolymer (M_n (PS) = 8 500) to our micellar solution, as illustrated in route iii) of Figure 2-1, we were able to vary the spatial density over an order of magnitude, as demonstrated in the TEM images in Figure 2-3. In all the TEM images in Figure 2-3, the molecular weight of PS-*b*-PAA (M_n (PS) = 16 400 g/mol, M_n (PAA) = 4 500 g/mol) and the $FeCl_3$ loading ratio (~ 1.7) are kept constant. In Figure 2-3A, no PS homopolymer was added to the solution, and a spatial density of 6 x 10^{10} particles per cm^2 was achieved. In Figure 2-3B, PS homopolymer was added to the micellar solution at a ratio of 4 molecules of PS homopolymer per molecule of PS-*b*-PAA block copolymer ([PS : PS-*b*-PAA] = 4). This addition of PS homopolymer decreased the spatial density by 83% to 1.1 x 10^{10} particles per cm^2. By further increasing the PS homopolymer to block copolymer ratio ([PS : PS-*b*-PAA] = 10), as shown in Figure 2-3C, the spatial density was decreased by another 41% to 6.5 x 10^{10} particles per cm^2. Comparing the results, which are shown in Table 2-2, show that the addition of PS homopolymer was able to vary the spatial density over nearly an order of magnitude.

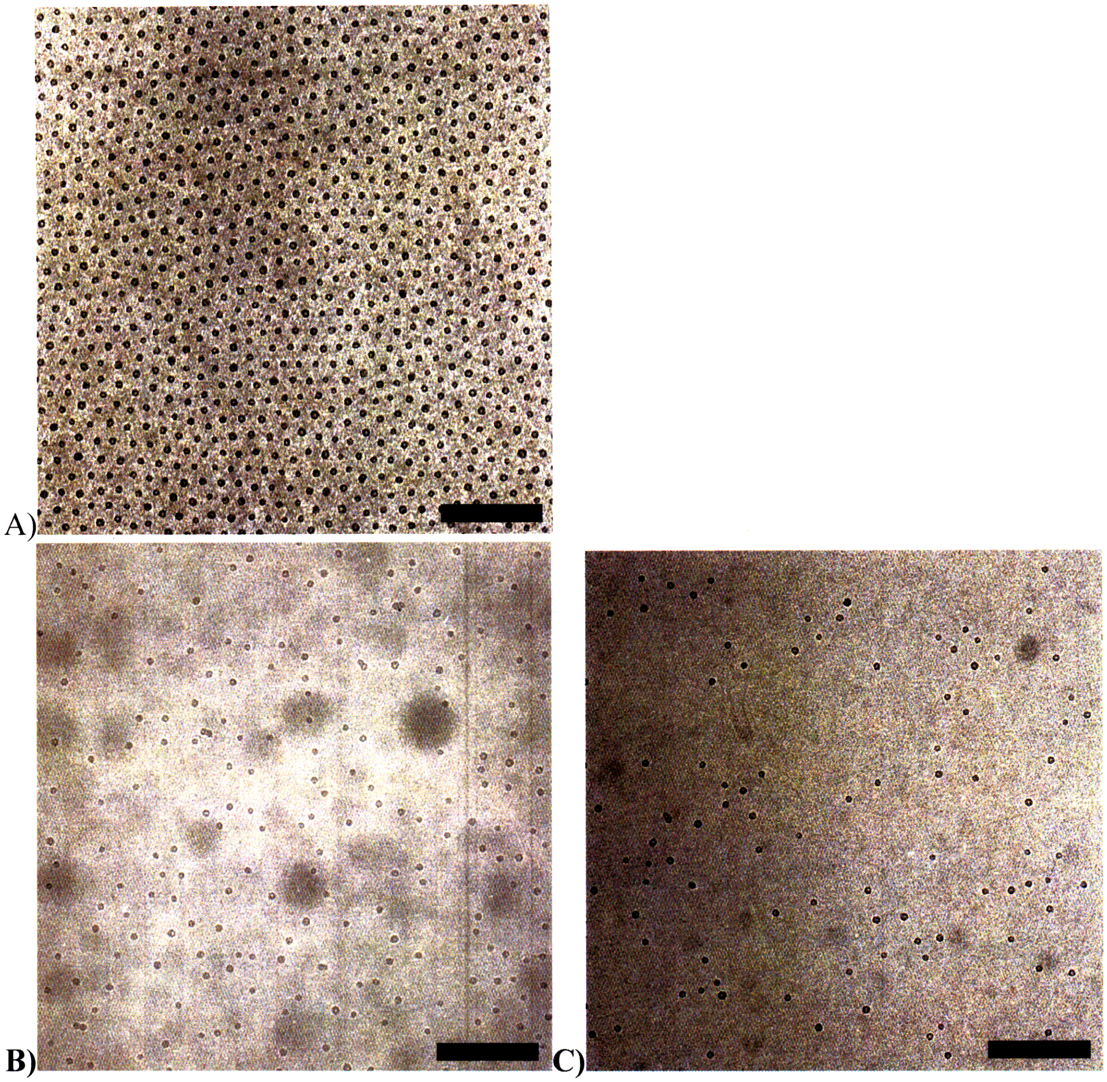

Figure 2-3: TEM images of iron oxide nanocluster arrays synthesized from micellar thin films using PS-b-PAA (M_n (PS) = 16 400 g/mol, M_n (PAA) = 4 500 g/mol) with a $FeCl_3$ loading ratio of 1.7 and a [PS : PS-b-PAA] equal to: (A) 0 (no PS homopolymer); (B) 4:1; (C) 10:1. Scale bar = 250 nm.

PS	PAA	Metal Loading Ratio	Ratio [PS : (PS-b-PAA)]	Spatial Density
(g/mol)	(g/mol)			(part/cm^2)
16 400	4 500	1.7	No PS homopolymer	6.0E+10
16 400	4 500	1.7	4 : 1	1.1E+10
16 400	4 500	1.7	10 : 1	6.5E+09

Table 2-2: Effects of varying the ratio of PS homopolymer molecules per PS-b-PAA molecule ([PS : PS-*b*-PAA]) on the spatial density of iron oxide nanocluster arrays.

As mentioned in the Experimental Section, the addition of PS homopolymer into the micellar solution increased the viscosity of the resulting solutions significantly, and toluene dilutions were employed to facilitate processing. As a control experiment to determine whether the dilution itself somehow affected the resulting micellar array spacing, a 5 mg PS-*b*-PAA / mL toluene solution without PS homopolymer was spin-cast onto a substrate to create a micellar thin film. The resulting TEM image (not shown) revealed metal nanocluster arrays that had diameters and center-to-center spacings which were identical to the metal nanocluster arrays created from micellar solutions with 13 mg PS-*b*-PAA / mL toluene and no PS homopolymer.

We have also performed AFM analysis of films with PS homopolymer in the absence of metal salts and using lower spin speeds. Using a spin speed of 1600 rpm (compared to 8000 rpm for films in Figure 2-3) thicker films would be expected, so a larger ratio of PS: PS-*b*-PAA would be need to achieve an equivalent decease in areal density. Figure 2-4 shows AFM images of films created with PS: PS-*b*-PAA ratios of 50:1 and 100:1 respectively. These films have areal densities similar to the films created with PS: PS-*b*-PAA ratios of 4:1 and 10:1 in Figure 2-3. There is also the possibility that micelles could be hidden beneath a film of PS homopolymer and thus not visible in AFM imaging. Spin casting conditions clearly could be used to vary the spacing of micellar films but we have not systematically investigated that here.

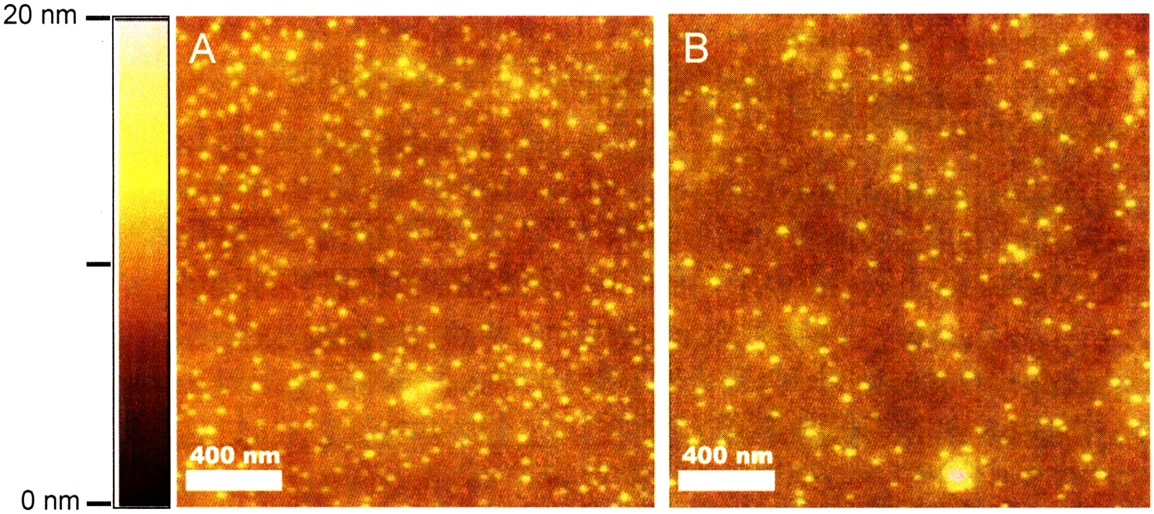

Figure 2-4: AFM height images of micellar thin films using PS-b-PAA (M_n (PS) = 16 400 g/mol, M_n (PAA) = 4 500 g/mol) and a [PS : PS-b-PAA] equal to (A) 50:1 and (B) 100:1.

2.1.3.3. Mixing of 'Empty' PS-*b*-PAA Micelles with Metal Loaded Micelles

Another useful strategy is to combine different micellar solutions, as shown in route iv from Figure 2-1. This novel procedure can allow for controlling the spatial density of loaded nanoreactors on the substrate or for the synthesis of multiple species metal nanocluster arrays.

Variations in the areal density of metal-loaded micelles on a substrate were achieved by combining a $PbAc_2$-loaded micelle solution (loading ratio ~5.4) with an unloaded micelle solution in a 1:1 volume ratio for 1 min and then spin-casting the solution onto a substrate. The resulting TEM image is shown in Figure 2-5. It is apparent from the TEM image that the spatial density of the metal nanoclusters has decreased due to an inclusion of empty PAA domains within the micellar thin film. By analyzing the image, we estimated the ratio of metal-loaded micelles to "empty" micelles in the thin film to be roughly 1:1 (67 PB-containing micelles and 73 'empty' micelles in

Figure 2-5B), which is equal to the ratio in our initial mixture. It is interesting to note that when the Pb-loaded micellar solution was mixed with the "empty" micellar solution for an even as little as 15 minutes, the thin films lacked "empty" micelles and contained only Pb-loaded micelles (images not shown). This demonstrates that there is a significant diffusion of metal species associated with the mixing of these solutions. We believe this route could be very useful in synthesizing arrays of cavitated nanoreactors with a controllable spatial density. A possible route would involve mixing a covalently crosslinked micellar solution (no cavitation possible) with an "empty" micelle solution, and then selectively cavitating the "empty" micelles after spin-casting the thin film. We have tried unsuccessfully to covalently cross-link micelles in Appendix A.

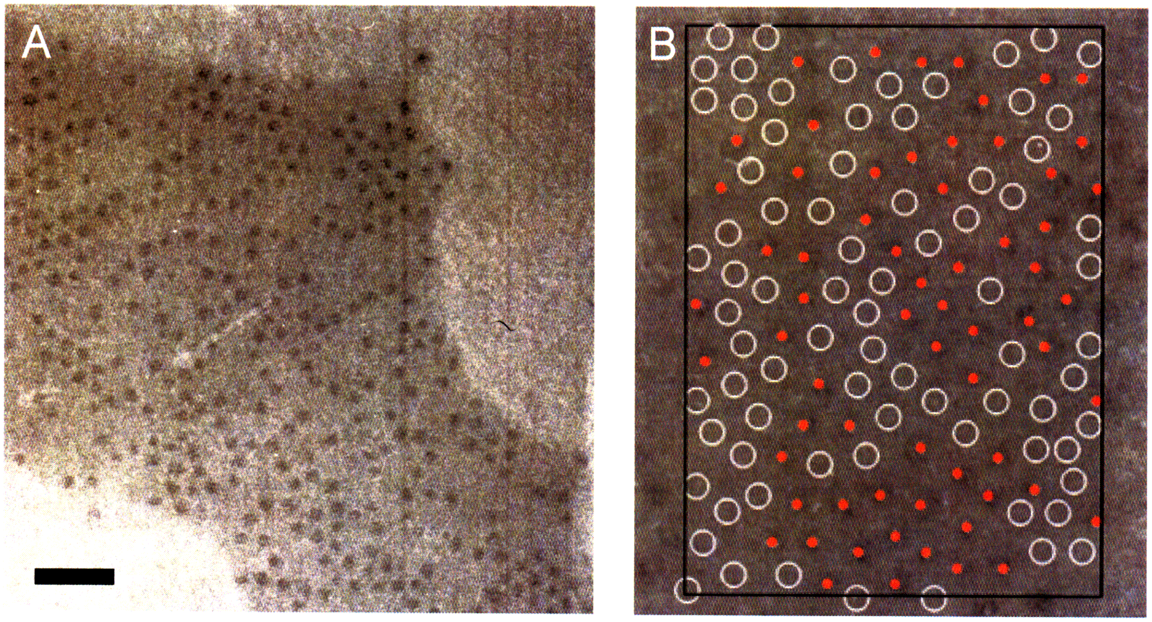

Figure 2-5: (A) TEM image of Pb-containing nanocluster array formed from a mixing a Pb-loaded micelle solution with an "empty" micelle solution in a 1:1 volume ratio for 1 min and then spin casting onto a substrate. Scale bar = 100 nm. (B) Zoom in of image A with red circles (67 total) applied to Pb-containing mcielles and open white circles (73 total) to 'empty' micelles.

2.1.3.4. Casting Micellar Thin Films from Dilute Solution

Yet another potential strategy to lower the areal density of micellar thin films is to cast films from dilute micelle solutions. We investigated this strategy by casting films of 'empty' PS-*b*-PAA 16.5-*b*-4.5 micelles at 1600 rpm on silicon using solution concentrations of 1, 0.1 and 0.01 mg/mL. For films cast from 1 mg/mL PS-*b*-PAA (Figure 2-6A) we observed areas that were continuous micellar films (spider web pattern) and areas that contain no micelles (circular area). The large object in the upper right of Figure 2-6A is a contaminant and should not be considered part of the micelle film. Figure 2-6B shows a film cast from 0.1 mg/mL PS-*b*-PAA, which has individual micelles spaced apart by significant distanced, but also a large group of continuous micelles and small groups of micelles. Individual micelles as well as groupings of two micelles are seen in films cast from 0.01 mg/mL PS-*b*-PAA. So we were able to increase the average micelle spacing, but were not able to achieve the individual micelles spaced apart as we did with the addition of PS homopolymer.

However, later results with two different polymer systems suggest that by increasing the spin rate and decreasing the ramp time would allow the creation of micelle films with individual micelle separate by large (compared to micelle size) spacings. In chapter 4 we discuss the block copolymer system, poly(ε-caprolactone)-*block*-poly(2-vinyl pyridine) (PCL-*b*-P2VP) which forms inverse micelles in toluene in detail. By reducing the solution concentration to 0.01 mg/mL and casting film at 2500 rpm with a 1 second ramp time micelle films with greatly increased spacing were observed without aggregates of multiple micelles as for PS-*b*-PAA (Figure 2-6D). There is significant polydispersity in the micelle size for PCL-*b*-P2VP compared to PS-*b*-PAA because of the polydisperisty of the copolymer (PDI = 1.8 for PCL-*b*-P2VP vs. PDI = 1.05 for PS-*b*-PAA). This result could be because of increased spin speed and decreased ramp time or because of some difference in the interaction of the micelle upon solvent evaporation. However, it seems more likely that these more aggressive spin-casting conditions lead to an increase in the toluene evaporation rate, which limits micelle aggregation. It is possible that using these spin-casting conditions would allow the creation of increased micelle spacing without aggregation occurring for PS-*b*-PAA.

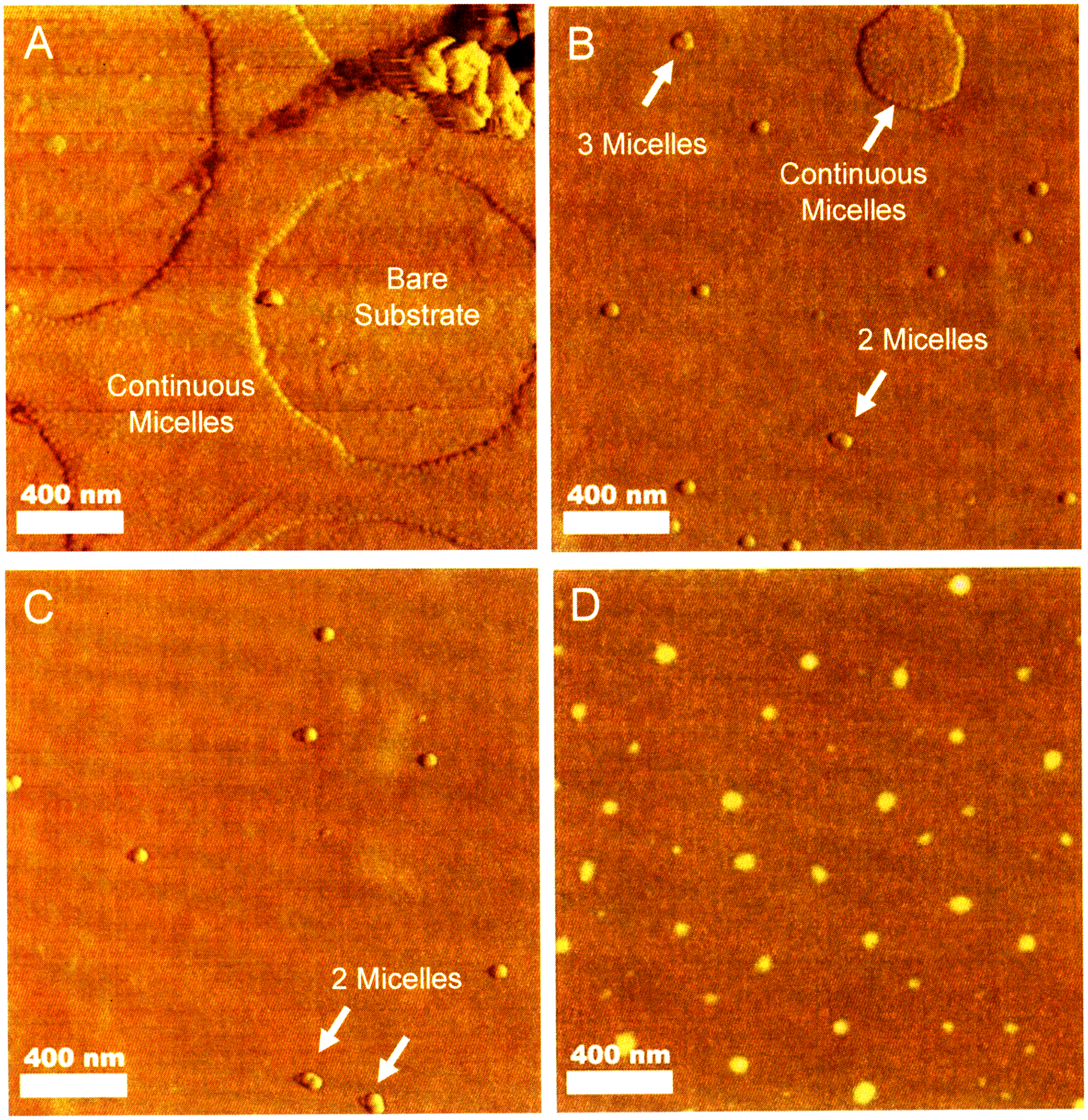

Figure 2-6: (A-C) AFM phase images of PS-*b*-PAA inverse micelles cast on silicon substrates from toluene at solutions concentrations of (A) 1 mg/mL, (B) 0.1 mg/mL, and (C) 0.01 mg/mL. Spin-casting conditions were 1600 rpm with a 5 second ramp for all samples. Z scale = 50°. (D) AFM height image of PCL-*b*-P2VP cast on silicon from 0.01 mg/mL solution in toluene. Spin-casting conditions were 2500 rpm with a 1 second ramp time. Z scale = 20 nm.

We also briefly studied the effect of decreasing the concentration and ramp time while increasing the spin rate for PS-*b*-P2VP 55-*b*-50 micelles in toluene. Close-packed micelle films are created by casting 10 mg/mL solutions in toluene and 1600 rpm with a 5 second ramp time (Figure 2-7A). However, when casting from 1 mg/mL solution with a ramp time of 1 second and a ramp speed of 8000 rpm films with individual micelles spaced from their nearest neighbor are created (Figure 2-7B). The micelle spacing is further increased by decreasing the solution concentration to 0.19 mg/mL (Figure 2-7C). Lower solutions concentration were not tested, but it is possible that micelle films with much larger spacing could be created without observing patches of continuous micelle film similar to what was observed for PCL-*b*-P2VP.

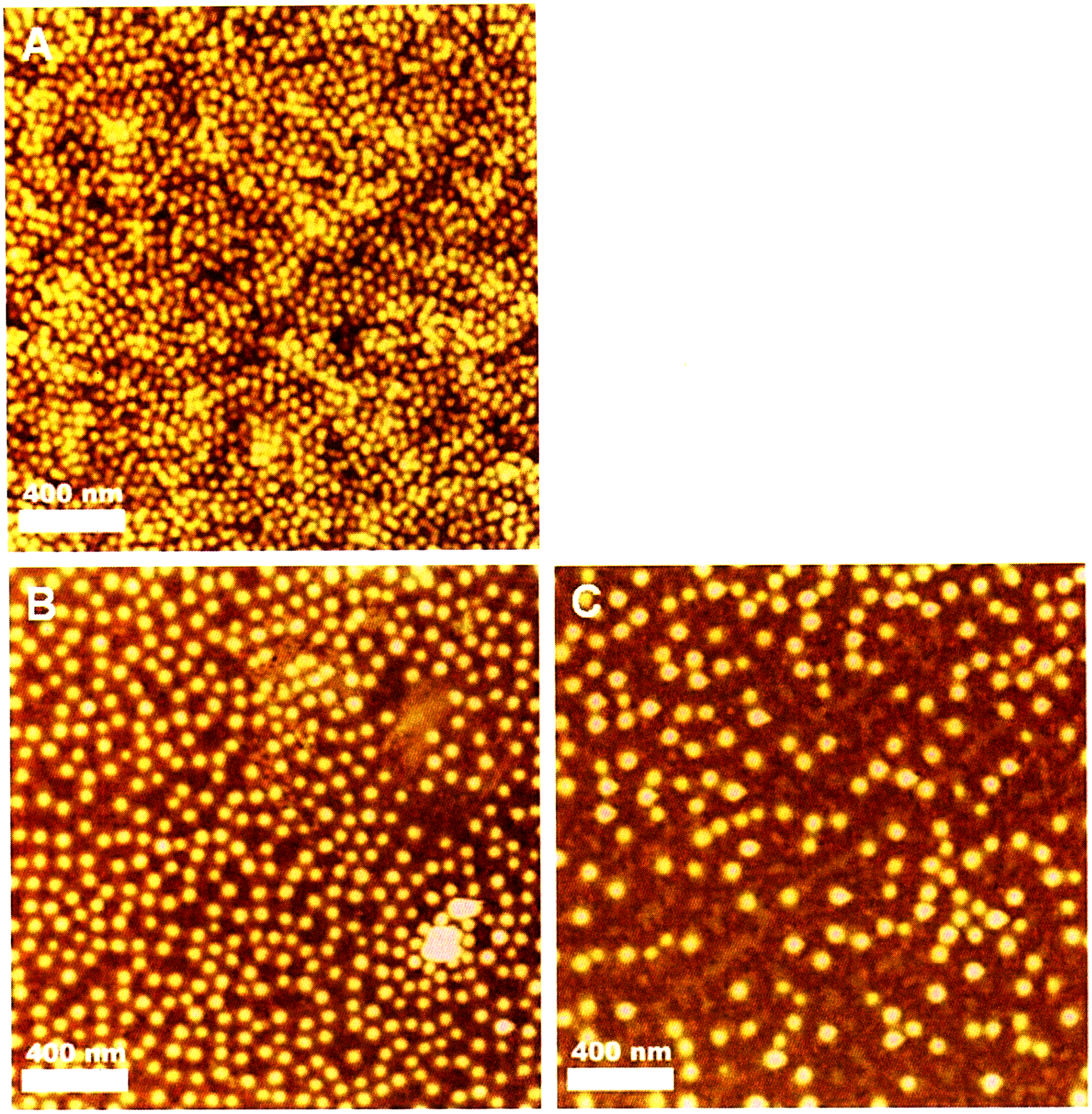

Figure 2-7: AFM height images of PS-*b*-P2VP 55-b-50 micelles on silicon substrates cast from toluene. (A) Film cast from 10 mg/mL solution in toluene at 1600 rpm with a 1 second ramp. Films cast at 8000 rpm with 1 second ramps from (B) 0.75 mg/mL and (C) 0.19 mg/mL solution in toluene.

2.1.4. Conclusions

We have demonstrated the ability to vary the size, center-to-center spacing, and density of spin-cast 2-D arrays of spherical PS/PAA micelles and the subsequent inorganic nanoclusters synthesized therein. The strategies used to vary the arrays include alteration of the block copolymer molecular weight, addition of PS homopolymer, combination of different micellar solutions, and by spin-casting from dilute solution. The strategies discussed in this work could have useful applications in the synthesis of carbon nanotube catalysts and in the construction of nanopatterned substrates for the investigation of cell attachment and function.

2.2. Patterning of Inverse Micellar Thin Films on the Micron Length Scale using Soft Lithographic Techniques

2.2.1. Introduction

Reliable and facile patterning of substrates on the micron length scale is an important technological challenge. Patterning using soft lithography,[22-25] which relies on using an elastomeric polymer to replicate a hard master, has emerged successfully as a fast, inexpensive, and straightforward route for patterning substrates.[26]

Microcontact printing (μCP) is a powerful soft lithographic patterning technique that has received much attention since its development roughly a decade ago.[56-58] While μCP was originally utilized to pattern self-assembled monolayers of alkane thiols on gold,[57] this technique has also been shown to be effective in patterning polymeric thin films.[26, 59-61] In general, this approach consists of wetting or "inking" a poly(dimethylsiloxane) (PDMS) stamp with a polymer solution, followed by transferring the polymeric thin film to the substrate. As expected, the competitive interplay of surface energies and wetting behavior of the components is central to successful printing using this technique.

Convective self-assembly using microfluidic channels[62] is another PDMS stamp-based technique that can be used to pattern polymer films. In this approach the PDMS stamp is placed in contact with the substrate and then a polymer solution is taken up into the features of the stamp via capillary action. The size and arrangement of features that can be made using this method is therefore limited by the need for a capillary force to drive convection of the polymer solution into the PDMS stamp.

As described in the previous section, amphiphilic block copolymer micelles in organic solvents represent a novel type of polymer solution from which micelles are capable of self-assembling into nanoscale ordered structures when deposited onto a surface.[21, 53, 55] For many of the applications of these systems, it would be very useful to pattern these block copolymer micellar thin films on a micron length scale or smaller to complement the inherent nanostructure of the thin films. In previous work, block copolymer micellar thin films have been patterned using both e-beam and photo lithography.[63-65] While these routes have been shown to be effective in patterning on length scales as small as 100 nm, these routes are time consuming, expensive, and equipment intensive. Recently Yun *et al.*[65] developed a soft lithographical method for patterning polystyrene-*block*-poly(4-vinylpyridine) (PS-*b*-P4VP) micelles onto a substrate utilizing μCP. In this approach, a toluene-based solution of PS-*b*-PVP micelles loaded with $FeCl_3$ is spin coated onto a PDMS stamp and then transferred to a silicon (Si) substrate through μCP. This route achieved micron-scale patterning of PS-*b*-PVP micellar thin films, which were subsequently oxygen plasma etched to create a monolayer of iron oxide nanoclusters.

We present two soft lithographical routes for fabricating patterned block copolymer micellar thin films. The first utilizes dip-coating to ink the PDMS stamp prior to μCP. In our approach we utilize the amphiphilic block copolymer, poly(styrene-*block*-acrylic acid) (PS-*b*-PAA), which forms spherical micelles when added to a toluene solution and heated.[21, 53, 55] After inking a PDMS stamp with this micellar solution using dip coating, we allow the toluene to evaporate before transferring the patterned block copolymer thin films onto a substrate through μCP. We demonstrate the ability to control the size, periodicity, and characteristic shape of the patterned areas through variation of the PDMS stamps. While confirming the results of Yun *et al*[65] by demonstrating the ability to transfer PS-based block copolymer micellar thin films from a PDMS stamp to a Si substrate, we also identify interesting wetting behavior that we believe is due to the inhomogeneous swelling of the PDMS stamp in toluene during dip-coating. This swelling leads to patterned micellar thin films with feature dimensions that are smaller than the corresponding PDMS stamp dimensions, while the periodicity of the patterned micellar thin films corresponds to the PDMS stamp periodicity. This interesting wetting behavior that causes smaller feature dimensions allows us to pattern stripes and circles of micellar thin films on the nanometer length scale. We also present results demonstrating the effect of varying the removal velocity of the PDMS stamp from the micellar solution, which alters the deposition of the micellar thin film onto the PDMS stamp. By varying the removal velocity we are able to create both positive and negative replications of the PDMS stamp with micellar thin films. Convective self-assembly using microfluidic channels is also used to create lined patterns of block copolymer micelles. We characterize these patterned substrates using optical microscopy as well as atomic force microscopy (AFM). Using the latter technique we also confirm that the PS-*b*-PAA thin films maintain their micellar nanostructure upon printing.

2.2.2. Experimental Section

2.2.2.1. Materials

Poly(styrene-*block*-acrylic acid) (PS-*b*-PAA) [M_n (PS) = 16 400 g/mol, M_n (PAA) = 4 500 g/mol, PDI = 1.05] was used as received from Polymer Source, Inc. PDMS stamps were synthesized by pouring a two-component curable siloxane (Sylgard 184, Dow Corning) over a silicon master with the desired pattern. Toluene (HPLC grade, 99.8%) was obtained from Sigma-Aldrich Co. and used as received. Polished, single crystal silicon (Si) wafers (p-type) were used as received from WaferNet, Inc.

2.2.2.2. Sample Preparation

PS-*b*-PAA was mixed with toluene at a concentration of 5.5 mg/mL and heated to 145 °C for 20 min in a sealed vial to create a spherical block copolymer micellar solution. Details about the formation of spherical block copolymer micelles in solution have been presented in section 2.1 above and published previously.[21, 53, 55] The untreated PDMS stamps were inked by dipping the stamps into the micellar solution with the normal to the patterned surface oriented horizontally. The PDMS stamps were submerged in the solution for 3 s, and then removed at a rate of 0.5 – 2 mm s^{-1}. The PDMS stamps were then allowed to dry for 4 min with the normal to the patterned surface oriented horizontally, and then rotated to dry 1 min with the normal to the patterned surface oriented vertically. The PDMS stamps were then placed in contact with an untreated Si substrate for 3-5 min with an applied pressure that varied depending on the dimensions of the PDMS stamp. For the channeled PDMS stamps, the applied pressure for the 8 μm diameter stamp was approximately 40 MPa, while the applied pressure for the stamp with 1 um diameter posts was approximately 180 MPa. An excessive level of applied stamping pressure causes the entire stamp to contact the substrate (easily observed visually during stamping), in which case the applied pressure needs to be reduced for proper stamping. The channeled PDMS stamps had a constant feature height of 400 nm (variable aspect ratio from 2.5 to 20), while the cylindrical post PDMS stamps had a constant aspect ratio of 1. The μCP procedure is illustrated schematically in Figure 2-8.

The stamps were slowly peeled from the substrate to leave a patterned block copolymer micellar film on the substrate.

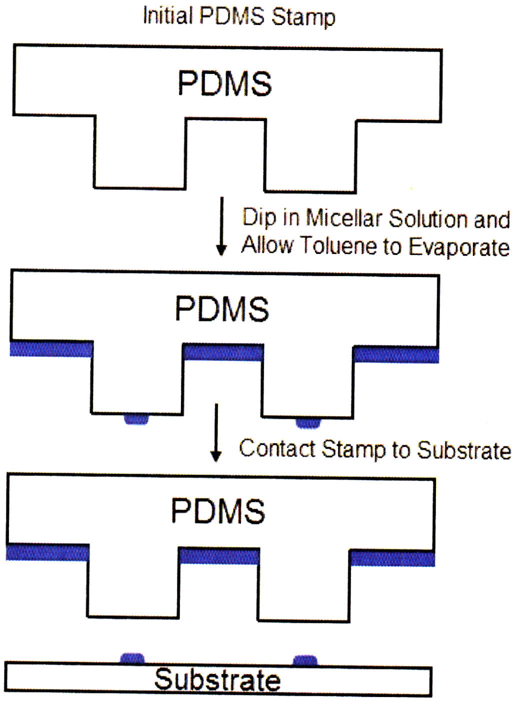

Figure 2-8: Schematic illustration of the μCP of block copolymer micellar thin films using a PDMS stamp. The dimensions of the inked regions on the stamps are shown to be smaller than the characteristic size of the stamp feature dimensions, consistent with microscopic observations presented below. Unless excessive stamping pressure is used, only the micellar regions from the raised features are transferred to the substrate, as shown here.

For convective self-assembly using microfluidic channels, a PDMS stamp with a 400 nm feature height, 10 μm lines and 20 μm periodicity was placed in contact with either a glass microscope slide or silicon wafer. 10 μL of 5.5 mg/mL PS-*b*-PAA solution in toluene was then pipped onto the substrate at one end of the PDMS stamp. The solution then wicked up into the PDMS stamp. The solution was allowed to dry by evaporation for 1 hour before the PDMS stamp was slowly removed from the substrate leaving behind the patterned micelle thin film.

2.2.2.3. Characterization

The patterned films were examined using a Leica optical microscope equipped with a Nikon digital camera (DXM 1200F) using Nikon imaging software. Images were obtained in reflectance mode. Atomic force microscopy (AFM) images were obtained using a Digital Instruments Dimension 3000 Nanoscope IIIA scanning probe microscope operating in tapping mode using a silicon cantilever. Contact angle measurements were performed on an Advanced Surface Technology video contact angle measuring device using the standard sessile drop technique.

2.2.3. Results and Discussion

2.2.3.1. Microcontact Printing Lined Patterns of Micellar Thin Films

The optical microscope images in Figure 2-9 demonstrate the effectiveness of using μCP to pattern PS-*b*-PAA micellar thin films. The results observed in Figure 2-9 are quantified in Table 2-3, which shows that by varying the width of the raised PDMS features from 1 um to 8 um, we are able to vary the width of the PS-*b*-PAA patterns from 0.5 to 1.5 um. The data in Table 2-3 also indicate that the patterned PS-*b*-PAA stripes have a width that is considerably smaller than the original width of the PDMS stamp. We believe that this effect is caused by the inhomogeneous swelling of the PDMS stamp. Because the edges of the PDMS channel have more surface area exposed to toluene, the edges will achieve a higher degree of swelling than the inner region. This inhomogeneous swelling of the PDMS in toluene causes the micelle solution to collect towards the center line of the PDMS features (See Figure 2-9). This effect has been documented previously in μCP patterning of the poly(styrene-*alt*-maleic anhydride)/tetrohydrofuran system.[59] In the present case, once the toluene evaporates, the PS-*b*-PAA micellar thin film is kinetically trapped on the surfaces of the stamp features because the continuous PS matrix has a glass transition temperature that is well above room temperature.

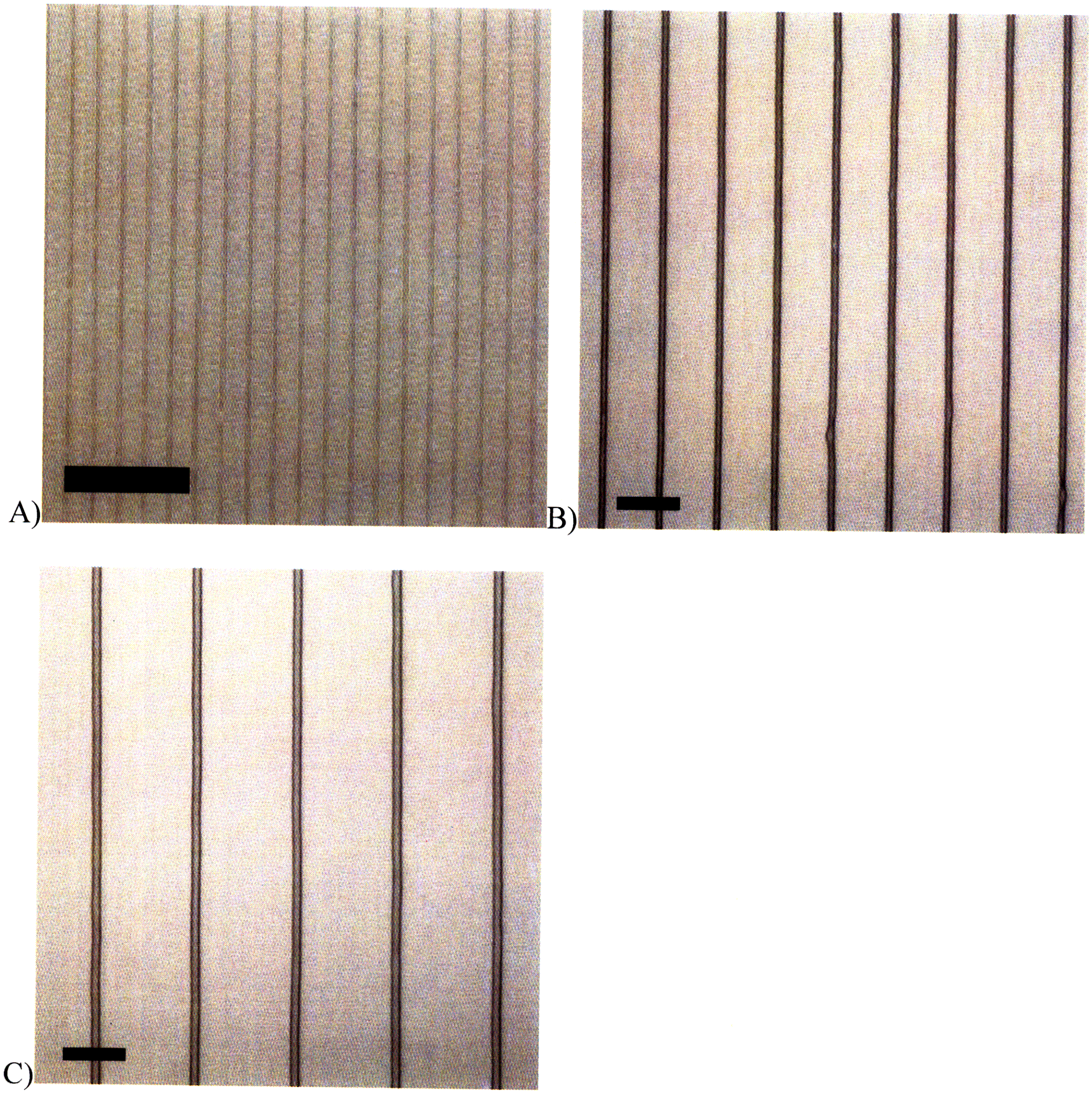

Figure 2-9: Optical microscope images of PS-*b*-PAA micellar thin films patterned using μCP with a PDMS stamp with a feature width and periodicity of: (A) 1 um and 2 um, (B) 4.5 um and 9 um, and (C) 8 um and 16 um. Scale bar = 10 um.

Feature width of PDMS stamp (um)	Periodicity of PDMS stamp (um)	Width of patterned PS-*b*-PAA thin film (um)	Periodicity of patterned PS-*b*-PAA thin film (um)
1.0	2.0	0.5	2.0
4.5	9.0	0.9	8.9
8.0	16.0	1.5	15.8

Table 2-3: Effects of varying the feature width and periodicity of the PDMS stamp on the width and periodicity of the resulting PS-*b*-PAA micellar thin film features.

The optical microscope image in Figure 2-10 demonstrates the effect of using excessive stamping pressure. The patterns in this image were created using a PDMS stamp with 5 um wide features and a periodicity of 10 um using an applied pressure of 600 MPa. The regions of the patterned micellar thin films labeled “A” in Figure 2-10 correspond to material that was located on the top of the PDMS features prior to contacting the substrate, and these are the areas that transfer to the substrate with moderate applied pressures, as shown in Figure 2-9. The patterned areas labeled “B” in Figure 2-10 represent the micellar material that resided in the troughs between the raised features on the PDMS stamp. The white regions correspond to bare substrate. With lower applied pressures the troughs did not make contact with the substrate and were not printed, as demonstrated in Figure 2-9. When excessive pressure is applied, the micellar thin films located in the troughs contacted the surface and were transferred to the substrate. The inset in Figure 2-10 shows the region of the substrate that was patterned by the end of the raised features of the PDMS stamp. This image shows that the regions labeled “B” in Figure 2-10 continuously connect with the polymer thin film regions patterned where the raised features have ended, confirming that the regions labeled “B” were transferred from the troughs of the PDMS stamp. The width of the films labeled “B” in Figure 2-10 correspond exactly to the width of the troughs of the PDMS stamp, giving more evidence for the proposed mechanism. The regions labeled "A" were transferred from the raised features of the PDMS stamps, and these patterned areas end where the raised features of the PDMS stamp end. The inset in Figure 2-10 also corroborates the inhomogeneous swelling mechanism by showing that the patterned thin films from the top of the raised features do not extend to the end of the PDMS raised features, due to the higher swelling at the end of the raised features. The regions labeled "B" in Figure 2-10 exhibit a distinct three-fold structure along their edges; we are unsure of the mechanism for its formation.

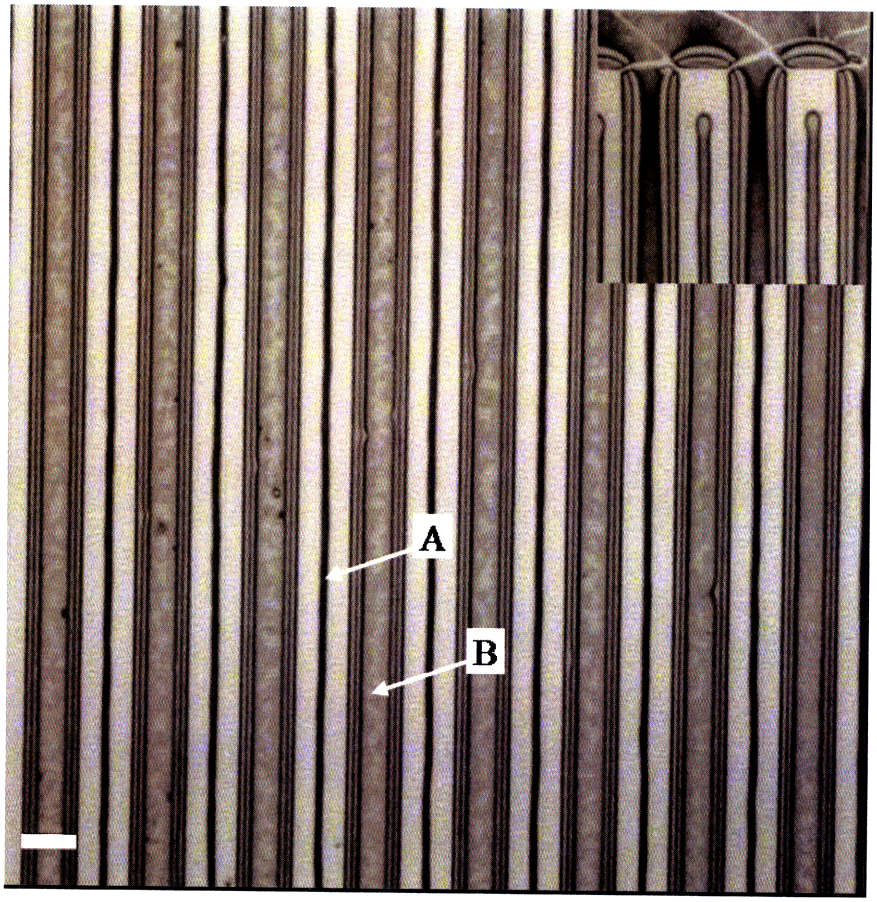

Figure 2-10: Optical microscope images of PS-*b*-PAA micellar thin films patterned using μCP with an applied pressure of 600 MPa and a PDMS stamp with a channel width of 5 um and a periodicity of 10 um. The narrow patterned films labeled "A" in the image correspond to the micellar thin films that originally were located on the top of the raised PDMS features prior to stamping. The regions labeled "B" in the image correspond to micellar thin films that were originally located in the troughs of the PDMS prior to

stamping. The inset shows the patterned substrate at the edge of the PDMS stamp. Scale bar = 5 um.

Figure 2-11 shows the AFM characterization of the PS-*b*-PAA micellar thin films patterned by using a PDMS stamp with a channel width of 7 um and a periodicity of 14 um and an applied pressure of 40 MPa. Figure 2-11A shows an AFM height image of the substrate after stamping. The thickness of the patterned micellar thin films is demonstrated in Figure 2-11B, which shows an individual scan line between the two triangles shown in Figure 2-11A. This shows that the patterned stripes are approximately 100 nm thick and are uniform in shape. To confirm that the micellar substructure persisted in the patterned areas, we examined the areas indicated by the white squares in Figure 2-11A at higher resolution. Figure 2-11C shows the AFM phase image of the patterned micellar thin film that is located in the square labeled "c)" in Figure 2-11A. The observed structure is identical to previous AFM images of micellar thin films[21, 53] of this same block copolymer, and verifies the nanoscale sub-structure of the patterned thin films. Figure 2-11D shows the AFM phase image of the area indicated by the square labeled "d)" in Figure 2-11A and corresponds to the smooth structure of the bare Si substrate. From these AFM results we are able to conclude that our μCP procedure enables the creation of substrates with well-defined patterns of PS-*b*-PAA micellar thin films. The thickness of the patterned stripes suggests there are 4 - 5 layers of micelles, as compared to the micellar monolayers that could be created using a spin casting approach. The cracks observed in Figure 2-11A are believed to arise from stresses that are imparted to the glassy polymer thin films during handling of the PDMS stamp during the stamping procedure. We have found that these cracks can be minimized by delicately handling the PDMS stamps during the stamping procedure.

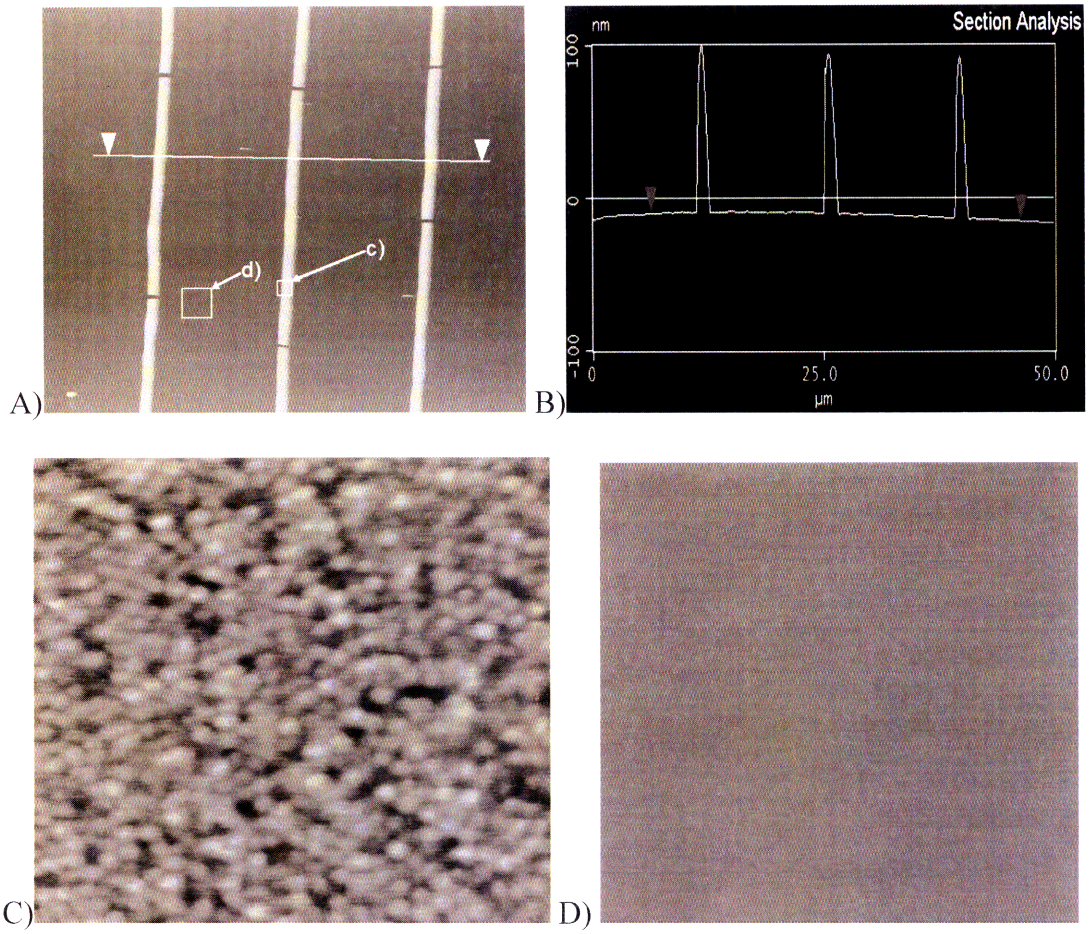

Figure 2-11: AFM characterization of a PS-*b*-PAA patterned micellar thin film using a PDMS stamp with a channel width of 7 um and a periodicity of 14 um. (A) AFM height image (50 um by 50 um scan) showing a patterned PS-*b*-PAA micellar thin film on a Si substrate; (B) Plot of individual scan line along the line connecting the two white triangles in (A); (C) AFM phase image (0.6 um by 0.6 um scan, 50° scale) from the square denoted "c)"; (D) AFM phase image (2.5 um by 2.5 um scan, 50° scale) from the square area denoted "d)".

2.2.3.2. Microcontact Printing for Circular Patterned Films

The optical microscope images in Figure 2-12 demonstrate the capability of using this μCP procedure to pattern PS-*b*-PAA micellar thin films in other geometries. The micellar thin films observed in Figure 2-12 were obtained using a PDMS stamp with cylindrical post features and a removal velocity of the stamp from the toluene solution of 1 mm s^{-1}. The results are quantified in Table 2-1. Figure 2-12A - C demonstrate the ability to vary the periodicity of the resulting PS-*b*-PAA micellar thin film patterns from 6.1 um to 17.5 um. In these images the diameters of the patterned micellar areas varied between 0.5 um and 0.6 um, which is much smaller than the diameter of the cylindrical posts on the PDMS stamp and similar to the result that was observed for the PDMS stamp with linear features (see Figure 2-9 and Table 2-3).

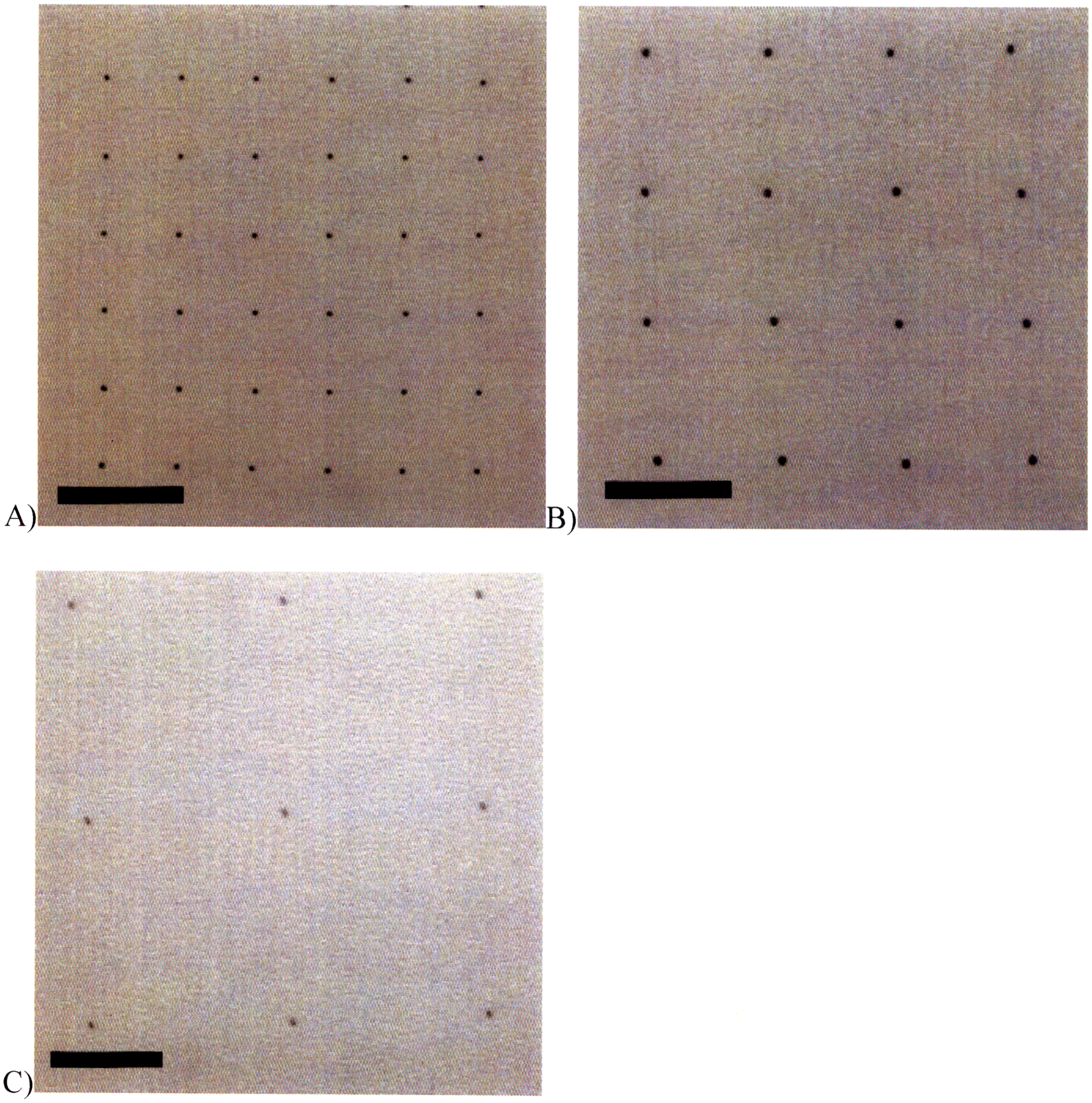

Figure 2-12: Optical microscope images of PS-*b*-PAA micellar thin films patterned using μCP with a PDMS stamp of cylindrical posts with a removal velocity of 1 mm s^{-1} and with a diameter and periodicity of: (A) 4 um and 6 um, (B) 4 um and 10 um, and (C) 3 um and 18 um. Scale bar = 10 um.

Diameter of posts on PDMS stamp (um)	Periodicity of posts on PDMS stamp (um)	Diameter of patterned PS-*b*-PAA thin film (um)	Periodicity of patterned PS-*b*-PAA thin film (um)
4.0	6.0	0.6	6.1
4.0	10.0	0.6	9.6
3.0	18.0	0.5	17.5

Table 2-4: Effects of varying the diameter and periodicity of cylindrical posts on a PDMS stamp on the diameter and periodicity of the resulting patterned PS-*b*-PAA micellar thin film.

Although the μCP of stripes of micellar thin films was relatively insensitive to the removal velocity of the PDMS stamp from the inking solution, the μCP using PDMS stamps with circular posts was quite sensitive to the PDMS stamp removal velocity. For the results in Figure 2-12, a removal velocity of 1 mm s^{-1} caused micellar thin films to deposit onto the tops of the cylindrical posts and subsequently transfer to the Si substrate. When the removal velocity of the PDMS stamp with cylindrical posts was lowered to 0.2 mm s^{-1}, the micellar thin film didn't deposit onto the top of the circular posts, as demonstrated in Figure 2-13A. Figure 2-13A shows an optical microscope image of a PS-*b*-PAA micellar thin film patterned using μCP with an applied pressure of 600 MPa using a PDMS stamp of cylindrical posts with diameters of 4 um and a periodicity of 8 um. Because of the large applied pressure, inked material from both the top of the raised features and the troughs should transfer from the PDMS stamp to the substrate. In this image, however, the well-defined circles correspond to bare substrate indicating that the cylindrical posts did not have micellar thin film deposited on their top surface due to the slower removal velocity. In Figure 2-13B, an optical microscope image shows a PS-*b*-PAA micellar thin film patterned using an applied pressure of 600 MPa using a PDMS stamp of cylindrical posts with a diameter of 4 um and a periodicity of 10 um and a removal velocity of 1 mm s^{-1}. In this image the PS-*b*-PAA micellar thin film did ink the tops of the cylindrical posts, and was subsequently transferred to the substrate along with the micellar thin film from the trough. Thus varying the removal velocity of the PDMS stamp from the micellar solution and the applied pressure, we are able to create positive, negative, and mixed representations of the PDMS stamp using a PS-*b*-PAA micellar thin film.

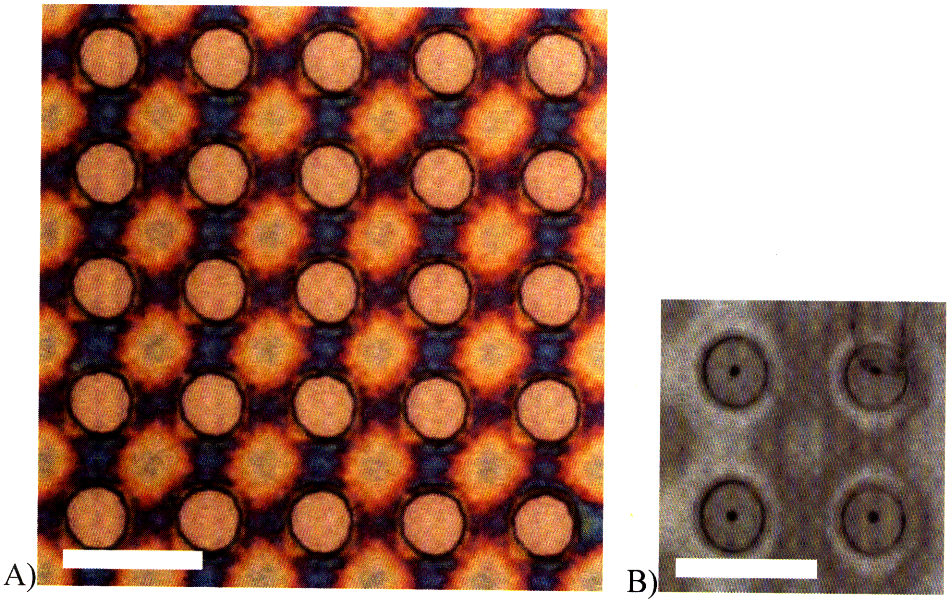

Figure 2-13: (A) Optical microscope image of a PS-*b*-PAA micellar thin film patterned using μCP with an applied pressure of 600 MPa using a PDMS stamp of cylindrical posts with diameters of 4 um and a periodicity of 8 um and a removal velocity of 0.2 mm s^{-1}. The lighter areas correspond to bare substrate, while the darker areas correspond to PS-*b*-PAA micellar thin film. (B) Optical microscope image of a PS-*b*-PAA micellar thin film patterned using μCP with an applied pressure of 600 MPa using a PDMS stamp of cylindrical posts with diameters of 4 um and a periodicity of 10 um and a removal velocity of 1 mm s^{-1}. Scale bars = 10 um.

2.2.3.3. Convective Self-Assembly using Microfluidic Channels

We have also successfully created lined patterns of PS-*b*-PAA micelle thin films using convective self assembly using microfluidic channels. Figure 2-14A shows an optical microscope image of a patterned micelle film created with a PDMS stamp that had a pattern of 10 μm lines with 20 μm periodicity. The dark areas correspond to micelle films while the white areas correspond to bare substrate. Similar to μCP printing we observed some effect from the swelling of PDMS with toluene. Here the PDMS lined pattern swells, simultaneously increasing the PDMS line width and decreasing the line width of bare substrate available for deposition of micelles. So we observed micelle patterns with a periodicity that matches the original PDMS stamp, but with reduced feature sizes. However, there appear to only be a 10-20% reduction in feature size compared to the much larger changes seen in μCP. We were able to observe the patterned film edge in AFM showing the continuous micelle film and adjacent bare silicon substrate (Figure 2-14B). The step height between the bare substrate and the micelle film is about 20 nm, which corresponds to the thickness of a PS-*b*-PAA 16.5-*b*-4.5 monolayer micelle film. It should be noted that it is difficult to obtain bare substrate between the PDMS features. Frequently, continuous micelle films were deposited. These films completely covered the substrate and had a step change in the film thickness corresponding to the PDMS feature width and periodicity. Presumably the toluene was able to swell the PDMS and penetrate between the PDMS and silicon substrate leading to film deposition where the PDMS features originally were in contact with the substrate. Adhesion between the PDMS stamp and substrate is an inherent difficulty in convective self-assembly.

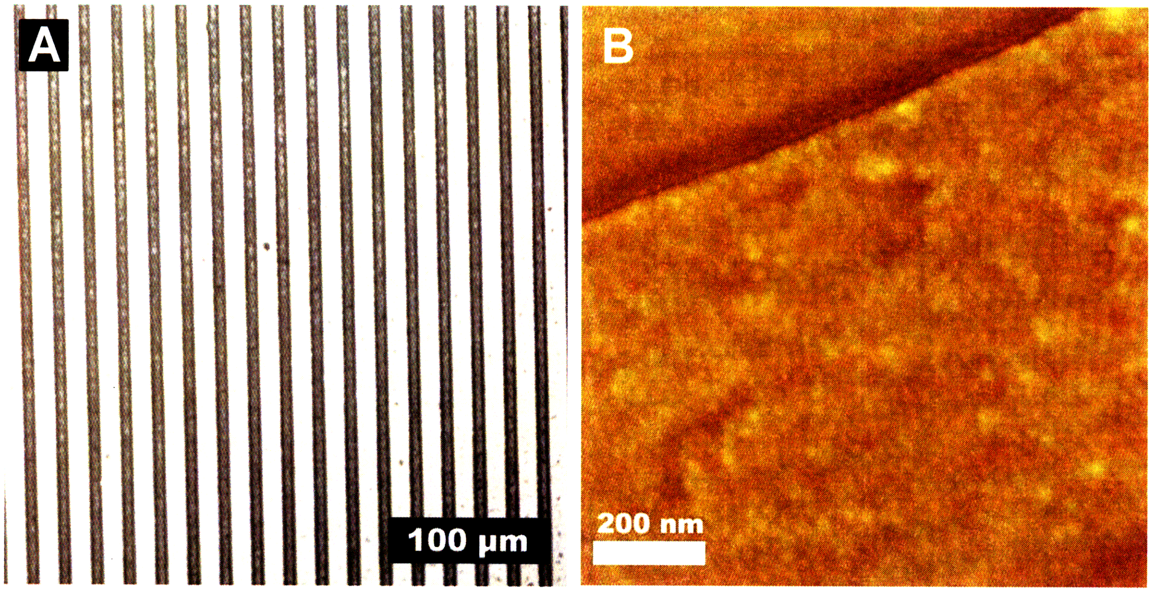

Figure 2-14: (A) Optical microscope image of patterned PS-*b*-PAA micelle film create using convective self-assembly with a PDMS stamp with 10 µm lines with 20 µm periodicity. (B) AFM phase image of an edge of the patterned micelle films showing bare substrate in the upper left of the image and continuous micelle film in the lower right. The step height change between the bare substrate and micelle film is around 25 nm, corresponding to the thickness of a monolayer of PS-*b*-PAA 16.5-*b*-4.5 micelle film.

2.2.4. Conclusions

In this work we have demonstrated a simple, effective, and easily accessible route for patterning PS-*b*-PAA micellar thin films using a µCP approach. We demonstrate the ability to create patterned features, while varying their characteristic length, periodicity, and characteristic shape. We also use AFM to characterize the structure of our patterned substrates as well as to verify that the patterned thin films maintain their micellar structure. Because these micellar thin films are capable of acting as both open arrays of carboxylic acid nanoreactors and as templates to create inorganic nanoclusters, we believe that the ability to pattern these block copolymer micellar thin films will have many useful applications. One of these applications, creating patterned iron oxide nanocluster arrays for carbon nanotube synthesis selectively on the patterned regions of the substrate, has been demonstrated by Bennett et al.[54]

Chapter 3 CAVITATION AND THE CREATION OF FUNCTIONAL NANOCAVITIES

3.1. Introduction

Block copolymers have been the subject of significant recent research due to their ability to self-assemble on the nanometer length scale into a variety of morphologies. Often, block copolymer films are solvent cast and annealed to form highly ordered equilibrium morphologies. A different approach can be utilized for block copolymers in selective solvents, which facilitate the formation of stable ordered structures in solution. The exchange of block copolymer molecules between micelles and solution is very slow compared to the exchange kinetics observed for low molecular weight surfactant micelles.[2] A favorable result of these slow exchange kinetics is the ability to retain a micellar morphology during casting from selective solvents onto solid substrates; this morphology becomes kinetically trapped in the final thin film upon solvent evaporation, even in cases for which the copolymer composition would suggest a transition to a different equilibrium heterogeneous phase. One of the most extensively studied polymer systems for formation of such micellar thin films is poly(styrene-*block*-X-vinylpyridine) (PS-*b*-PXVP) (X = 2 or 4). These films have been studied for their potential use in a variety of applications including data storage,[3] nanolithography,[4-12] and deposition of metal nanoparticle arrays such as gold catalyst particle arrays for zinc oxide nanowire synthesis,[13] iron oxide nanoparticles for carbon nanotube synthesis[14] and magnetic applications,[15] zinc oxide nanoparticles for optical devices[16] and nickel[17] or gold[18-20] arrays for protein binding.

There has also been recent interest in the swelling and rearrangement of amphiphilic block copolymers for the creation of nanostructured films that contain nanopores and nanocavities. Previous work in our lab demonstrated the creation of 2-D arrays of nanocavities in polystyrene-*block*-poly(acrylic acid) (PS-*b*-PAA) thin films.[21] A PS-*b*-PAA polymer with PS and PAA block molecular weights of M_n = 16 400 g/mol and M_n = 4 500 g/mol respectively formed kinetically trapped spherical inverse micelles in toluene after a suitable heating and cooling cycle described earlier,[21] which were then spin-cast onto a planar substrate to create a quasi-hexagonal array of PS-*b*-PAA micelles. When films of PS-*b*-PAA were exposed to highly alkaline aqueous solutions with monovalent cations, the PAA domains swelled and ruptured the glassy PS corona, a process we termed cavitation (Figure 3-1). In the previous chapter, we have shown control over the size and spacing of the spherical PAA domains of these micellar films by varying the molecular weight of the block copolymer, adding PS homopolymer to the block copolymer micellar solutions before casting films, and casting from dilution solutions.[55] The ability to pattern these nanostructured films using soft lithographic techniques was also demonstrated.[54] A variety of multivalent metal ions have been loaded into these micelles pre- and post-cavitation. If the polymer is subsequently plasma-etched or pyrolized, a 2-D array of inorganic nanoparticles is produced on the supporting substrate, which, for the particular case of iron oxide, we have used successfully as a structured catalyst for carbon nanotube synthesis.[53, 54, 66]

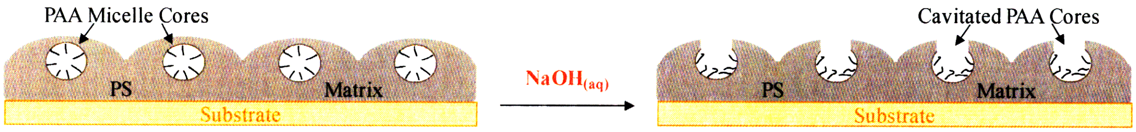

Figure 3-1: Schematic of cavitation of PS-*b*-PAA micelles demonstrated previously by Boontongkong and Cohen.[21]

A number of studies have characterized the formation of nanocavities in related polymer systems. Cong et al.[67] and Li et al.[68] have observed similar cavitation behavior for films of PS-*b*-P2VP micelles when these films were exposed to high relative humidity or acetic acid, respectively. Semifluorinated alkanes can form arrays of nanocavities,[69] but the surfaces of such films consist of only a single functionality, unlike some of the block copolymer systems that contain two distinct, patterned functionalities. PS-*b*-P2VP dissolved in THF along with 1,5-dihydroxynaphthalene (DHN) were cast into films of P2VP cylinders aligned perpendicular to the substrate.[70] Methanol treatment of the film removes the DHN from the cylinders leading to the creation of nanoporous films. PS-*b*-PMMA cylinders have also been used to create nanoporous films[71, 72] by irradiating the film and then rinsing away the degraded PMMA. Xu et al. [73, 74] have studied the reversible swelling of PAA cylinders aligned perpendicular to the surface in a PS matrix. The oriented cylinders form cavities or mushrooms depending on the pH of the swelling solution.

Here we have focused on characterizing the cavitation phenomenon of micellar thin films as a function of solvent treatment, using PS-*b*-PAA as a model system. We exposed micellar films of various molecular weights to aqueous solutions with a range of pH and ionic strengths as well as to alkyl alcohols of varying chain length, and characterized the resulting film morphologies via atomic force microscopy (AFM). The cavitation process can be reversed by thermally annealing the films. We also visualized the rearrangement of the PAA chains following solvent treatment using transmission electron microscopy (TEM) and demonstrated the availability of the micellar core PAA blocks for participation in post-cavitation conjugation chemistry. We have also examined this cavitation process for several different molecular weights of PS-*b*-P2VP. Cavitation is not limited to spherical micelles, as we demonstrate cavitation of cylindrical PS-*b*-P2VP micelles.

3.2. Experimental Section

3.2.1. Materials

Three poly(styrene-*block*-acrylic acid) diblock copolymers (PS-*b*-PAA) were used in this work with the following molecular weights and nomenclature: PS-*b*-PAA 16.4-*b*-4.5 (M_n (PS) = 16 400 g/mol, M_n (PAA) = 4 500 g/mol, PDI = 1.05), PS-*b*-PAA 42-*b*-4.5 (M_n (PS) = 42 000 g/mol, M_n (PAA) = 4 500 g/mol, PDI = 1.15), and PS-*b*-PAA 66.5-*b*-4.5 (M_n (PS) = 66 500 g/mol, M_n (PAA) = 4 500 g/mol, PDI = 1.07). Three Poly(styrene-*block*-2-vinyl pyridine) diblock copolymers (PS-*b*-P2VP) were used in this work with the following molecular weights and nomenclature: PS-*b*-P2VP 149-*b*-19 (M_n (PS) = 148 500 g/mol, M_n (P2VP) = 19 000 g/mol, PDI = 1.05), PS-*b*-P2VP 81-*b*-21 (M_n (PS) = 81 000 g/mol, M_n (P2VP) = 21 000 g/mol, PDI = 1.16), PS-*b*-P2VP 55-*b*-50 (M_n (PS) = 55 000 g/mol, M_n (P2VP) = 50 000 g/mol, PDI = 1.11). These copolymers, along with their molecular-level characterization data, were purchased from Polymer Source, Inc. Toluene (HPLC grade, 99.8%), n-propanol, Tween 20 and lead(II) acetate trihydrate ($PbAc_2$) were obtained from Sigma-Aldrich Co. Methanol, ethanol, isopropanol, n-butanol, n-octanol, hydrochloric acid (37%), sodium chloride and sodium hydroxide were purchased from Malinckrodt Chemicals. Phosphate buffered saline (PBS) was obtained from VWR international. EZ-link amine-PEO-biotin and EDC were purchased from Pierce Biotechnology. Streptavidin, Alexa Fluor 647 conjugate was purchased from Molecular Probes. Poly(acrylic acid) (PAA) (M_n = 90 000, 25% aqueous solution), Sulfonated polystyrene (SPS) (M_n ~ 70,000) and polyallylamine hydrochloride (PAH) (M_n = 70 000) were purchased from Polysciences. Streptavidin, Quantum Dot 605 conjugate was purchased from Quantum Dot Corporation. All chemicals were used as received. Silicon nitride TEM membrane window substrates were purchased from Structure Probe, Inc. Each substrate (surface area ~ 4.5 mm^2) consisted of a 100-nm-thick amorphous, low-stress Si_3N_4 membrane supported on a 0.2-mm-thick silicon wafer that was back-etched in the center to create the electron transparent Si_3N_4 window (surface area ~ 0.2 mm^2). All aqueous solutions were made using deionized water (> 18 MΩ cm, Millipore Milli-Q).

3.2.2. Microscopy

TEM was performed on a JEOL 2000FX operating at 200 kV. AFM was performed on a Digital Instruments Dimension 3000 Nanoscope IIIA scanning probe microscope using a silicon RTESP cantilever from Veeco Instruements operating in tapping mode. Fluorescence images were obtained using a Zeiss Axiovert 200 microscope equipped with a Roper Scientific CoolSnap HQ CCD Camera.

3.2.3. Sample Preparation

Each of the three different molecular weights of PS-*b*-PAA (listed in the Materials section) was separately mixed with toluene at 25C at a concentration of 10 mg/mL: all of the resulting solutions were slightly cloudy. Solutions of PS-b-PAA 16.4-*b*-4.5 were heated to 140 °C for 20 minutes and allowed to cool in air to room temperature, which results in a change from cylindrical to spherical block copolymer micelles.[21] The other PS-*b*-PAA molecular weights formed spherical micelles at room temperature. PS-*b*-P2VP micelles solution were used at 10 mg/mL without heating. Thin films (25 - 200 nm) were then created by spin-casting the micellar solutions onto glass, silicon or silicon nitride substrates at spin rates of 1600-8000 rpm. The use of electron transparent silicon nitride window grids allows TEM characterization while providing a flat substrate on which films were spin-cast. In order to prevent film delamination experienced when incubating a hydrophobic film on a hydrophilic substrate in a polar solvent, a polyelectrolyte multilayer adhesion layer on a glass substrate was used for some experiments. The polyelectrolyte multilayer film consisted of five bilayers of polyallylamine hydrochloride (PAH) dipped at a concentration of 10 mM on a repeat unit basis at pH 3.5 with 0.1 M NaCl and sulfonated polystyrene (SPS) at a concentration of 10 mM on a repeat unit basis at pH 3.5 with 0.1 M NaCl. A film consisting of three and a half bilayers of PAH dipped at pH 7.5 and a concentration of 10 mM on a repeat unit basis and poly(acrylic acid) dipped at pH 3.5 at a concentration of 10 mM on a repeat unit basis was then deposited on top. This results in a film with a PAH top layer and a water advancing contact angle of 70° as described elsewhere.[75]

The resulting thin film morphology is spherical PAA domains quasi-hexagonally arranged in a PS matrix.[21] For TEM imaging, films were immersed in a saturated lead(II) acetate trihydrate solution for 24 hours to load lead ions into the PAA domains. The lead ions diffuse through the polystyrene corona and bind to the carboxylic acids of the PAA domains. Cavitation is suppressed because the divalent lead ions ionically crosslink the neutralized PAA cores and prevent swelling. This absence of cavitation behavior was also observed in earlier work when di-or tri-valent cations were employed.[21]

For cavitation, film-coated substrates were placed in 20-30 mL of the selected solution for varying amounts of time and dried under vacuum overnight at 25 °C prior to

AFM imaging. Films treated in PBS buffer or solutions pH adjusted with NaOH were rinsed with deionized water prior to drying under vacuum. This rinsing procedure eliminated any precipitated salt on the surface, facilitating AFM imaging of the polymer structure. Nanocavity size was determined using section analysis of AFM images using NanoScope ® Software v5.30. Taking section lines directly through cavities allowed their size to be determined. 50 cavities were analyzed per image to determine nanocavity size and distribution. AFM imaging of control samples was performed with each AFM cantilever to insure consistent imaging results.

Imaging of the back side of cavitated micelle films was accomplished by first casting micelle films onto bare silicon substrates. Spin-casting conditions of 8000 rpm with 1 second ramp times were used to facilitate the formation of monolayer micelle films. Films were treated in 0.004M NaOH (pH = 11.6) for 30 minutes and then dried under vacuum. Plasma treated PDMS was then pressed down (hand pressed, gentle pressure) on top of the micelle film. The PDMS/micelle film/silicon was then submerged in DI water for 5 minutes before pulling the PDMS apart from the silicon substrate. This transfers significant areas of the micelle film onto the PDMS. Micelle films were then immediately dried with an air gun before placing under vacuum to dry before imaging.

The procedure used for coupling the amine-PEO-biotin linker and Streptavidin, Alexa Fluor 647 is described elsewhere.[76] Briefly, films were incubated in 0.5 μg/mL EZ link amine-PEO-biotin linker molecule, 5 mg/mL EDC in MilliQ water for 4 hours at room temperature. Films were washed 5x with MilliQ water and then incubated for 30 minutes at room temperature in PBS buffer at pH 7.4 with 0.5 μg/mL Streptavidin, Alexa Fluor 647 conjugate and 0.1% v/v Tween 20. Films were then washed 5x in PBS. The identical procedure was used for Streptavidin, Quantum Dot 605 conjugation except a 0.1 μg/mL SAvQD solution was used.

3.3. Results and Discussion

3.3.1. Effect of Solvent Quality on the Cavitation of PS-*b*-PAA Spherical Micelles

In previous work,[21] we found that inverse spherical PS-*b*-PAA micelles formed in toluene and cast as close-packed micellar films on solid substrates reorganized upon exposure to alkaline aqueous NaOH solutions. This cavitation process was driven by water swelling of the hydrophilic PAA blocks in the cores of the micelles, and led to fracture of the glassy polystyrene corona at the free surface of the film. To further investigate this reorganization phenomenon, we first examined the role of solvent quality on micelle cavitation. Micellar films were exposed to a series of alkyl alcohols of varying chain length, to allow a continuous variation of the selectivity of the solvent toward each block (Table 3-1).

Solvent	Cavitation Observed	Solubility Parameter, δ (cal/cm^3)$^{0.5}$
Water	Yes	23.4
Methanol	Yes	14.5
Ethanol	Yes	12.7
N-propanol	Yes	11.9
Isopropanol	Yes	11.5
N-butanol	No	11.4
N-octanol	No	10.3
Toluene	N/A	8.9
Acrylic Acid	N/A	12.0
Styrene	N/A	9.3

Table 3-1: Solubility parameters of solvents used in micellar assembly and film treatments

Films of PS-*b*-PAA 16.4-*b*-4.5 micelles cavitated when incubated in methanol, ethanol, n-propanol or isopropanol. In contrast, the micelles did not cavitate, maintaining their as-cast morphology, when exposed to n-butanol or n-octanol. These results are illustrated by the AFM images in Figure 3-2, which show an as-cast micellar film (A) and the results of treating films of PS-*b*-PAA 16.4-*b*-4.5 with isopropanol (B) or n-butanol (C) for 30 minutes, and then drying under vacuum overnight. Extended treatment times (up to 192 hours) produced the same morphologies seen following 30 minute treatment times across all samples. While it is likely that the PAA domains swelled to some degree in n-butanol and n-octanol, this swelling was not significant enough to cause rupture of the glassy PS domains. It is also possible that the solvent could plasticize the PS block such that its increased flexibility led to swelling or stretching rather than cavitation; however, Yaffe and Kramer[77] have shown that when soaked in n-butanol, the T_g of PS decreases from 100 °C to 71 °C and when soaked in n-propanol the T_g is depressed to 81 °C. These T_g values are still well above room temperature. From this fact, we conclude that the effect on the PS caps of exposure to solvent does not play a significant role in the suppression of cavitation in n-butanol treated films and the change in cavitation behavior between isopropanol and n-butanol must be due to differences in PAA swelling. These results illustrate that the polarity of the solvent plays a major role in the swelling and cavitation of the PAA domains, as the alcohols represent a homologous series of polar molecules with systematically variable polarity and hydrophobicity.

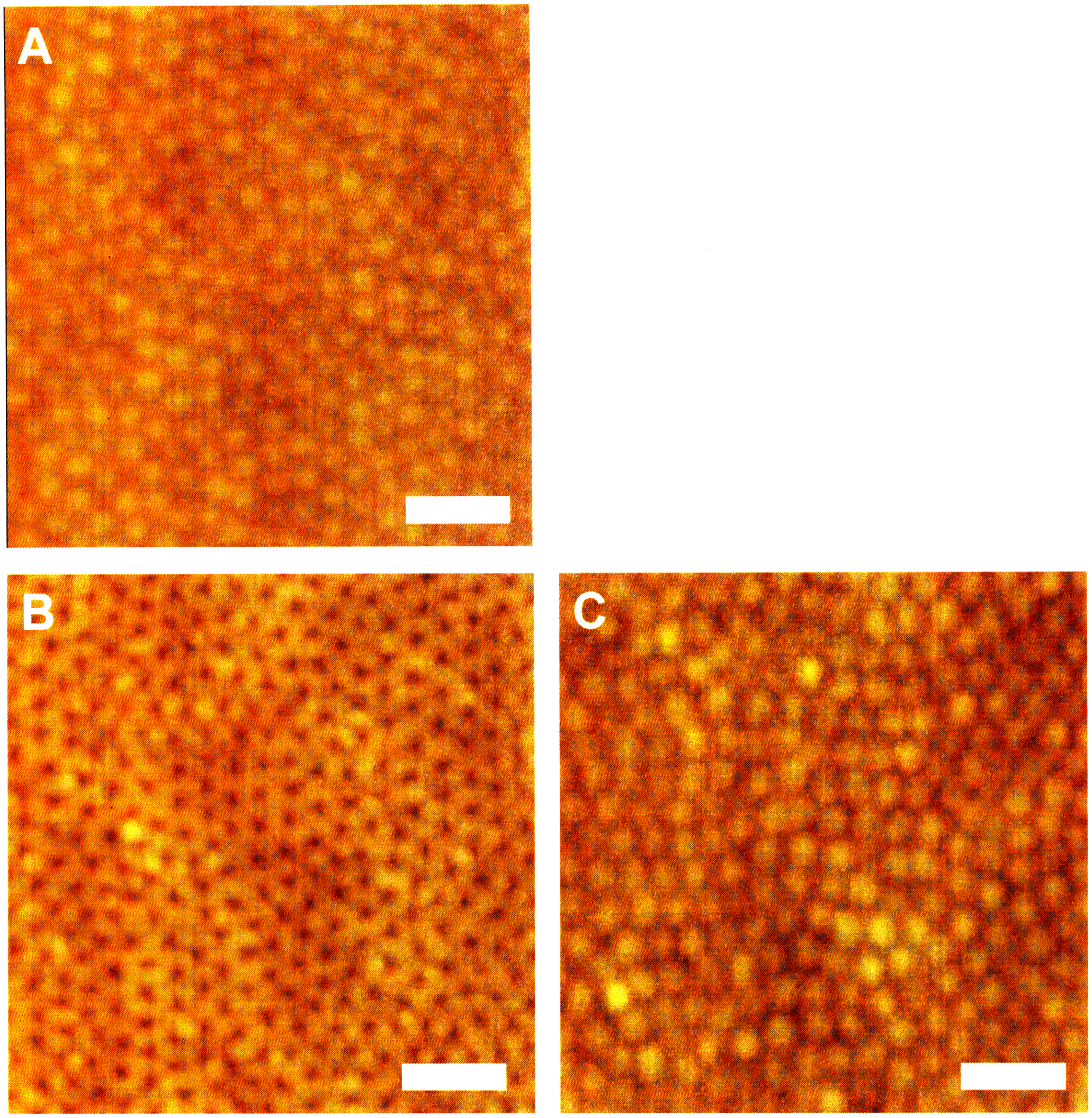

Figure 3-2: AFM height images of PS-*b*-PAA 16.4-*b*-4.5 films (A) as-cast and treated in (B) isopropanol and (C) n-butanol for 30 minutes. Scale bars are 100 nm and height scales are 20 nm.

3.3.2. Effect of pH and Ionic Strength of Aqueous Solution on the Cavitation of PS-*b*-PAA Spherical Micelles

Next, we examined the effect of varying the solvent interaction with the PAA blocks by exposing micellar films to aqueous solutions of varying pH and ionic strength. Because PAA is a weak polyacid, the charge along the polymer backbone increases with increasing pH. This charging phenomenon drives the polymer chain to a more extended conformation in order to minimize the electrostatic interactions between neighboring repeat units along the chain. We thus expect swelling of the interior PAA block of the micelle and cavitation to be favored as pH increases.

The morphology of cavitated PS-*b*-PAA 16.4-*b*-4.5 polymer films and the degree to which the micelle opens depends on pH, as seen in the AFM images in Figure 3-3 for the case of films treated for 30 minutes in aqueous solutions ranging in pH from 2.0 to 11.6 at low ionic strength. For treatment in pH 2.0 HCl (ionic strength, I = 10 mM), seen in Figure 3-3A, only a very subtle depression can be seen on the top of the micelles, suggesting that a morphological rearrangement has occurred but to a much lower degree than in the films treated at higher pH. In comparison, films treated with pH 5.6 deionized water (Figure 3-3B), exhibited easily distinguishable cavities and the PS corona of each micelle was fractured. This fracture and rearrangement was even more evident for the film treated in pH 7.4 NaOH (I = 3 μM) (Figure 3-3C). In the film treated in pH 11.6 NaOH (I = 4 mM) (Figure 3-3D), film rearrangement resulted in a morphology that was significantly different from the other films studied. In films treated in pH 2.0 - 7.4 the boundaries between adjacent micelles remains defined, but for pH 11.6 treated films the boundaries are difficult to determine and, with the exception of the hexagonal arrangement, it has almost completely lost is resemblance to the as-cast films. Figure 3-3E shows the cavity diameter for PS-*b*-PAA 16.4-*b*-4.5 films treated in pH 5.6 deionized water, pH 7.4 NaOH and pH 11.6 NaOH, as determined from analyzing the AFM data. These values are only approximate due to the comparable size of the cavities and the AFM tip; however, a clear trend of increasing cavity diameter with increasing pH of the solution is observed. This is consistent with the increased swelling of PAA with increasing pH. PAA domain swelling and chain stretching mechanisms have been show to create topologically similar structures in uncapped PAA cylinders aligned perpendicular to the surface in PS-*b*-PAA thin films.[74] Cavitation of micelle films at one pH followed by exposure of the film to a second aqueous solution with a higher pH than the initial solution led to a morphology identical to that resulting from a single treatment in the higher pH solution. The PAA chains swell more when exposed to the higher pH solution and thus further cavitate the PS caps compared to their state after the first solution treatment at a lower pH. However, sequential exposure of a film to a higher pH followed by a lower pH left the film in the higher-pH cavitated structure, presumably because the PAA chains already have ample solution volume available to them to swell.

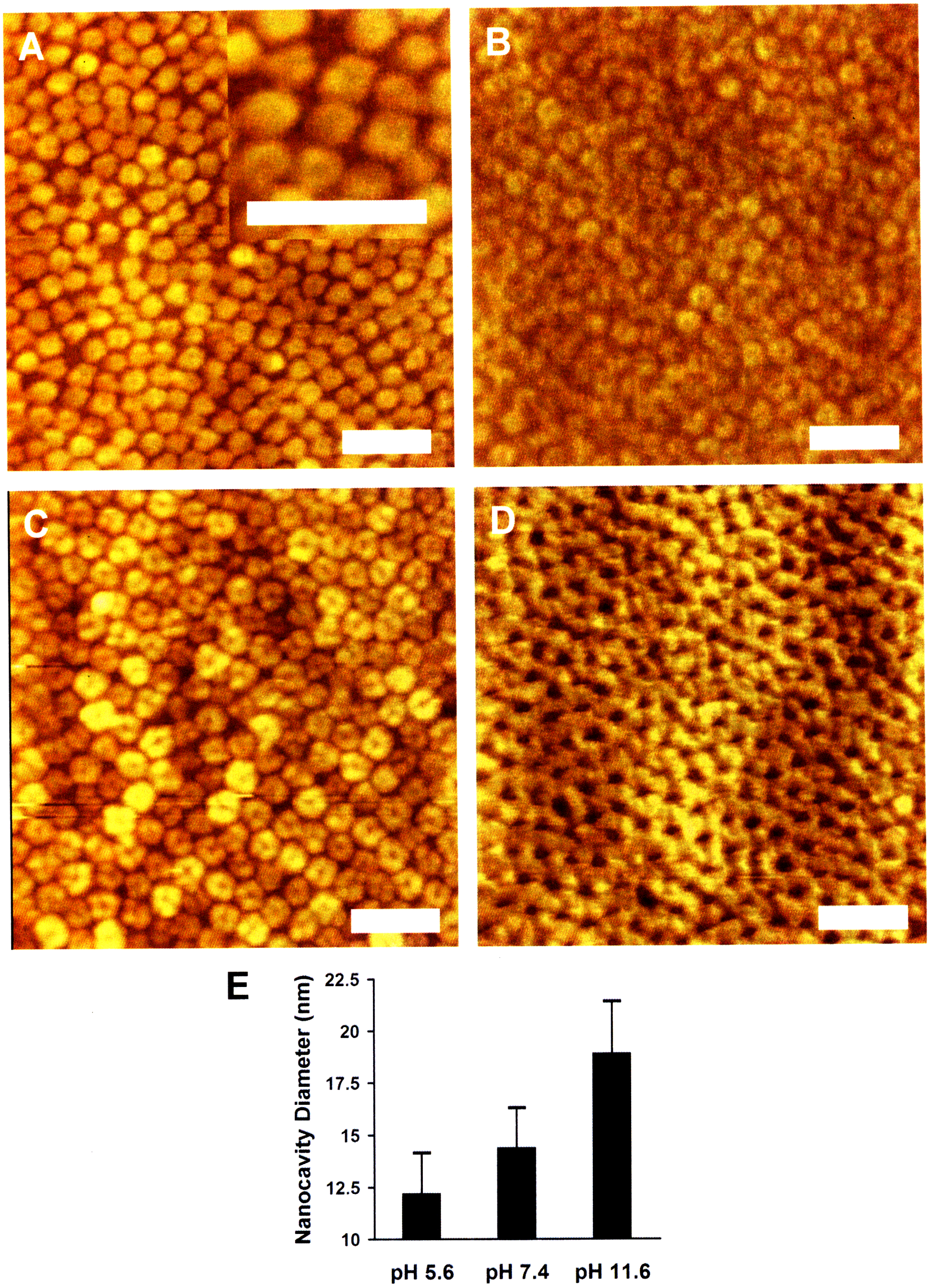

Figure 3-3: AFM height images of PS-*b*-PAA 16.4-*b*-4.5 films treated for 30 min in (A) pH 2.0 HCl, (B) MQ water pH 5.6, (C) pH 7.4 NaOH and (D) pH 11.6 NaOH. Scale bars are 100 nm and height scales are 20 nm. (E) Size of nanocavities resulting from described treatments for PS-*b*-PAA 16.4-*b*-4.5 determined from AFM images.

Ionic strength, like pH, plays a role in the swelling of polyelectrolyte brushes, hydrogels and other polyelectrolyte films. For many weak polyelectrolyte systems, increasing the ionic strength of the solution leads to a decrease in the swelling of films. However, for weak polyelectrolyte brushes, including poly(acrylic acid), the opposite behavior has been predicted[78-83] and observed[84, 85] at low ionic strengths. For PAA specifically, brush swelling has been predicted and observed to be greater for ionic strengths approaching 1 M compared to the swelling at <1mM at constant pH.[81] This behavior is determined by two opposing effects as the ionic strength increases. The first is a decrease in the electrostatic potential (increased ionic screening), which would decrease the swelling of the brush. The second is the charge state of the polymer itself. For a weak polyacid, as the ionic strength of the solution is increased, the pKa of the polymer is shifted to a lower pH and the charge of the polymer increases. This charging of the polymer chain and accumulation of associated counterions in the PAA domain leads to a higher intrabrush osmotic pressure and increased brush swelling. It is this latter effect that dominates at low ionic strength for weak polyelectrolyte brushes and leads to increased swelling with increased ionic strength. At very high ionic strengths (> 1M) swelling will begin to be dominated by the decrease in electrostatic potential (increased ionic screening) and swelling will decrease. The ionic strength where this behavior is predicted can range significantly and can be 10M or higher in some cases. We expected that a similar behavior could prevail in micellar films, as the PAA chains are in a brush-like state pinned at the PS-PAA domain boundary.

In order to investigate what effect ionic strength has on the swelling and cavitation behavior of PS-*b*-PAA micellar films, we treated 16.4-*b*-4.5 films in pH 7.4

phosphate buffered saline (I = 150mM) (Figure 3-4). The morphology of the resulting film more closely resembles that of the films treated in pH 11.6 NaOH (I = 4 mM) than the films treated in pH 7.4 NaOH (I = 3 μM). This is consistent with the behavior of weak polyelectrolyte brushes discussed above. By increasing the ionic strength of the solution while remaining in the low ionic strength regime as applicable to PAA, the swelling of the PAA domain increases, leading to a morphology that resembles a film treated at higher pH but lower ionic strength. Similar results were obtained for micelle films treated with pH 7.4 NaCl solutions of 10 – 150 mM (data not shown). We have also treated micellar films with high ionic strength solutions to see if we can observe the deswelling behavior predicted at high ionic strengths. We tested solutions as high a 1M NaCl and still observed a higher degree of swelling (Figure 3-4) compared to films treated in pH 7.4 NaOH (I = 3 μM).

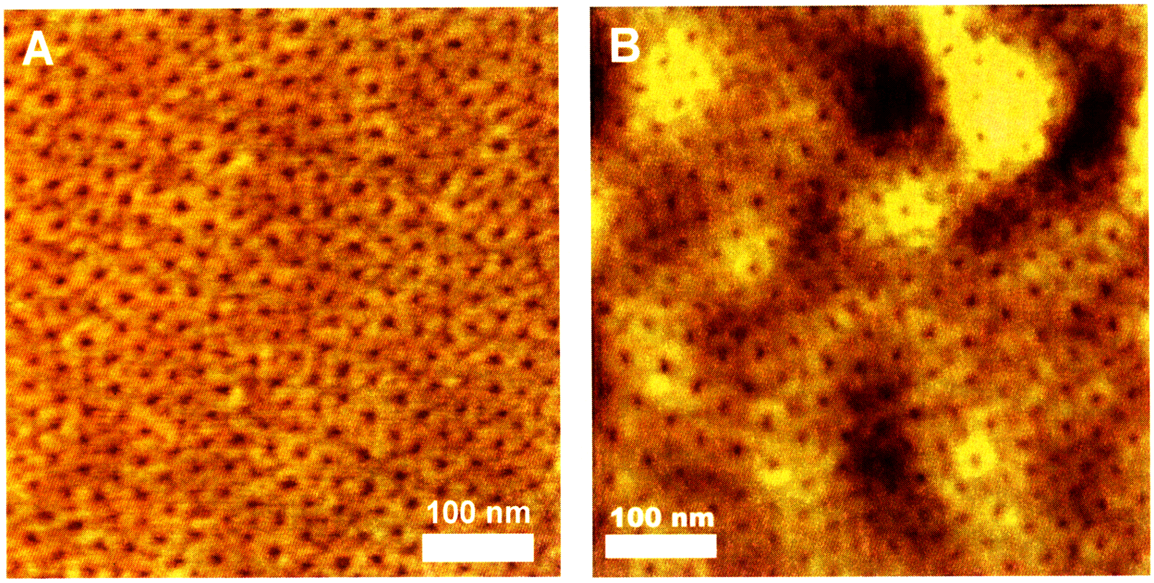

Figure 3-4: AFM height images of PS-*b*-PAA 16.4-*b*-4.5 film treated in (A) PBS buffer (I = 150 mM) at pH 7.4 for 30 min and (B) 1 M NaCl for 30 min. Height scale is 20 nm.

Because of the potential for this block copolymer system for biological applications, films were incubated in RPMI 1640 cell media with 10% fetal calf serum (FCS) to investigate the behavior of the micellar films in a more physiological environment. RPMI has a pH of 7.2 and contains several mono- and multivalent buffers as well as amino acids, vitamins, and glucose with a total ionic strength around 150 mM. Incubation of PS-*b*-PAA 16.5-b-4.5 micelle in RPMI 1640 w/10% FCS resulted in cavitation shown in Figure 3-5.

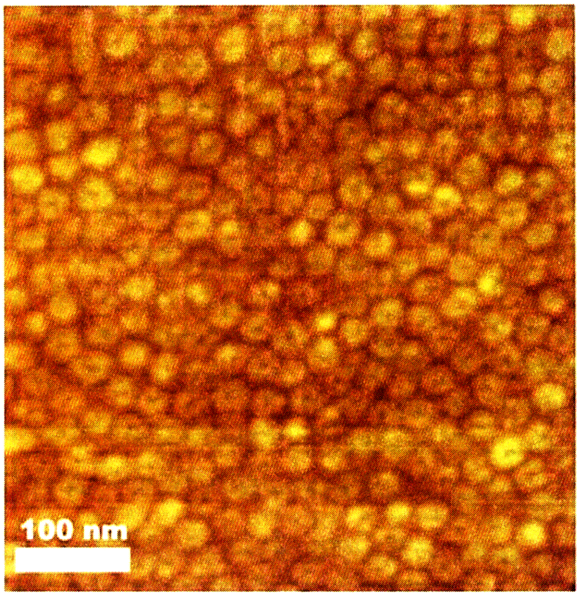

Figure 3-5: Cavitation of PS-*b*-PAA 16.5-*b*-4.5 resulting from 30 min treatment in RPMI 1640 cell media with 10% fetal calf serum.

3.3.3. Cavitation and the Variation of PS-*b*-PAA Molecular Weight

The reorganization of micellar films in response to aqueous solutions of varying pH demonstrates that selectively varying the interaction of the solvent with the core block of the micelles can substantially modulate the final structure of the cavitated films. However, the glassy PS corona of the micelles also plays a role in controlling cavitation behavior and morphology. By increasing the PS block length while holding the PAA block length constant, the PS:PAA ratio of the polymer increases. As a consequence, for each PAA chain there is more PS present, and the swelling of the PAA chain required to fracture the PS caps will increase, and thus we expect the pH of the solution required to cavitate the micelle will be higher. In addition, the critical molecular weight for entanglement coupling in PS is about 36 kg/mol;[86] as a result varying the PS block molecular weight around this value would be expected to produce significant changes in the polystyrene's ability to mechanically resist swelling of the encapsulated PAA core. To test this hypothesis, we examined the cavitation behavior of PS-*b*-PAA 42-*b*-4.5 and 66.5-*b*-4.5 micelles following exposure to aqueous solutions of varying pH (Figure 3-6). Unlike PS-*b*-PAA 16.4-*b*-4.5 micelles, PS-*b*-PAA 42-*b*-4.5 does not cavitate in pH 5.6 deionized water, even after long treatment times (up to 168 hours). However, treating with a pH 7.4 NaOH solution triggered cavitation. When the PS block length increased to 66.5 kg/mol, the resulting micellar films did not cavitate in NaOH solution with a pH as high as 9.6, but did cavitate upon exposure to pH 11.6. At sufficiently large PS molecular weights, cavitation might be suppressed at all pH values.

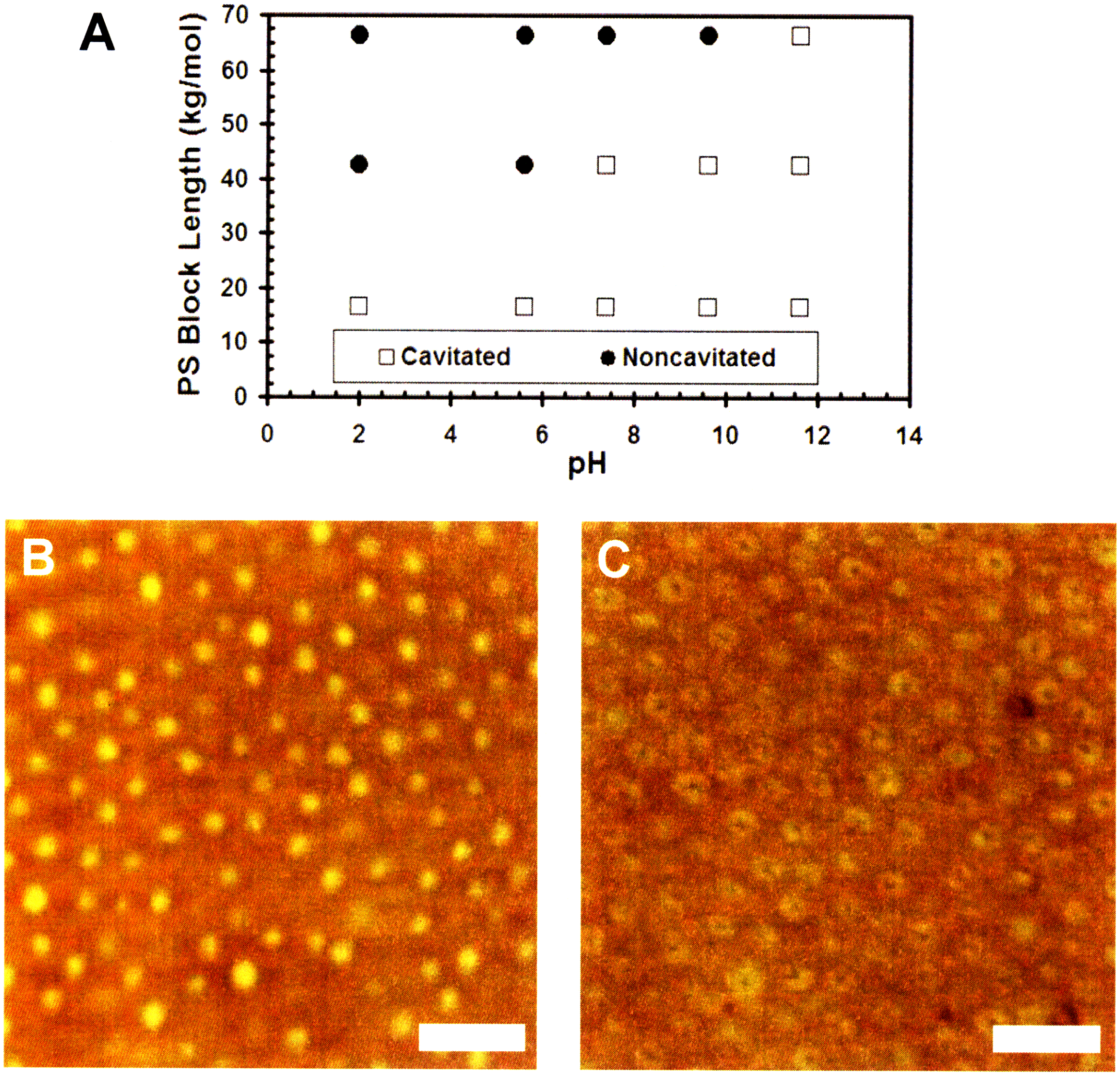

Figure 3-6: Cavitation behavior of PS-*b*-PAA with a PAA block of M_n = 4.5 kg/mol and changing PS block length for aqueous solution treatments of varying pH. AFM height images of PS-*b*-PAA 66.5-*b*-4.5 after a 30 minute treatment in (B) pH 9.6 NaOH solution and (C) pH 11.6 NaOH solution. Scale bars are 100 nm and height scales are 20 nm.

3.3.4. TEM Visualization of PAA Chain Rearrangement Upon Aqueous Solution Treatment

In order to further investigate the rearrangement of the polymer thin film upon exposure to aqueous solution, we examined the selective loading of multivalent metal ions into micelle films pre- and post-cavitation. The TEM images in Figure 3-7 show a

PS-*b*-PAA 16.4-*b*-4.5 films that has been exposed to aqueous 0.4 mM lead(II) acetate solution and a PS-*b*-PAA 16.4-*b*-4.5 film that was exposed to pH 11.6 NaOH and subsequently to an aqueous lead(II) acetate solution. AFM images (not shown) confirm that the film in Figure 3-7A has the familiar as-cast morphological topology (Figure 3-2A) of quasi-hexagonal closed-packed micelles and that the film in Figure 3-7B exhibits the expected cavitated morphology (Figure 3-3). For the as-cast films, the lead staining yields a circle with small clusters visible inside the circular area of the micelle. The cavitated film exhibits a different staining pattern characterized by a ring structure. We believe this ring structure is a result of the cavitated morphology that leaves a cylinder-like cavity, the walls of which are covered with a PAA brush. This proposal is consistent with the observation in Figure 3-7B that the walls of the cylinder-like cavity appear dark with light staining in the center.

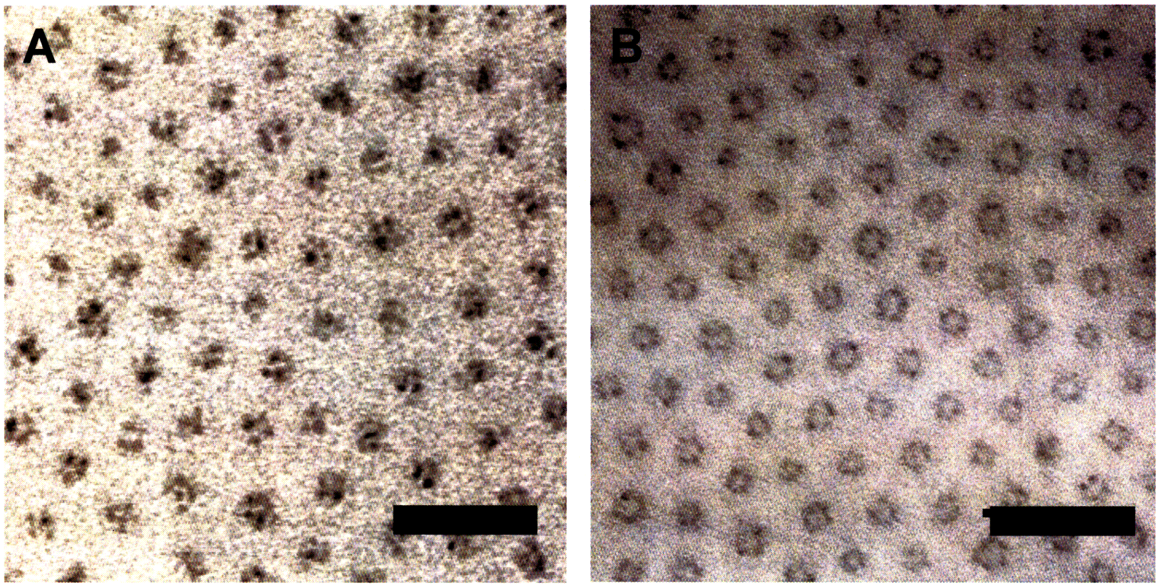

Figure 3-7: TEM images of PS-*b*-PAA 16.4-b-4.5 films stained with lead acetate. Image A is of as-cast film and B is a film that has been cavitated in pH 11.6 NaOH before staining. Scale bars are 100 nm.

3.3.5. Reversibility of the Cavitation Process via Thermal Annealing

The results described above characterize the swelling of PAA domains leading to the fracture of the PS caps, creating arrays of nanocavities. To investigate whether the reverse process can occur (cavitated micelles returning to their as-cast spherical morphology) we thermally annealed cavitated PS-*b*-PAA 16.4-*b*-4.5 thin films. The T_g of bulk PS is about 100 °C, so it is expected that the PS chains on the free surface of our ultrathin films would be sufficiently mobile during annealing at 100 °C. Micellar films that had first been treated in pH 7.4 NaOH were thermally annealed at 100 °C for 24 hours. After annealing, the films were imaged in AFM and the morphology had returned to that of the as-cast films (Figure 3-8). Annealed films that had returned to this as-cast morphology, cavitated a second time upon treatment in pH 7.4 NaOH (I = 3μM).

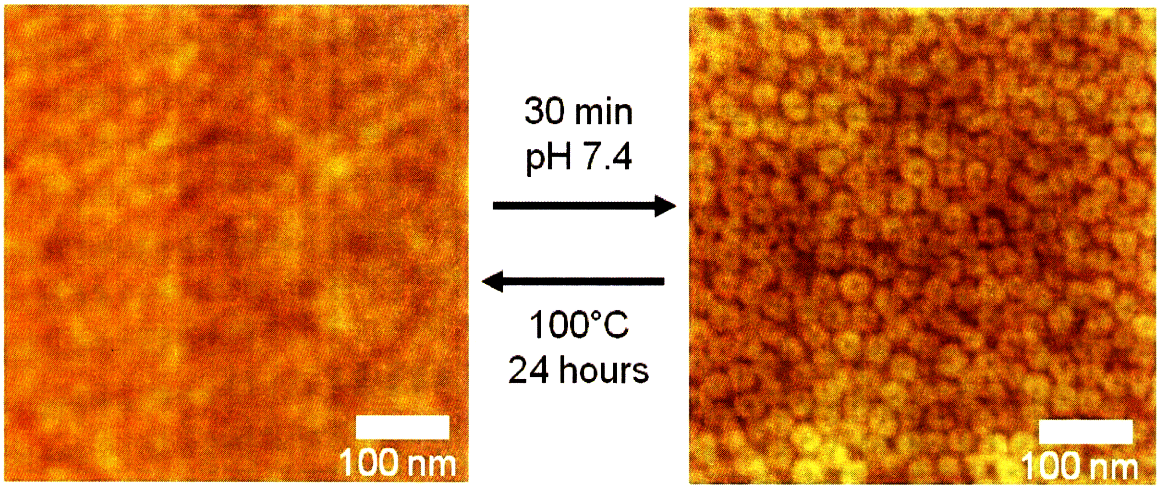

Figure 3-8: Schematic showing cavitation of PS-*b*-PAA 16.5-*b*-4.5 micelle and subsequent annealing at 100 °C for 24 hours, which returns film to the as-cast morphology of spherical micelles.

3.3.6. Cavitation of Nonclose-packed PS-*b*-PAA Micelles

Until now we have described cavitation of continuous close-packed micellar films. However, in Chapter 2 (Figure 2-4) we also demonstrated the ability to create micelle films where individual micelles were separated by 100+ nm distances from their nearest neighbor. It is possible that the caviation phenomena would be limited to close-packed films as neighboring micelles would provide mechanical strength which would limit swelling in the direction parallel to the substrate. This would lead to preferential swelling normal to the substrate and cavitation. To examine the rearrangement of micelle films in nonconfined geometries, we created films with large intermicelle spacings by spin-casting at 1600 rpm with a 1 second ramp time casting from 0.01mg/mL PS-b-PAA solutions in toluene. Films were subsequently treated in PBS to cavitate the micelles (Figure 3-9). The textured background in the images is the polyelectrolyte multilayer that is discussed in the experimental section as it becomes rough on the nanometer length scale upon aqueous solution treatments and subsequent drying. The cavitation does not appear as clear in the height image (Figure 3-9A) compared to close-packed films. This is because the depth of the cavity as indicated by AFM is small compared to height range of the image. In images of close-packed films the height scale is 20 nm as compared to 30 nm here because in close-packed films the low points of the image are the creases between micelles, whereas here they are the substrate. So this larger overall height scale results in a lower color contrast for the cavities. Cavitation is easily observed in the phase image (Figure 3-9B), similar to the images of close-packed films.

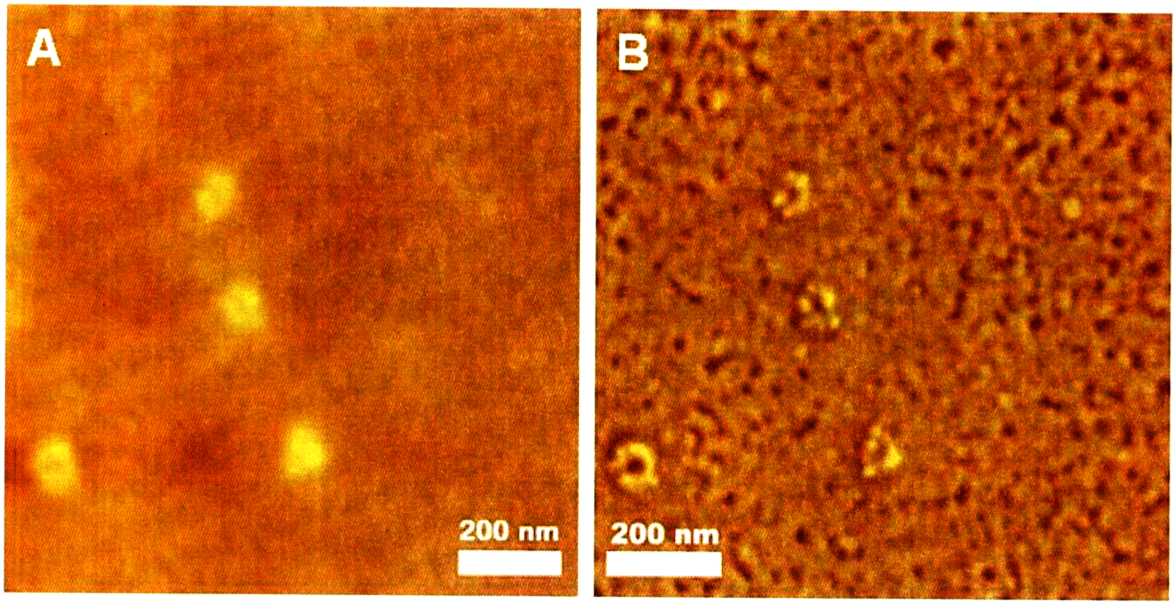

Figure 3-9: Cavitation of individual micelles upon treatment for 30 min in PBS. Film was cast from 0.01 mg/mL PS-*b*-PAA 16.5-*b*-4.5 solution in toluene at 1600 rpm with a 1 second ramp. (A) Height image with 30 nm height scale. (B) Phase image with 50° scale.

3.3.7. Investigation of the Underside of Cavitated PS-*b*-PAA Micelle Films

AFM imaging of films has allowed us to characterize the upward facing morphology of PS-*b*-PAA micelles. However, we have not been able to observe the effect of these treatments, if any, on the side of the micelle film facing down on the substrate. Li et al. [68] claims to have imaged the back side of PS-*b*-P2VP micelle films after solution treatment and observed that the cavity observed on the top side of the film persist across the entire film. To investigate this we have transfered cavitated micelle films to PDMS substrates, inverting the film and allowing the underside of the micelle film to be imaged via AFM. Figure 3-10 is an AFM image of the back side of a PS-*b*-PAA films. The morphology is that of an as-cast morphology. There are two main concerns with this procedure. First, because the film is exposed to water it is possible that the film could cavitate after being transferred to PDMS and result in the observation of a cavitated morphology that was not present on the back side of the film when it was on silicon, giving a false positive result for cavitation. The other is that a monolayer micelle film is needed. In AFM we only observe the top layer of micelles and can offer no insight into any possible rearrangement of micelles that are between the substrate and the top of the film. In this experiment we are interested in observing the morphology of the back side of micelles that are cavitated on the top side. This is not achieveable unless we have a single layer of micelle. We believe that we have a monolayer of micelles because we see cracks in the PS-*b*-PAA film (Figure 3-10) that expose what is underneath the first micelle layer and we do not see any significant topography, suggesting that we are imaging the PDMS substrate. The depth of these cracks is less than 15nm, which is smaller than the ~20nm thickness that has been previously demonstrated in our lab for monolayer PS-*b*-PAA thin films and observed for patterned PS-b-PAA films in Figure 2-13. This suggests that we do indeed have a monolayer micelle film and that the back side of the film that is originally in contact with the substrate does not undergo any siginificant rearrangement or cavitation.

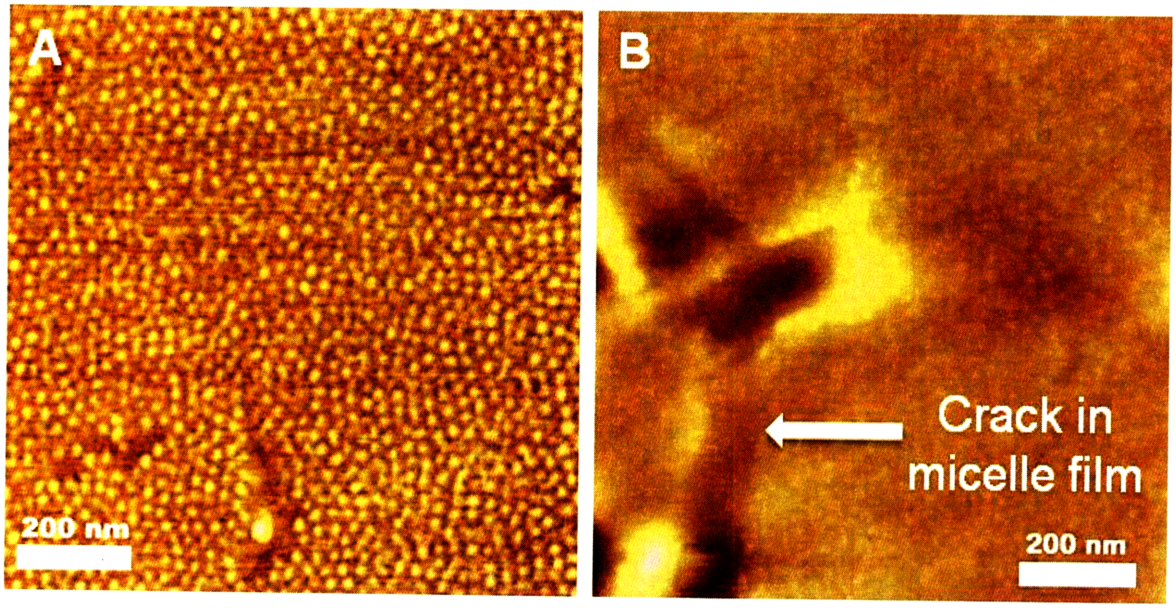

Figure 3-10: AFM imaging of the back side of an PS-*b*-PAA 16.5-b-4.5 micellar thin film that was cast on silicon and treated in 0.004M NaOH (pH = 11.6) for 30 minutes and

then transferred to a PDMS substrate to expose the side of the film that had been down on the silicon substrate. (A) Height image with 7.5 nm height scale. (B) Height image with 20 nm height scale showing a crack in the micelle film.

3.3.8. Creation of Protein Arrays from Cavitated Micellar Thin Films

Cavitation of the PS caps and the resulting exposure of the PAA chains produces a nanopatterned surface of PS and PAA domains. EDC, a carbodiimide, zero-length cross linking agent that couples primary amines and carboxylic acids, can then be utilized to selectively bind primary amine functionalized molecules to the exposed carboxylic acid moieties of the PAA domains of our cavitated films. This capability, combined with our previous work[54, 55] in chapter two that demonstrated control over the center-to-center spacing and PAA domains size of PS-*b*-PAA thin films, points to the potential to create controlled 2-D nanopatterned arrays of many different molecules. To demonstrate this concept, we have selectively bound a streptavidin-Alexafluor conjugate to a cavitated PS-*b*-PAA 16.4-*b*-4.5 film. First, a primary amine functionalized triethylene glycol biotin linker molecule was covalently-linked to the surface using EDC chemistry, and then the film was incubated in a streptavidin-Alexafluor solution. These films were then imaged in a fluorescence microscope to confirm binding as seen in Figure 3-11. The cavitated film in Figure 3-11A was treated with the complete coupling reaction followed by streptavidin binding. The strong fluorescence of the conjugated film confirms both the availability of the PAA groups to the solution and the ability to functionalize these nanocavities post-cavitation. Control reactions were performed where no biotin linker molecule (Figure 3-11B) or no streptavidin-alexafluor conjugate (Figure 3-11C) were present, respectively. The absence of fluorescence intensity in these films indicates that non-specific binding of both the biotin linker molecule and the strepatvidin-alexafluor to the cavitated micelles films was low.

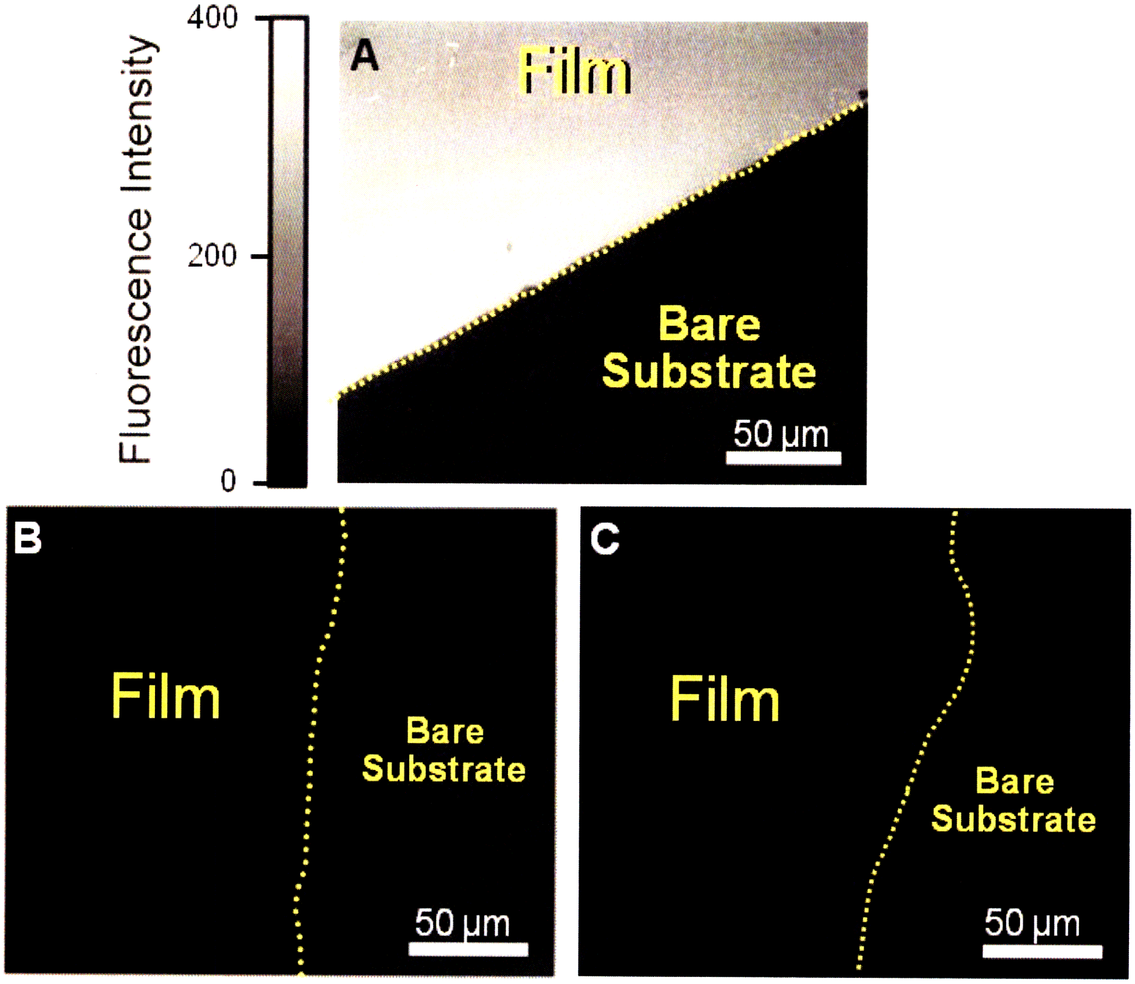

Figure 3-11: Fluorescence images demonstrating the specific coupling a streptavidin, alexa fluor conjugate to the carboxylic acid groups of a cavitated PS-*b*-PAA (16.4-*b*-4.5) film via a NH_2-triethylene glycol-biotin linker molecule. The substrate is a polyelectrolyte multilayer on glass as described in the experimental section. Exposure time is 400 ms. (A) Full reaction scheme. (B) Control reaction with no EDC. (C) Control reaction with no NH_2-Ethylene glycol-biotin.

We have also characterized the coupling of streptavidin-alexa fluor using AFM. For control reactions where binding is not detected by fluorescence, we observe a micelle film that appears unchanged from what we have seen for cavitated micelle films (Figure 3-12B). However, for the full reaction scheme where bright fluorescence was observed we are no longer able to see the familiar nanocavities (Figure 3-12A). Instead we see a blurry image where they are some globular bumps that are on the order of 10-15 nm. This corresponds to the streptavidin protein that is bound to the carboxylic acid groups of the PAA. Certainly, observing the protein using the AFM is not a sensitive means of detecting protein on the surface especially for our films where we have significant topology on the same length scale as the size of the protein (hydrodynamic diameter of 5-6 nm) which can make detection difficult, but the difference between the films in Figure 3-12 is significant and confirms our fluorescence results.

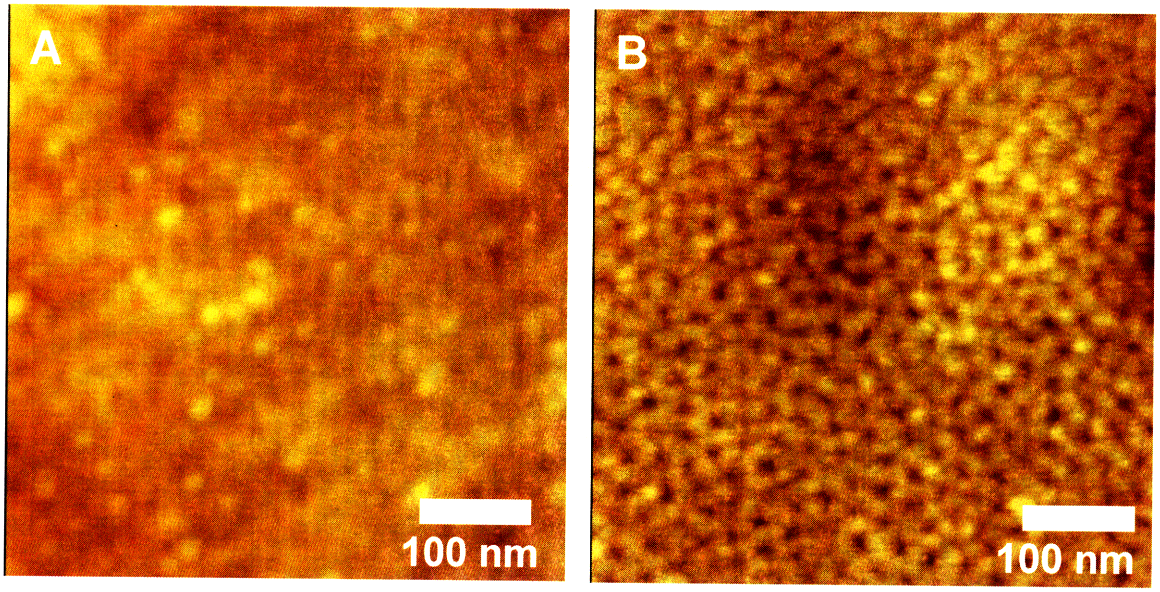

Figure 3-12: AFM height images of streptavidin-alexa fluor conjugate bound to PS-*b*-PAA micellar thin film via and NH_2-triethylene glycol-biotin linker molecule where (A) is height image a film which has been treated with the full reaction scheme (corresponding to image A in Figure 3-6) and (B) is a film that has been treated with a control reaction with no EDC (corresponding to image B in Figure 3-6).

Streptavidin-quantum dots (SAvQD) have also been coupled to cavitated PS-*b*-PAA micellar thin films using the same procedure where we first coupled a primary amine functionalized triethylene glycol biotin linker molecule to the surface using EDC chemistry. The surface was then washed and incubated in with a SAvQD solution. Figure 3-8 show fluorescence microscope images demonstrated the selective binding of SAvQDs to cavitated PS-*b*-PAA micellar films. Again, we see high florescence signal from films treated with the full reaction conditions (Figure 3-8A) and low signal from films treated with control reaction conditions without either the biotin linker molecule (Figure 3-7B) or the streptavidin-alexafluor conjugate (Figure 3-6C).

SAvQDs are large enough (20-30nm) to easily been seen via AFM imaging, so we performed imaging of SAvQD conjugated films. A significant amount of SAvQDs were visible on the surface although they were at a density much less than 1 SAvQD per micelle (Figure 3-14). This is probably a result of using a low concentration of SAvQDS (0.1 μg/ml, 5x lower then the concentration of streptavidin, alexa fluor used) in order to eliminate non-specific binding of SAvQDs to the surface. This appears to be a lower density than was observed for SAv-Alexafluor conjugates (Figure 3-12). However, the fluorescence intensity is higher for bound SAvQDs compared to bound SAv-alexa fluor conjugates (Figure 3-11A) because of the higher fluorescence intensity per particle for the QDs versus the limited number of alexa flour molecules per protein.

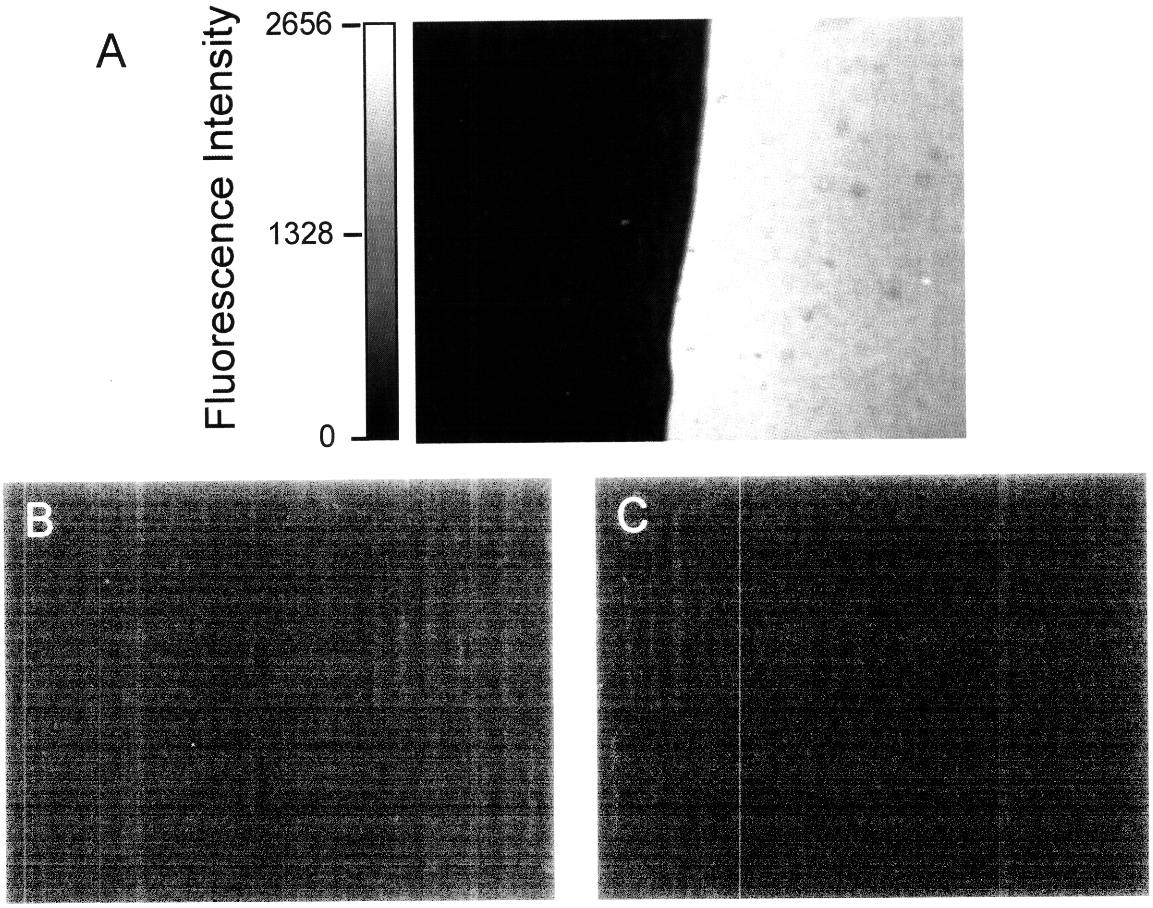

Figure 3-13: Fluorescence images demonstrating the specific coupling a streptavidin, quantum dot 605 conjugate to the carboxylic acid groups of a cavitated PS-*b*-PAA (16.4-*b*-4.5) film via a NH_2-triethylene glycol-biotin linker molecule. The substrate is a polyelectrolyte multilayer on glass as described in the experimental section. Exposure time is 400 ms. (A) Full reaction scheme. (B) Control reaction with no EDC. (C) Control reaction with no NH_2-Ethylene glycol-biotin. Images (B) and (C) are from the center of the polymer films, so there is no film edge in the image like in Figure 3-11.

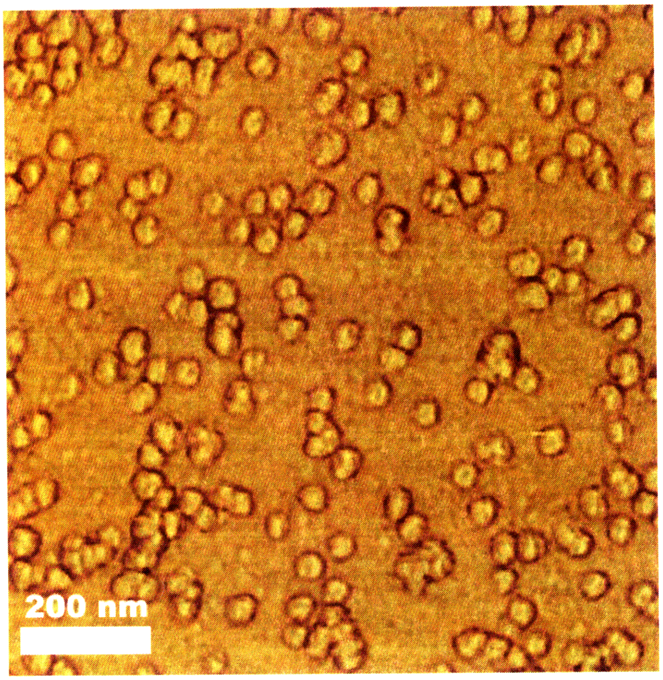

Figure 3-14: AFM phase image of SAvQDs coupled to a cavitated PS-*b*-PAA micellar thin film.

3.3.9. Cavitation of Spherical and Cylindrical PS-*b*-P2VP Micelles

Using PS-*b*-PAA as a model system, we have studied the formation of nanocavities. In principle, cavitation could be observed in a wide variety of amphiphilic polymer systems where micelle are cast from a solvent selective for one block and then treated in a solvent selective for the opposite block. Others[67,68] have subsequently published work demonstrating cavitation of PS-*b*-P2VP spherical micelles cast from toluene. We have also observed this behavior for several different molecular weights of PS-*b*-P2VP. Figure 3-15 shows AFM height images of as-cast micelles and micellar films treated in 0.004M NaOH (pH = 11.6) of 81-b-21 PS-*b*-P2VP (Figure 3-15A, B) and 149-b-21 PS-*b*-P2VP (Figure 3-15C, D).

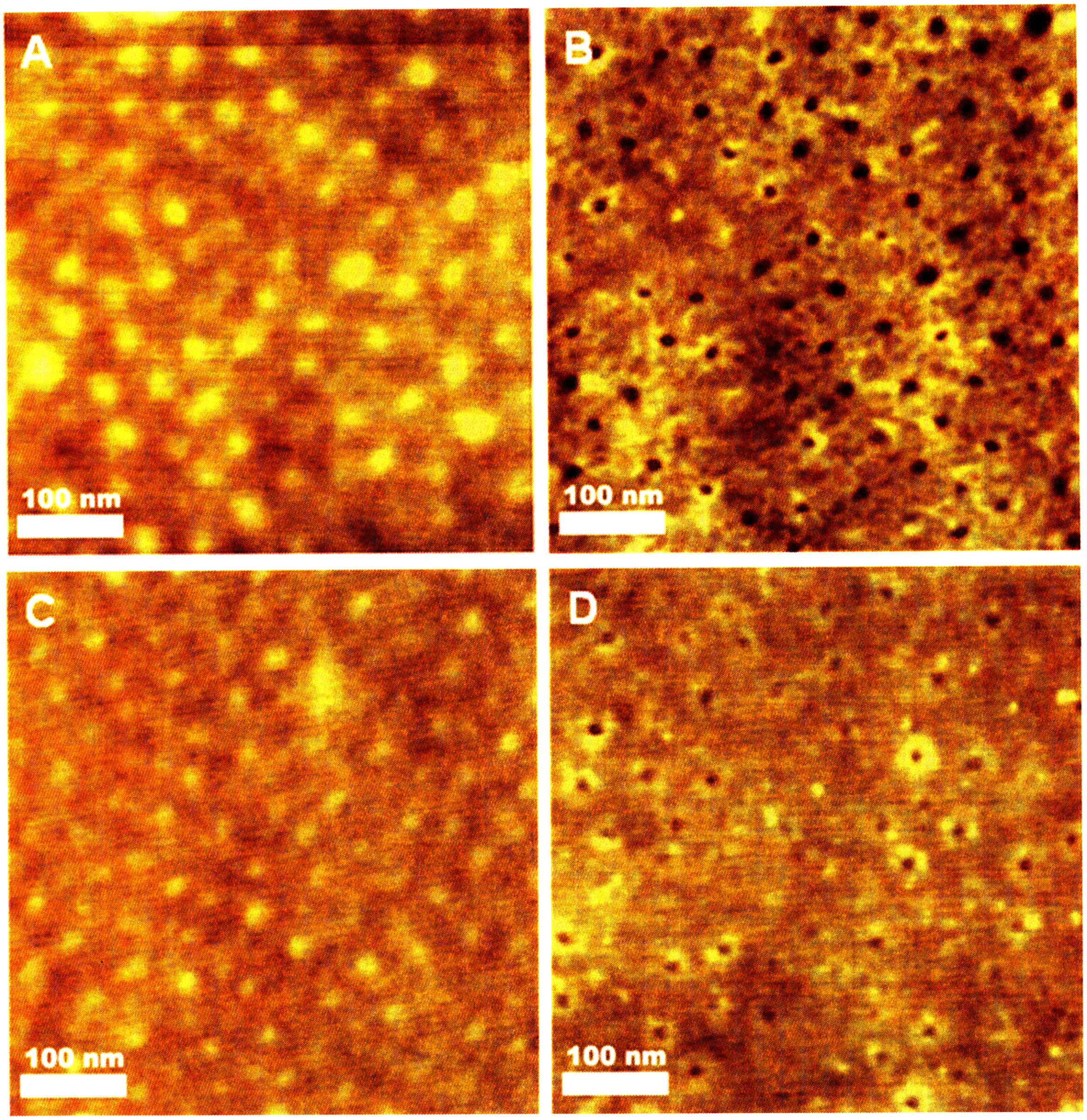

Figure 3-15: (A) AFM height image of 81-*b*-21 PS-*b*-P2VP micelles as-cast and (B) treated in pH 11.6 NaOH. (C) AFM height image of 149-*b*-21 PS-*b*-P2VP micelles as-cast and (D) treated in pH 11.6 NaOH. Height scale for all images is 7.5 nm.

Cavitation is not limited to spherical morphologies, as we have observed this phenomenon in cylindrical micelles as well. The as-assembled PS-*b*-P2VP 55-*b*-50 has evidence of some wormlike structures mixed with spherical structures (Figure 3-16A). When a micelle solution in toluene was put into contact with a ovalbumin protein solution in PBS overnight without mixing the two phases, predominantly cylindrical micelles were formed (Figure 3-16B). The amount of ovalbumin encapsulated in the micelle was quite small, about 100 ng per mg of polymer (0.01 % wt/wt or 1 protein molecule per 4300 polymer chains). So it is possible that water incorporation also played a role in changing the polymer morphology. When treated in PBS for 16 hours (shorter treatment times would have likely resulting in cavitation, but were not explored) the cylindrical micelle underwent a rearrangement similar to that observed for spherical micelles (Figure 3-16C). Cavities are seen along the entire length of the cylindrical micelles. All experiments that resulted in cylindrical micelles with PS-*b*-P2VP 55-b-*50* came from a single copolymer solution. When new solutions were made in an attempt to repeat these results, spherical micelles were obtained (Figure 2-7). It is not know what cause the differences in micelle morphology, although it is possible that a contaminant led to the formation of cylindrical micelles. We experienced a similar inconsistency in polymer morphology with PS-*b*-PAA at a different point in time that went away when acquiring fresh toluene, illustrating the potential effect of contamination on micelle assembly.

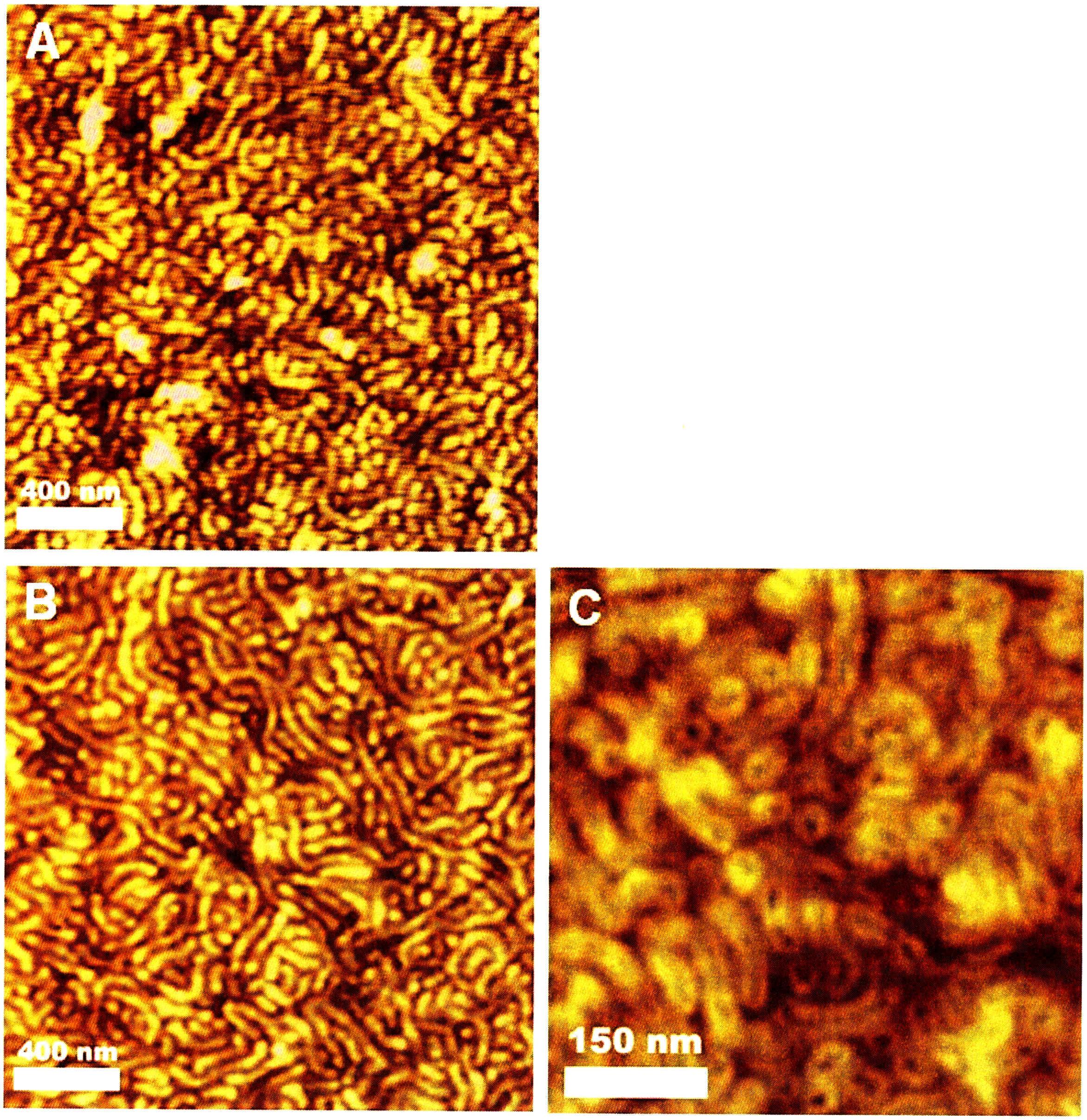

Figure 3-16: Cavitation of cylindrical micelles of PS-*b*-P2VP 55-*b*-50 cast from toluene after exposure to an aqueous solution of ovalbumin protein.

3.4. Conclusions

AFM imaging was successful in capturing the morphological rearrangement of PS-*b*-PAA micellar thin films that were exposed to alcohols and aqueous solutions of varying pH and ionic strength. We have shown that solvent polarity, pH of the aqueous solution, and the ionic strength of the solution determine whether a micellar film of a given molecular weight and composition will cavitate and expose the PAA chains to film surface. The resulting cavity size is also dependent on these variables. The results support the contention that the cavitation behavior is a result of PAA domain swelling which induces fracture and rearrangement of the PS caps. At constant PAA block molecular weight, varying the molecular weight of the PS domains also affects cavitation behavior of the micelles. A higher pH solution is required to cavitated micelles with larger PS molecular weights. The cavitation process is thermally reversible; annealing films at a temperature near the T_g of the PS block returned the films to the original pre-cavitated morphology. The morphological rearrangement was also visualized by TEM imaging of films selectively stained for PAA. We also demonstrated selective linking of a streptavidin-alexafluor conjugate and a streptavidin-quantum dot conjugate to the PAA chains of the cavitated micellar film. The success of this conjugation chemistry demonstrates the availability of the PAA domains to reagents in aqueous solution, and suggests the potential of the novel 2-D cavitated nanostructured system for biological applications. We have also demonstrated the plasticity of this rearrangement process by observing it with the spherical and cylindrical PS-*b*-P2VP copolymer micelles.

Chapter 4 BLOCK COPOLYMER MICELLES IN BIOCOMPATIBLE OILS AS NANOCONTAINERS FOR DRUG DELIVERY

4.1. Introduction

Selective solvents induce the self-assembly of block copolymers in solution into stable ordered structures. In medical applications, amphiphilic block copolymer micelles assembled in aqueous solutions with a hydrophilic corona block and hydrophobic core block have long been of interest as carriers for drug delivery.[27-30, 87-89] A variety of aqueous micelle systems that sequester poorly water-soluble drugs in the micelle core[27-30, 87-89] or which carry compounds that interact specifically with the core block (e.g., oligonucleotides bound to ionic micelles[90]) have been developed for systemic drug delivery and cancer therapy.

In a similar manner, micellar systems assembled in nonpolar solvents have been used as carriers of hydrophilic compounds. Metal salts sequestered into the hydrophilic cores of block copolymer micelles in organic solutions and cast as micellar thin films have been of particular interest for a variety of applications.[3-5, 7, 9-21, 53-55, 66, 91-93] Micelles have also been used as carriers of polar small molecule dyes in organic solutions. For example, Il Yoo et al.[94] loaded rhodamine derivatives in PS-*b*-P4VP inverse micelles in toluene and Groβ and Maskos[95] used crosslinked PS-*b*-P2VP nanoparticles in toluene to encapsulate low molecular weight dyes. Star polymer architectures and polyorganosiloxane nanoparticles have also been used for solubilizing low molecular weight dyes in organic phases.[96-98]

While most of these prior studies have focused on solvents relevant for industrial applications, we hypothesized that block copolymer micelles formed in biocompatible oil phases could be of interest in biomedical applications as carriers for therapeutic molecules, imaging agents, or vaccine adjuvants. Biocompatible oils are found in a variety of medical applications: Important vaccine adjuvants used widely in animal research (e.g. Freund's adjuvant) and in human patients (e.g. MF-59, a vaccine adjuvant in clinical use in the European Union) are based on oils (mineral oil and squalene in the case of Freund's adjuvant and MF-59[99, 100], respectively). Because of their interaction with lipid membranes, oils have been investigated for drug delivery applications such as transdermal[38-40] and oral delivery.[36] Other well-studied oils for biomedical applications include lipiodol, an iodinated fatty acid ethyl ester, used as a imaging contrast agent,[101] to target radiotherapy to hepatocellular carcinoma[102] and even for infertility.[103]

Although micelles formed by block or branched copolymers could be useful for controlling the loading and release of proteins or other hydrophilic drugs from oil phases relevant to many of the biomedical applications highlighted above, very few studies of micellar systems in biocompatible oil phases for drug delivery have been reported. In the arena of biotechnology, protein loading into surfactant-based inverse micelles has been used as a strategy for extraction/purification of proteins in a variety of organic solvents[104-113] including fatty acids and fatty acid esters.[112, 113] New and Kirby[114] investigated low molecular weight amphiphiles for loading of calcintonin in biocompatible oil phases for oral delivery. Recent work by Jones et al.[115] demonstrated the loading of a peptide, vasopressin, and two proteins, myoglobin and bovine serum albumin, into lipid modified poly(glycerol methacrylate) star polymers in ethyl oleate.

In this work we focused on micelles formed from a block copolymer system poly(ε-caprolactone)-*block*-poly(2-vinyl pyridine) (PCL-*b*-P2VP), containing a biodegradable hydrophobic block (PCL) and a polar, hydrogen bonding block (P2VP). We examined micelle assembly in two different oil phases, toluene (as a model volatile nonpolar solvent) and oleic acid, a naturally occurring fatty acid. Oleic acid is a biocompatible oil used in oral drug delivery,[31-36] buccal delivery,[37] transdermal drug delivery,[38-41] and as a vaccine adjuvant.[42] PCL-*b*-P2VP micelles in toluene were characterized by atomic force microscopy (AFM) and dynamic light scattering. The structure of the block copolymer in oleic acid was studied via cryogenic transmission electron microscopy (cryoTEM). Notably, we observed different micellar structures in the two solvents used here. In toluene, the micelles consist of P2VP cores with PCL corona, while in oleic acid our results suggest PCL blocks compose the micelle core with P2VP forming the corona. Two proteins, ovalbumin (ova) and bovine serum albumin (BSA), were loaded into the organic phase micelles. When the protein-loaded oleic acid phase is placed in contact with an aqueous reservoir, sustained release of protein back into aqueous solution is maintained over a period of ~30 hours. These results highlight the potential of block copolymers as carriers for sustained release of hydrophilic drug cargos from biocompatible oils.

4.2. Experimental Section

4.2.1. Materials

Poly(ε-caprolactone)-*block*-poly(2-vinyl pyridine) (PCL-*b*-P2VP) diblock copolymer [M_n (PCL) = 35 400 g/mol, M_n (P2VP) = 20 900 g/mol, copolymer PDI (M_w/M_n) = 1.8], PCL homopolymer [M_n = 33 000 g/mol, PDI = 1.7], P2VP homopolymer [M_n = 22 000 g/mol, PDI = 1.09] and their molecular characterization data were purchased from Polymer Source, Inc. Toluene and Gold(III) chloride trihydrate were obtained from Sigma-Aldrich. Phosphate buffered saline (PBS) was purchased from VWR International. Ovalbumin, texas red (ova-TR) conjugate, bovine serum albumin, texas red (BSA-TR) conjugate, NuPAGE LDS sample buffer, MES SDS running buffer, BenchMark pre-stained protein ladder and 10% Bis-Tris gels were obtained from Invitrogen. All aqueous solutions were made using deionized (DI) water (> 18 MΩ cm, Millipore Milli-Q). Oleic acid was obtained from EMD Chemicals and [methyl-C^{14}] methylated ovalbumin (ova-C^{14}) was purchased from American Radiolabeled Chemicals, Inc. Hionic-Fluor scintillation cocktail was obtained from Perkin-Elmer. All chemicals were used as received. Quantifoil R1.2/1.3 holey carbon-coated copper TEM grids were obtained from Ted Pella, Inc. Silicon nitride window TEM grids were obtained from Structure Probe, Inc.

4.2.2. Preparation of Polymer Solutions

Toluene or oleic acid was added to polymer powder to form a 10 g/L polymer solution. The solution was heated in a sealed vial at 70°C for 2 hours with periodic agitation to fully dissolve the polymer. Polymer solutions were then allowed to cool to room temperature for 16 hours. Toluene copolymer solutions were centrifuged for 30 sec at 14000*g* before use. Dilutions as needed were made from these stock solutions.

4.2.3. Atomic Force Microscopy (AFM)

Imaging was performed on a Digital Instruments Dimension 3000 Nanoscope IIIA scanning probe microscope using a silicon RTESP cantilever (tip radius < 10 nm) from Veeco Instruments operating in tapping mode. Micelle diameter and height were determined using linescan analysis of AFM images with NanoScope ® Software v5.30. To create samples for imaging, 50 μL of 0.01 g/L polymer solution in toluene were pipetted onto a silicon substrate and spin-cast at 2500 rpm for 60 sec with a ramp time of 1 sec. Samples were then dried under vacuum for at least 12 hrs at 25°C prior to imaging. For cavitation, micelle-coated substrates were placed in 20 mL of PBS for 16 hrs, rinsed briefly with DI water to help remove residual salt from the surface and dried under vacuum for at least 12 hrs at 25°C prior to AFM imaging.

4.2.4. Dynamic Light Scattering (DLS)

DLS experiments were performed using a Brookhaven BI-200SM light scattering system (514 nm argon laser) at a measurement angle of 90°. Samples were measured for 5 min with a polymer concentration of 0.1 g/L in toluene. Number average diameters are reported.

4.2.5. Cryogenic Transmission Electron Microcopy (cryoTEM)

CryoTEM was performed to characterize the morphology of the micelles in oleic acid. Oleic acid controls without polymer were also prepared. A thin film of oleic acid polymer solution was spin cast onto a silicon substrate at 4000 rpm with a 1 sec ramp time. A Quantifoil R1.2/1.3 holey carbon-coated copper grid was treated in an oxygen plasma for 30 seconds and then picked up using locking TEM tweezers and the tweezers were then mounted on the micromanipulator. The grid normal was aligned perpendicular to the lab bench, with a slight angle of 5-10 °. This angle allows only part of the grid to contact the oleic acid thin film upon lowering, helping to create a gradient of film thickness on the grid. The grid was lowered down into contact with the oleic acid thin film using the micromanipulator. Once the grid had first contacted the film, the grid was not lowered any further. After 5 seconds, the grid was raised away from the oleic acid thin film. At this point the grid should look 'wet' (darker in color) but there should not be a film whose thickness is easily visible to the eye. If there is an easily visible drop or film on the grid, the grid was blotted on a silicon wafer using the micromanipulator to remove extra oleic acid polymer solution. The grids were then transferred to a microscope slide and imaged in the optical microscope at 40X magnification to confirm that the holey carbon film had not been detached from the copper grid during sample preparation. The 1.2 um holes in the carbon film should be easily visible in the microscope. The oleic acid polymer solution results in a blurring of these holes in the microscope image compared to an empty grid. In this way, it is possible to tell where the oleic acid solution is on the grid. If the oleic acid film is too thick, individual 1.2 um grid holes will not be visible and TEM imaging will not be possible. The best samples corresponded to grids where inside of individual copper grid patterns, a transition from what appeared to be empty grid to oleic acid film was visible. It is believe that this indicates a gradient of oleic acid film thickness so that in the TEM, a range of oleic acid film thickness can be investigated. However, we did not attempt to correlate individual grid holes in the optical microscope with those imaged in the TEM.

The grid was then plunged into liquid nitrogen, vitrifying the solution. The grid was directly loaded into a JEOL 2200FS TEM using a Gatan 626 cryo-specimen holder at liquid nitrogen temperature, and imaged using 200kV accelerating voltage with a 185 μA emission current. TEM images were recorded at a magnification of 40,000X on a slow-scan CCD camera (Gatan, Inc.).

4.2.6. Loading of metal salt in PCL-*b*-P2VP Micelles in Toluene.

Gold (III) chloride trihydrate solid was added to a 10 mg/mL toluene solution of PCL-*b*-P2VP and mixed on a vortexer at 200 rpm for 16 hours. The micelle solution was then decanted from the remaining gold salt and centrifuged for 30 seconds at 14000*g*. Thin films were then cast onto silicon nitride TEM window grids at 2000 rpm with a 1 second ramp. TEM imaging was performed on a JOEL 200CX operating at 200 keV.

4.2.7. Loading of Proteins in PCL-*b*-P2VP Micelles

To load protein into PCL-*b*-P2VP, 50 μL of 10 g/L protein (ova-TR, BSA-TR, ova-C^{14}) was agitated on a vortexer at 200 rpm for 72 hrs with 1 mL of 10 g/L of polymer solution in oleic acid or toluene in a 1.5 mL microcentrifuge tube at 25°C. The mixture was then centrifuged to separate the oil and aqueous phases. Oleic acid solutions were centrifuged for 15 minutes at 14000*g*, while toluene solutions were centrifuged for 30 seconds at 14000*g*. Ova-C^{14} was diluted between 10:1 and 50:1 with non-labeled ova for loading experiments. Control experiments with no polymer, PCL homopolymer and P2VP homopolymer were also performed. Protein concentrations in each solution were determined using a Molecular Devices Spectramax M2^{e} fluorescence plate reader with an excitation and emission wavelength of 584 nm and 612 nm respectively. Ova-C^{14} concentrations were measured with a Packard Top Count NXT microplate scintillation counter using Hionic-Fluor scintillation cocktail.

4.2.8. Release of OVA-TR into PBS reservoirs

Protein release was investigated by gently layering 100 μL of oleic acid or toluene polymer solution loaded with ova-TR on top of 1 mL of PBS with 1% wt/v BSA in a 1.5 mL microcentrifuge tube and incubating the quiescent two-phase system at 37 °C or

25°C. At various times, aliquots of both phases were taken and their protein concentration determined. The oil phase was first removed before an aliquot of the aqueous phase was taken. Individual samples were used only for a single time point and each time point was assayed in quadruplicate. The solutions were not mixed during the release experiment. Samples were kept in the dark throughout the experiments.

4.2.9. SDS PAGE of ova-TR release from a Oleic Acid Copolymer Solution.

Ova-TR was released from oleic acid micelle into a PBS reservoir without BSA. Aliquots were taken after 24 hours and samples were prepared with NuPAGE LDS sample buffer under reducing conditions. 10% Bis-Tris gels with MES SDS running buffer were used at 100V for 70 minutes. Staining was performed using a SilverSNAP II stain kit according to the manufacturer's instructions.

4.2.10. 'Passive' Loading of Polymer Solutions

Prior to loading polymer solutions by mixing them and centrifuging to separate the two phases, we performed loading experiments where the oil phase (toluene or oleic acid) was gently layered on top of the aqueous solution containing the compound of interest. The two phases were not mixed, similar to the release experiments described above. Because of this lack of phase mixing, we term this 'passive' loading. We performed experiments with aqueous solutions of the small molecule dye calmagite, the polysaccaharide dextran and the protein ovalbumin. A rhodamine-dextran conjugate was used for quantification of loading and an ovalbumin-texas red conjugate was also used as above. Varying concentrations of the molecule of interest were used from 1-10 mg/mL while the polymer solution concentration was kept constant at 10 mg/mL. Loading was measured after 7 days.

4.2.11. Release from PCL-*b*-P2VP Micellar Films Cast from Toluene

Micellar films were cast by pipetting 100 µL of PCL-*b*-P2VP micelle solution in toluene that had been passively loaded with ova-TR, into an individual well of a white polypropylene 96 well plate. The solvent was allowed to evaporate for 4 hours in a fume hood before drying under vacuum for 1 hour at 25 °C. 150 µL of PBS solution was the added on top of the micellar films. The protein concentrations were determined using a Molecular Devices Spectramax M2^e fluorescence plate reader with an excitation and emission wavelength of 584 nm and 612 nm respectively. Individual samples were used only for a single time point and each time point was assayed in triplicate. Plates were sealed with an adhesive plastic film to prevent water lose over the experimental time course.

4.3. Results and Discussion

4.3.1. Characterization of PCL-*b*-P2VP Self-Assembly in Toluene

We first examined micelle formation of PCL-*b*-P2VP in toluene. Toluene is not itself a biocompatible organic phase, but rather serves as a model non-polar organic phase for analysis of PCL-*b*-P2VP micelle formation and enabled comparison of the properties of this block copolymer with a number of other micelle-forming copolymers that have been extensively characterized in toluene by our group and others. Self-assembly in toluene has been studied for a variety of block copolymers, most notably poly(styrene-*block*-X-vinylpyridine)[16, 116, 117] (PS-*b*-PXVP) (X = 2 or 4) and our own previous work with polystyrene-*block*-poly(acrylic acid)[21, 55, 118] (PS-*b*-PAA). Toluene is a selective solvent for the PS block and leads to inverse micelle formation for these amphiphilic block copolymers. Block copolymer micellar films can be cast onto substrates from volatile solvents, unlike low molecular weight surfactant micelles, due to the slower exchange kinetics of individual molecules with micelles in solution.[2] The micelle morphology is kinetically trapped in the final thin film upon solvent evaporation, even in cases for which the copolymer composition would suggest a transition to a different equilibrium heterogeneous phase. Recently, Chan et al.[119] demonstrated the formation of PCL-*b*-P4VP spherical micelles with a PCL corona and P4VP core in a 90/10 v/v solvent mixture of toluene and dichloromethane (DCM). The polymer was first dissolved in DCM, a good solvent for both blocks, and then toluene (a poor solvent for P4VP) was added to induce the formation of ordered structures in solution with a PCL corona.

Here we also used toluene as a preferential solvent for PCL to create ordered structures of a similar polymer, PCL-*b*-P2VP. All of the studies carried out here used a block copolymer with molecular weights of 35.4 kg/mol for the PCL block and 20.9 kg/mol for the P2VP block. AFM images of PCL-*b*-P2VP micelles spin-cast from toluene onto silicon substrates were collected and dynamic light scattering was performed to measure the hydrodynamic diameter. Figure 4-1A and Figure 4-1B show an AFM height and corresponding phase image of PCL-*b*-P2VP micelles cast from toluene. By spin-casting at high speed from dilute (0.01 g/L) solutions we were able to create films where individual micelles were easily visible with separation distances between adjacent micelles of several hundred nanometers. Linescans through individual micelles (e.g. Figure 4-1C) were analyzed to determine the distribution of micelle heights and diameters (Table 4-1). The block copolymer had a PDI of 1.8 and we also observed significant polydispersity in the size of the micelle assemblies. With an average diameter of 103 ± 32 nm and average height of 5.6 ± 2.4 nm, the micelles in the images are spherical structures that have flattened out on the surface upon casting/drying. When imaging spherical particles, AFM image analysis overestimates the particle diameter but provides accurate height data because of tip geometry.[120, 121] However, because the micelles are flattened (5.6 nm height vs 103 nm diameter) and have a height of only about one half of the AFM tip radius, the error in estimated diameter due to tip size is negligible.

In prior studies we demonstrated the ability to induce rearrangement ('cavitation') of substrate-supported polystyrene-*block*-poly(acrylic acid) (PS-*b*-PAA) inverse spherical micelles upon treatment with aqueous solutions.[21] Briefly, when inverse micelles are treated with a selective solvent for the core polymer block, such as aqueous solutions, the hydrophilic micelle core swells and fractures the glassy PS corona. We subsequently studied this process in more detail[118] and others have reported similar behavior for polystyrene-*block*-poly(2-vinyl pyridine) (PS-*b*-P2VP) micelles.[67, 68] We have also observed this rearrangement in PS-*b*-P2VP.[122] In the present studies, instead of a glassy amorphous corona block like PS, the micelle coronas are composed of a rubbery semicrystalline PCL block (T_g = -60°C, T_m = 60°C). We observed a similar cavitation process for PCL-*b*-P2VP micelles cast onto silicon and exposed to PBS for 16 hrs. Figure 4-1D and Figure 4-1E are AFM height and phase images showing the polymer rearrangement upon treatment in PBS buffer which selectively swells the P2VP core block. The rearrangement is difficult to observe in the height image due to the relatively small cavity depth compared to the overall micelle height. However, micelle reorganization is clearly observed in the phase image (Figure 4-1E) and micelle height cross section (Figure 4-1). The cavity width and depth is underestimated by the AFM due to the similar dimension of the cavity with the AFM tip. Cavitation of the micelles on exposure to aqueous solutions is consistent with P2VP forming the core of the micelle structures. In addition, similar to work done previously in our own lab[21, 53-55, 66, 91-93] and others,[3-5, 7, 9-20] we exploited the interaction of vinylpyridine groups with metal salts to successfully load gold salts into the core of the PCL-*b*-P2VP micelles as confirmed by TEM imaging (Figure 4-2). These data collectively support the conclusion that P2VP forms the core of PCL-*b*-P2VP micelles assembled in toluene.

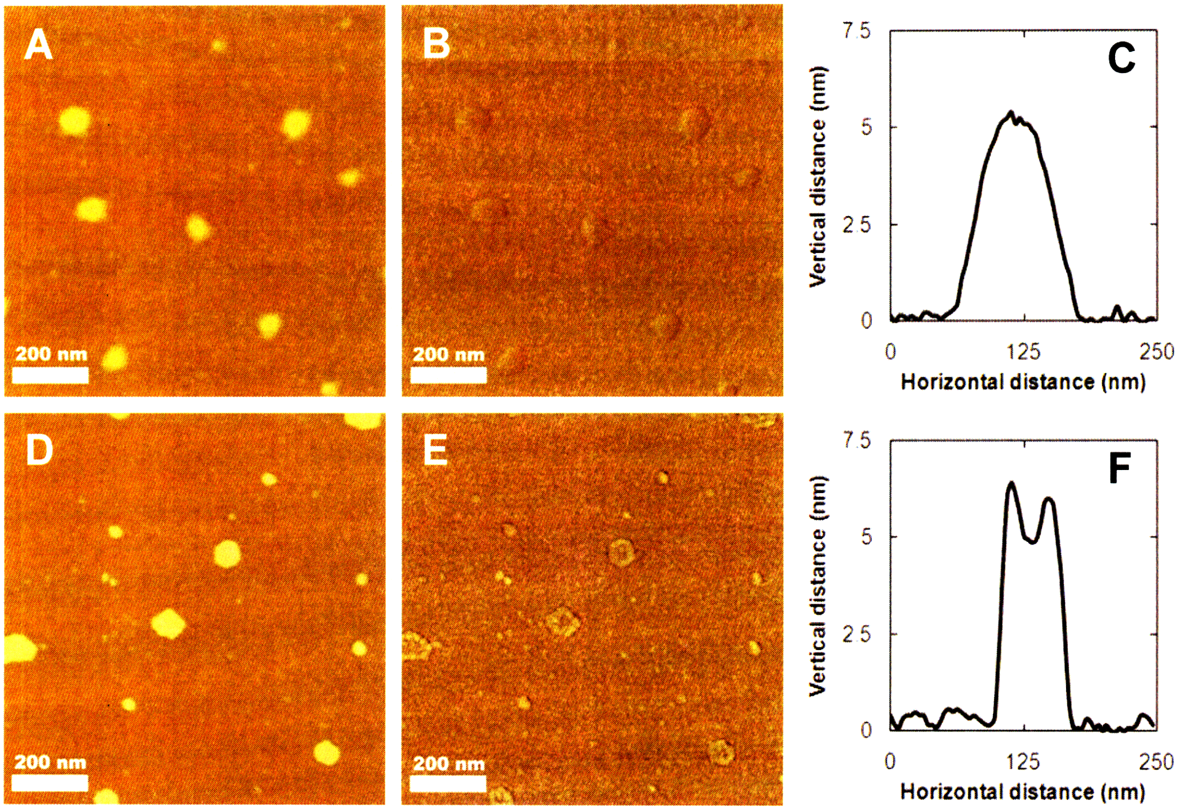

Figure 4-1: PCL-*b*-P2VP micelles cast from toluene on silicon. (A) AFM height image and (B) corresponding phase image of as-cast micelles. (C) Height cross-section of as-cast individual micelle. (D) Height image and (E) corresponding phase image of micelles after treatment in PBS for 16 hours. (F) Height cross-section showing cavitated morphology of micelles after PBS treatment. Height scales are 20 nm and phase scales are 50 °.

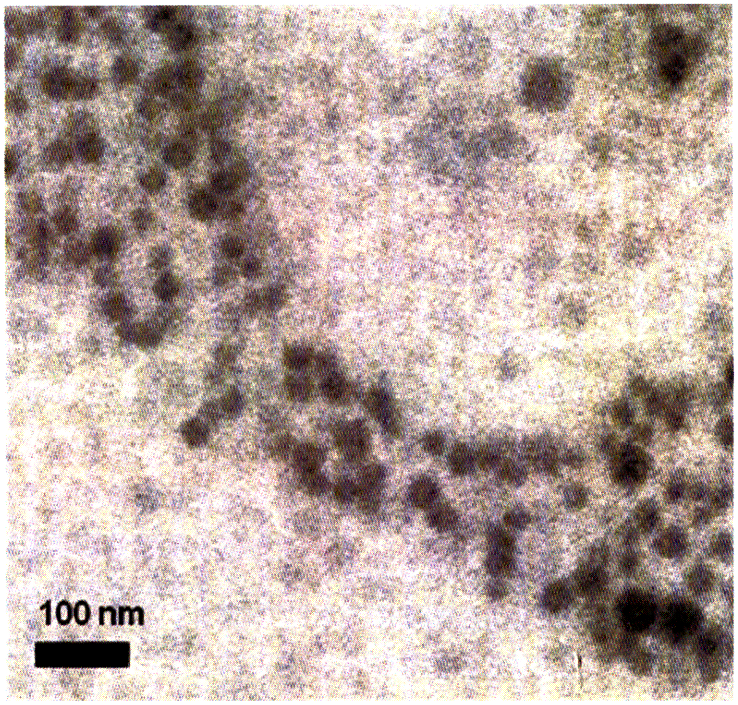

Figure 4-2: TEM image of PCL-*b*-P2VP micelle loaded with $HAuCL_4$ in toluene and spin cast on a silicon nitride window TEM grid. Dark circular regions represents the gold salt associated with the P2VP core domains.

The PCL-*b*-P2VP micelles had a number average hydrodynamic diameter of 154 nm as determined by DLS (Table 4-1). We can compare and correlate this result to our AFM imaging. First, from our AFM image analysis we can calculate our average particle volume by approximating the particles as spherical caps.

Equation 4-1:
$$V_{micelle} = \pi h(3D^2+4h^2)/24$$

Where h and D are the height and diameter of the micelles measured by AFM.

The volume of P2VP block can then be calculated, assuming equal densities for PCL and P2VP, by simply multiplying the total micelle volume by the weight fraction of P2VP. Certain molecular-level length scales can then be calculated readily to provide internal checks on the micellar size and proposed molecular organization. Having calculated the P2VP volume, we can compute the diameter of the P2VP core for the polymer in solution assuming a spherical geometry and no solvation. The corona thickness, δ, can be determined by subtracting the core radius from the overall micelles radius determined by light scattering. Knowing the corona thickness, we can compare the conformation of the corona chains to that of a fully extended chain and to the expected end-to-end distance for a PCL chain. The fully extended chain length ($nl\cos\theta$) for PCL is 269 nm for M_n = 35 400. The expected root mean square (RMS) end-to-end distance for PCL chains is obtained using the characteristic ratio (C_∞) and an estimated expansion factor (α) in toluene:

$$\textbf{Equation 4-2:} \qquad \langle r^2 \rangle^{1/2} = (\alpha^2 C_\infty n l^2)^{1/2}$$

The theta temperature for PCL in toluene[123] is 15 °C, so we expect α to be greater than, but close to unity. The characteristic ratio of PCL[124, 125] is ~6. We used a number weighted average value of the C-O and O-O bond lengths for l to obtain a value for $\langle r^2 \rangle^{1/2}$ of 17.2 nm.

The fractional chain extension of polymer blocks making up the micelle corona depends on a variety of factors including the composition ratio of the core and corona blocks, size of the micelle core, micelle aggregation number, length of the corona chains as well as the chemical nature of the corona chains and solvent quality.[126, 127] Fractional chain extensions have been observed ranging from 20 to 100%.[126-134] Here, the PCL corona chains are 24% of the fully extended chain length (Table 4-1). The PCL chains in our micelles are long (310 repeat units with 7 bonds per repeat unit along the backbone) compared to the average micelle corona chain lengths. Because the PCL chains are long compared to the P2VP chains, the micelles are 'hairy' micelles, as opposed to 'crew-cut' micelles and the former are generally characterized by lower corona chain extensions.[126,

[127] Charged polymer chains result in more extended conformation because of electrostatic repulsion of like charges on adjacent chains. PCL is uncharged so we expect lower chain extension as observed. Our results agree well with a similar long chain, uncharged micelle system of PS-*b*-PI in decane studied by McConnell et al.[129] who observed corona chains that were 21%-35% of the fully extended chain length (calculations done by Zhang et al.[126])

The calculated corona thickness is four times the expected RMS end-to-end distance. Steric effects near the core/corona interface cause the chain to take on a more extended conformation compared to the expected end-to-end distance. This has been observed by others[126-134] including Schillen et al.[131] who observed chain lengths longer than the RMS end-to-end distance (calculated assuming $\alpha = 1$) for PI-*b*-PMMA in acetonitrile even at 20 °C below the theta temperature, which should promote compact corona chains ($\alpha < 1$). These results are summarized in Table 4-1 and provide good support for a P2VP core/PCL corona micelle structure in toluene with a diameter of ~150 nm.

Micelle Solution	Hydrodynamic Diameter (D_H)	Diameter (Dry state AFM)	Height (Dry state AFM)	Core Diameter	Corona Thickness (δ)	$\delta / n\,l \cos\theta$	$\delta / (\alpha^2 C_\infty n\,l^2)^{1/2}$
	(nm)	(nm) (± SD)	(nm) (± SD)	(nm)	(nm)		
As-assembled	154	103 ± 32	5.6 ± 2.4	28	63	0.24	3.7
OVA-TR Loaded	157	104 ± 27	5.8 ± 1.7	28	65	0.24	3.8

Table 4-1: Micelle size determination and analysis by DLS and AFM for as-assembled micelle and ova-TR loaded micelles in toluene. Hydrodynamic radius (D_H) measured by DLS. Diameter and height from AFM image analysis. Core diameter, corona thickness, ratio of corona thickness (δ) to fully extended chain length and RMS end-to-end distance calculated as discussed in the text.

4.3.2. Characterization of Polymer Self-Assembly in Oleic Acid

For drug delivery applications, we assessed PCL-*b*-P2VP solution behavior in oleic acid, a biocompatible natural fatty acid with very different physical properties compared to toluene. Though oleic acid is comprised of a long nonpolar alkyl chain, the acid endgroup of oleic acid enables hydrogen bonding between oleic acid molecules and between oleic acid and dissolved solutes. Oleic acid is a high viscosity, high boiling point liquid which precludes AFM imaging of dried substrate-supported micelles, as seen above in toluene, because the solvent evaporation rate is too low. In order to visualize the polymer assembly in solution we turned to cryogenic transmission electron microscopy (CryoTEM). CryoTEM is a technique that relies upon solvent vitrification to trap molecular and morphological conformations and allow direct imaging of the *in situ* state of structures in liquids. This technique has been widely applied to aqueous systems, but has found more limited application for continuous oil phases, as recently reviewed.[135] Difficulties in sample preparation include problems in applying a thin film to a TEM grid, particularly for high viscosity solvents, finding a suitable cryogen that is not soluble in the oil phase and imaging vitrified solvents that are often more susceptible to electron beam damage and provide lower contrast compared to aqueous solutions.[135, 136]

Here we were able to overcome these difficulties to image PCL-*b*-P2VP in oleic acid. Figure 4-3A shows a representative cyroTEM image of the spherical structures formed by the copolymer in oleic acid. We analyzed an extensive series of cryoEM images in order to obtain an average particle size and size distribution presented in Figure 2B, with arrows indicating the average micelle size. The average micelle size is 144 nm with a standard deviation of 59 nm for 262 particles imaged (Table 4-2). The particle size is similar to that observed for micelles in toluene and, again, we see significant polydispersity. However, unlike toluene, homopolymer solubility data suggest micelles assemble with a PCL core and a P2VP corona: P2VP homopolymer is soluble in oleic acid at 25°C while PCL homopolymer is only soluble above 60°C and precipitates upon cooling. Both homopolymers tested had a similar M_n to their respective blocks in the copolymer. P2VP hompolymer solubility might be attributed the strong hydrogen bonding character of the nitrogen heteroatom.[137]

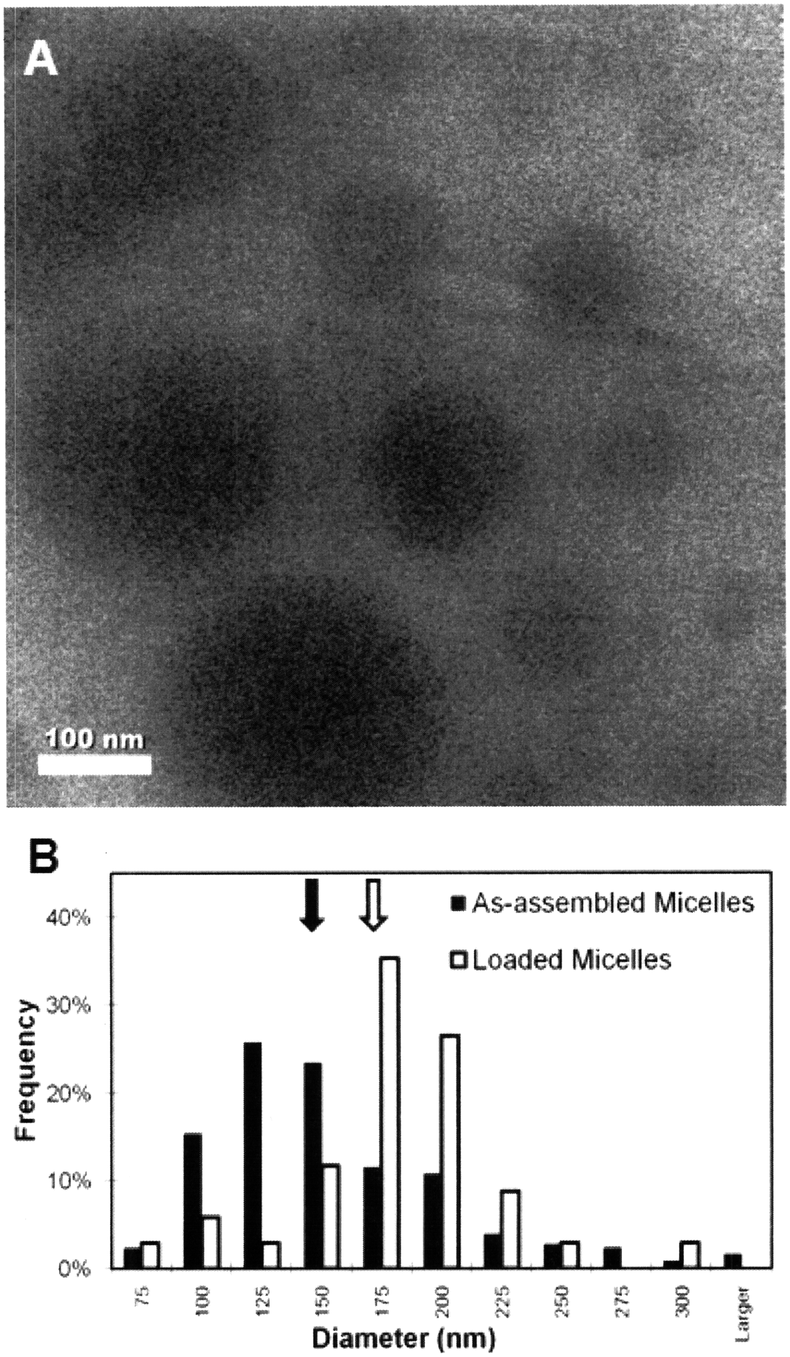

Figure 4-3: (A) Cryogenic transmission electron microscopy of PCL-*b*-P2VP inverse micelles in oleic acid. (B) Histogram of particle size distribution for as-assembled and ova-TR loaded micelles. Black and white arrows indicates average micelle size for as-assembled and ova-TR loaded micelles respectively.

Micelle Solution	Diameter	Number of Particles Sampled
	(nm) (± SD)	
As-assembled	**144 ± 59**	**262**
OVA-TR Loaded	**166 ± 44**	**34**

Table 4-2: Micelle size and distribution as determined from cryoTEM image analysis.

4.3.3. Loading of Ovalbumin and Bovine Serum Albumin in Micelles

To determine whether PCL-*b*-P2VP micelles could load proteins into organic phases, we chose ovalbumin (ova) (45 kDa, pI = 4.5) and bovine serum albumin (BSA) (67 kDa, pI = 4.8) as model globular proteins cargos. We quantified protein loading into micelle-containing toluene or oleic acid using fluorescently labeled conjugates of ova (ova-TR) and BSA (BSA-TR) as well as a radiolabeled ova (ova-C^{14}) conjugate. Micelles were loaded by mixing 1 mL of 10 g/L micelle solution in toluene or oleic acid with 50 uL of 10 g/L protein solution in PBS. Solutions were centrifuged to separate the aqueous and oil phases after 72 hours.

In toluene, loadings of 5.7 % wt/wt (weight of protein / weight of P2VP) were achieved for ova and 3.0% wt/wt for the higher MW BSA in block copolymer solutions (Table 4-3). Experiments with P2VP homopolymer, PCL homopolymer and pure toluene revealed negligible loading of protein into the toluene phase. These results demonstrate the importance of the block copolymer micelle structure for the solubilization of protein for the case of toluene, a highly nonpolar solvent, as the organic phase.

For block copolymer solutions in oleic acid, loadings of 7.8% wt/wt (weight of protein / weight of P2VP) and 1.9% wt/wt were achieved for ova and BSA, respectively (Table 4-3). An ova-TR loading of 7.8% wt/wt corresponds to transfer of 58% of the ova-TR originally in the aqueous phase into the oleic acid phase by the block copolymer. This degree of protein loading into PCL-*b*-P2VP micelles appeared to be saturating, as experiments using 100 uL of 10 g/L protein solution in PBS did not result in higher amounts of protein being retained in the oil phase. Loading of ovalbumin with fluorescent or radioactive labels showed similar results. As described above, PCL homopolymer is insoluble in oleic acid at room temperature, precipitating upon cooling from 70°C. Oleic acid from which PCL homopolymer had precipitated and pure oleic acid were unable to solubilize ova or BSA. However, P2VP homopolymer solutions in oleic acid incorporated 1.9 % (wt/wt P2VP) ova-TR or 0.70% (wt/wt P2VP) BSA-TR. These results suggest that interactions between oleic acid, P2VP and the protein support solubilization of ova in the oleic acid phase. Surfactants,[138] including oleic acid[139] and sodium oleate,[140, 141] have previously been shown to interact with proteins through a process known as hydrophobic ion pairing[142-144] that can increase protein solubility in an organic phase. This provides a possible mechanism for interaction between ova and oleic acid. But here we observed insignificant loading in pure oleic acid, demonstrating the importance of P2VP.

Because PCL-*b*-P2VP micelles in oleic acid consist of a P2VP corona and PCL core, the observed P2VP homopolymer loading and PCL insolubility suggest that it is the corona of the block copolymer micelles that is sequestering protein in the oleic acid/block copolymer system. The PCL core is insoluble in both oleic acid and water at room temperature, implying that no significant protein loading can be accommodated. To the best of our knowledge, this is the first demonstration that in continuous oil phases, drug (or protein) cargo loading can occur in the *corona* of block copolymer micelles, as opposed to the more common situation of solute loading in the core of micelles. These results with PCL-*b*-P2VP demonstrates the ability of block copolymers to solubilize protein into either the core or corona of micelles assembled in organic phases, depending on the balance of interactions between blocks, solvent, and protein.

Solvent	Polymer	ova-TR	ova-C14	BSA-TR
		(%wt/wt) (±SD)	(%w/wt) (±SD)	(%w/wt) (±SD)
Oleic Acid	PCL-*b*-P2VP	7.8 ± 0.79	6.5 ± 2.5	1.9 ± 0.68
Oleic Acid	PCL	insoluble	n.d.	insoluble
Oleic Acid	P2VP	1.9 ± 0.22	n.d.	0.70 ± 0.041
Oleic Acid	no polymer	0.048 ± 0.0052	0.16 ± 0.19	0.039 ± 0.004
Toluene	PCL-*b*-P2VP	5.7 ± 1.8	n.d.	3.0 ± 0.32
Toluene	PCL	< 0.01	n.d.	< 0.01
Toluene	P2VP	< 0.01	n.d.	< 0.01
Toluene	no polymer	< 0.01	n.d.	< 0.01

Table 4-3: Loading of ovalbumin (ova) or bovine serum albumin (BSA) into polymer solutions in toluene or oleic acid. Loading experiments used 10 mg/mL polymer solutions. Protein loadings are in % wt/wt of P2VP for PCL-*b*-P2VP and P2VP homopolymer, % wt/wt PCL for PCL homopolymer, and % wt/wt polymer if a 10 mg/mL polymer solution had been used for the no polymer control experiments. n.d. = not determined.

4.3.4. Characterization of Micelles Loaded with Ovalbumin in Toluene and Oleic Acid

In order to determine if loading of protein had any effect on the micelle morphology, we characterized the structure of PCL-*b*-P2VP micelles in both toluene and oleic acid after loading of ova-TR. AFM imaging of micelles loaded with ova-TR (Figure 4-4A) cast from toluene onto silicon showed the same spherical morphology (compare to Figure 4-1A), and image analysis led to almost identical average dimensions and size distributions (Table 4-1). In line with the AFM results, DLS experiments gave a hydrodynamic radius of 157 nm for the protein loaded micelles compared to 154 nm for the as-assembled micelles. Each of the characterization techniques indicates that the loading of protein did not have a significant influence on the morphology, size and size distribution of PCL-*b*-P2VP micelles in toluene. This is consistent with the relatively low weight fraction of protein sequestered within each micelle core.

CryoTEM of ova-loaded micelles in oleic acid showed that the spherical morphology of PCL-*b*-P2VP micelles was unchanged by protein loading, and analysis resulted in a similar average size and size distribution (Figure 4-4B, size histograms overlaid in Figure 4-3B): The average protein-loaded micelle size is 166 ± 44 for 34 particles imaged. The increase in average micelle size of 22 nm is relatively small compared to the distribution of sizes and may be a result of the small number of loaded micelles that were able to be imaged, or may reflect a small increase in micelle dimensions following protein loading.

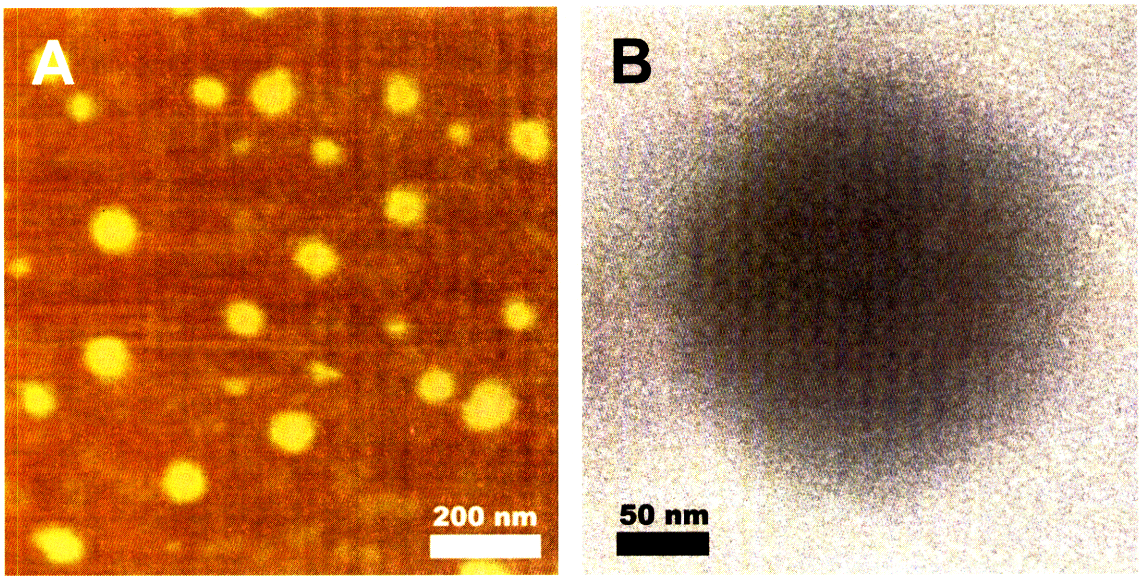

Figure 4-4: (A) AFM height image of PCL-*b*-P2VP micelles loaded with ova-TR cast from toluene on silicon. (B) Cryogenic transmission electron microscopy image of PCL-*b*-P2VP micelles loaded with ova-TR in oleic acid.

Summarizing these observations, we propose the following mechanism for micelle loading of protein in our experiments (Figure 4-5): in solution single block copolymer chains, or unimers, exchange with the micelle assemblies.[2] The P2VP block of the unimer in solution complexes protein which is then shuttled into a micelle assembly, thereby loading the protein into the micellar structure. This unimer shuttling process sequesters protein molecules into the micelle regardless of the location of the P2VP block, i.e. in the micelle core or corona. When a copolymer molecule leaves the micelle, the protein remains behind, cooperatively associating itself favorably with the P2VP blocks in the micellar structure. The block copolymer is able to load significantly more ova per unit weight of P2VP compared to P2VP homopolymer, showing the importance of the micelle structure to act as a protein depot.

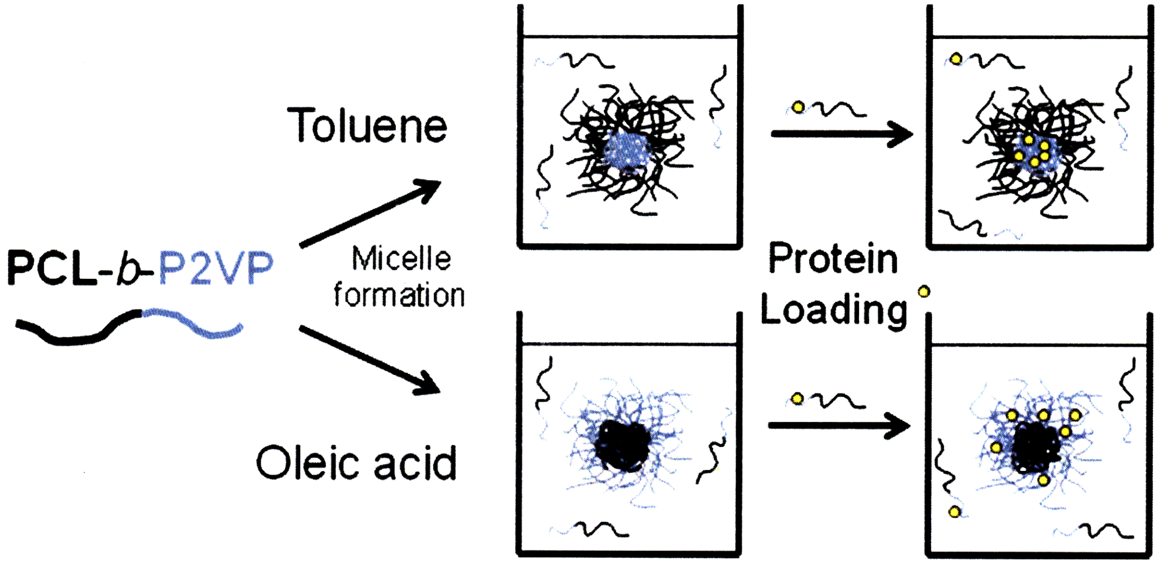

Figure 4-5: Schematic models for PCl-b-P2VP micelle structure and protein loading in toluene and oleic acid.

4.3.5. Release of Ovalbumin from Inverse Micelles

We hypothesized that micelles in biocompatible oils could serve as depots for sustained release of proteins or other drug compounds from oil phases into extracellular fluids in various applications such as topical or oral drug delivery. To investigate the release of protein from micelles we measured the exchange of protein between an oleic acid block copolymer solution loaded with ova-TR and an aqueous reservoir of PBS with 1% BSA. Oleic acid (100 μL) containing 10 g/L PCL-*b*-P2VP loaded with ova-TR (29 ug ova total) was gently layered over 1 mL of an aqueous reservoir (PBS with 1% BSA) in a 1.5 mL microcentrifuge tube, and protein transfer into the aqueous phase during static incubation at 37°C was recorded over time via fluorescence measurements. The release profile of ova-TR from the inverse micelle in oleic acid is shown in Figure 4-6.

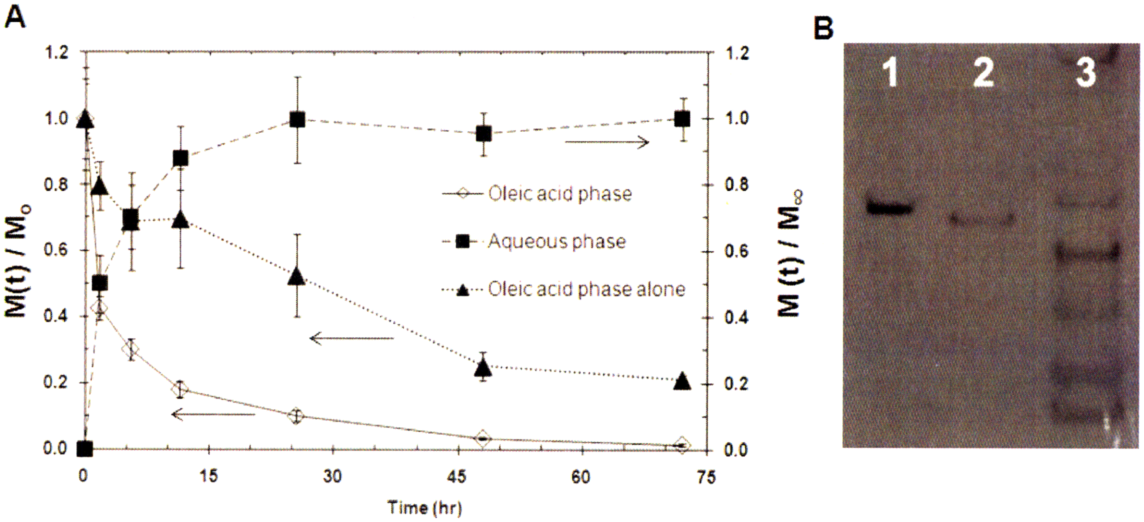

Figure 4-6: Release of ova-TR from oleic acid polymer micelle solution into PBS with 1% BSA reservoir upon static incubation in a microcentrifuge tube measured by fluorescence. Error bars represent the standard deviation of 4 independent fluorescence measurements. 'Oleic acid phase' and 'Aqueous phase' denote the loaded polymer micelle solution and aqueous reservoir solution in contact with each other. 'Oleic acid phase alone' denotes an ova-loaded copolymer micelle solution in oleic acid that was incubated in a microcentrifuge tube without addition of an aqueous reservoir. M(t) is the mass of ova-TR in the indicated phase, M_0 is the initial mass of ova-TR in the oleic acid

phase and M_∞ is the mass of ova-TR in the aqueous phase after 72 hours. (B) SDS PAGE of ova-TR release from oleic acid block copolymer solution into PBS reservoir (no BSA present in reservoir). Lanes: (1) Ova-TR released from block copolymer oleic solution; (2) Ova-TR stock solution; (3) Protein Ladder. The band just above the location of Ova-TR in lanes 1 and 2 represents ~49 kDa standard and the band just below represents ~37 kDa standard.

Release of ova-TR from the micelle phase was essentially complete after ~30 hrs, with the aqueous phase reaching 90% of maximum release by this time. The amount of ova-TR in the oleic acid phase dropped to 2% of initial loading by the 72 hr time point, however, the amount of ova-TR released in to the aqueous phase aqueous phase at the 72 hr time point (M_∞) was only 30% of the initial loading (M_0). A series of control experiments clarified the source of this protein loss. Ova-TR standard solutions in PBS with 1% BSA were completely stable over this time course (data not shown). However, ova-TR-loaded micelles in oleic acid incubated in the absence of an aqueous phase ('Oleic acid phase alone,' Figure 4-6) showed a loss of ova-TR over time, with only 21% of the originally loaded protein remaining at the 72 hr time point. Two potential mechanisms for protein loss from the oleic acid phase are (i) protein adsorption to the walls of the centrifuge tube in the oil phase, or (ii) protein aggregation at the oleic acid-water interface. To distinguish between these possibilities, experiments measuring release of ova-TR from different volumes of oleic acid/micelle solutions into fixed volumes of aqueous phase in the same microcentrifuge tubes were performed. In this setup, the oil phase/tube wall interfacial area was steadily increased while the oil/aqueous reservoir interfacial area was held constant. We observed that the amount of ova-TR signal loss scaled linearly with the amount of oleic acid micelle solution volume (data not shown). This suggests that protein lost from the organic phase was an artifact of adsorption to the sides of the microcentrifuge tubes in the oil phase, rather than protein aggregation at the oleic acid-water interface – an important distinction since the former mode of protein loss would not be active in many real applications (e.g. topical delivery). We also confirmed the transfer of protein into aqueous phase reservoirs lacking BSA by SDS PAGE analysis (Figure 4-6B). Importantly, ova-TR release from the block copolymer oil phase showed no signs of aggregation/oligomerization, but migrated at a slightly higher molecular weight compared to the ova-TR standard solution, which may reflect some residual association of oleic acid molecules with release protein. The kinetics of ova-TR release from P2VP homopolymer in oleic acid (Figure 4-8) were similar to block copolymer solutions, suggesting a similar release mechanism from PCL-*b*-P2VP and P2VP homopolymer solutions. The key advantage of the block copolymer structure compared to homopolymer P2VP is thus the increased loading of protein into the organic phase achieved per mass of P2VP.

In order to compare to our oleic acid release data, we measured the release of ova-TR from PCL-*b*-P2VP micelles in toluene. The same experimental setup and geometry as above was used, but due to the volatile nature of toluene, we ran experiments at 25°C to limit the effect of toluene evaporation on the results. Ova-TR release was complete after ~100 hours, slower than the release kinetics observed for micelles in oleic acid at 37 °C. These kinetics are similar to what we observed for release of ova-TR from micelles in oleic acid at 25°C (data not shown). However, unlike oleic acid, the amount of ova-TR released into the aqueous phase (M_∞) is 97% of the initial loading (M_0).

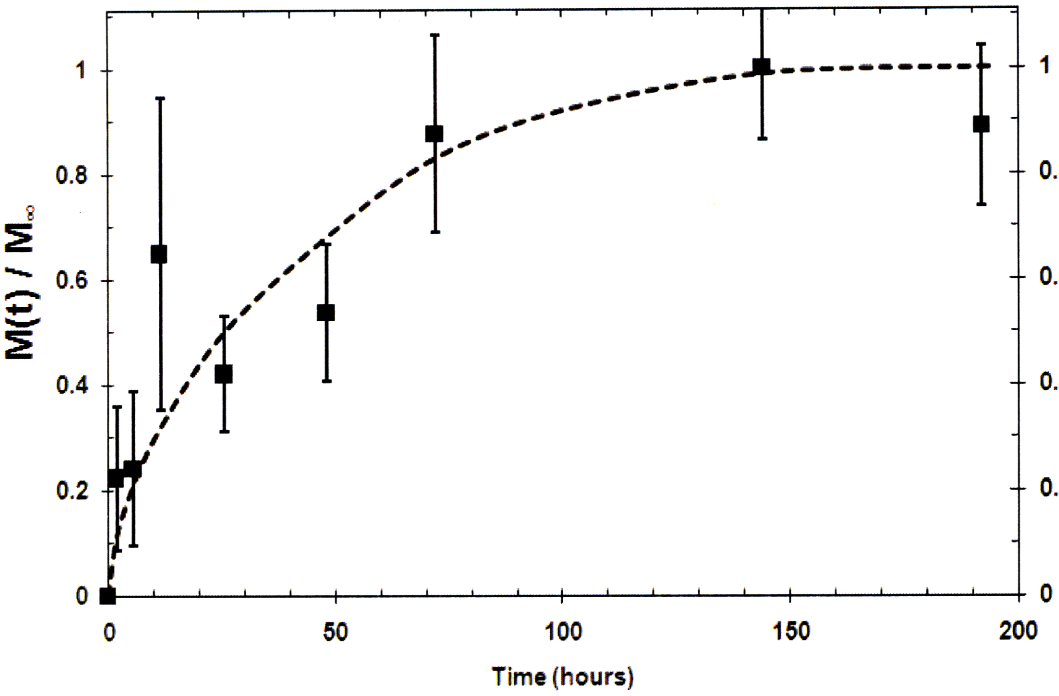

Figure 4-7: Release of ova-TR from PCL-*b*-P2VP micelles in toluene into an aqueous reservoir of PBS with 1% wt/v BSA during static incubation in an microcentrifuge tube. Data points represent the amount of ova-TR in the aqeuous reservoir. Error bars represent standard deviation of three independent experiments. The dotted line is a quide to the eye.

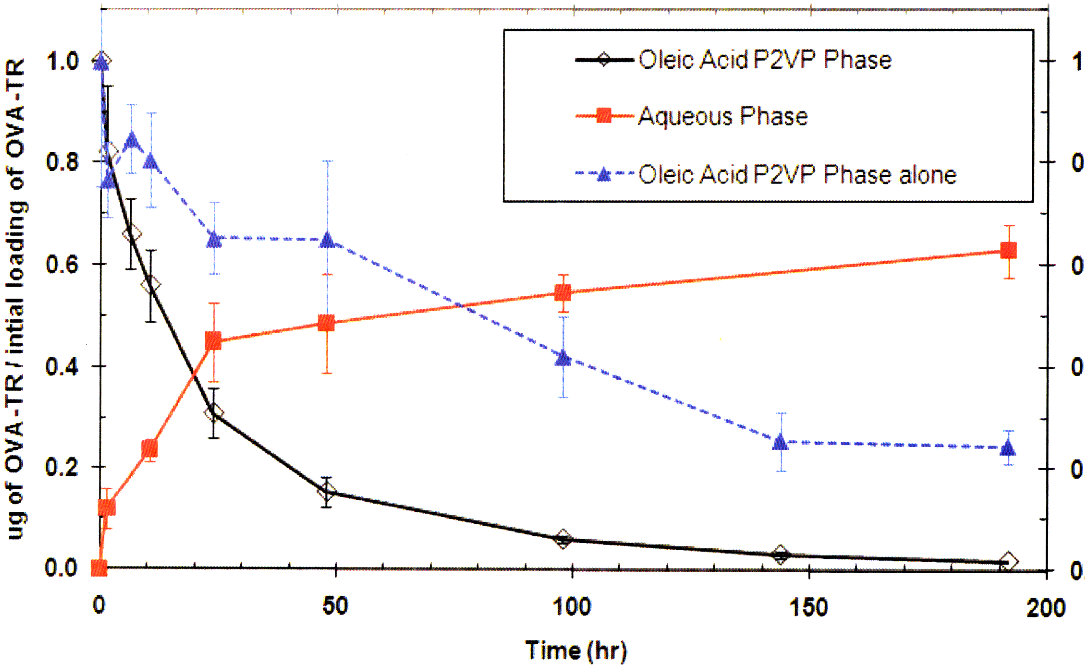

Figure 4-8: Release of ova-TR from oleic acid P2VP homopolymer solution into PBS with 1% BSA reservoir measured by fluorescence at 25°C Error bars represent the standard deviation of 4 independent fluorescence measurements. 'Oleic acid P2VP phase' and 'Aqueous phase' denote the loaded homopolymer solution and aqueous reservoir solution, respectively. 'Oleic acid P2VP phase alone' denotes a homopolymer solution in oleic acid loaded with ova-TR that was incubated in a microcentrifuge tube without addition of an aqueous reservoir.

4.3.6. Passive Loading of Calmagite and Dextran into PS-*b*-PAA and PS-*b*-P2VP micelles in Toluene

The small molecule calmagite (Figure 4-9B) and the polysaccharide dextran (Figure 4-11A) have been successfully loaded into spherical inverse micelles of PS-*b*-PAA 42.5k-*b*-4.5k and PS-*b*-P2VP 81k-*b*-21k in toluene. Loading was accomplished by gently layering the block copolymer solution in toluene on top of an aqueous phase containing either calmagite of dextran (Figure 4-9A). No mixing of the two phases occurred.

Calmagite was solubilized in the toluene phase in the presence of both PS-*b*-PAA and PS-*b*-P2VP copolymer, but no transfer occurred in the pure toluene (Figure 4-9C). Experiments with PS, PAA and P2VP hompolymer were not performed. Although loading was not quantified, the PS-*b*-P2VP toluene solution has a darker color compared to the PS-*b*-PAA solution, indicating a higher loading of calmagite. This is most likely due to the larger weight fraction of block polymer that is the core forming block (P2VP or PAA). Calmagite is also contains a SO_3H group that could become negatively charged in solution and potentially have stronger interactions with the P2VP block compared to the PAA block. However, Groβ and Maskos[95] have shown that charge interactions plays a minimal role in loading of small molecule dyes into crosslinked PS-P2VP nanoparticles in toluene.

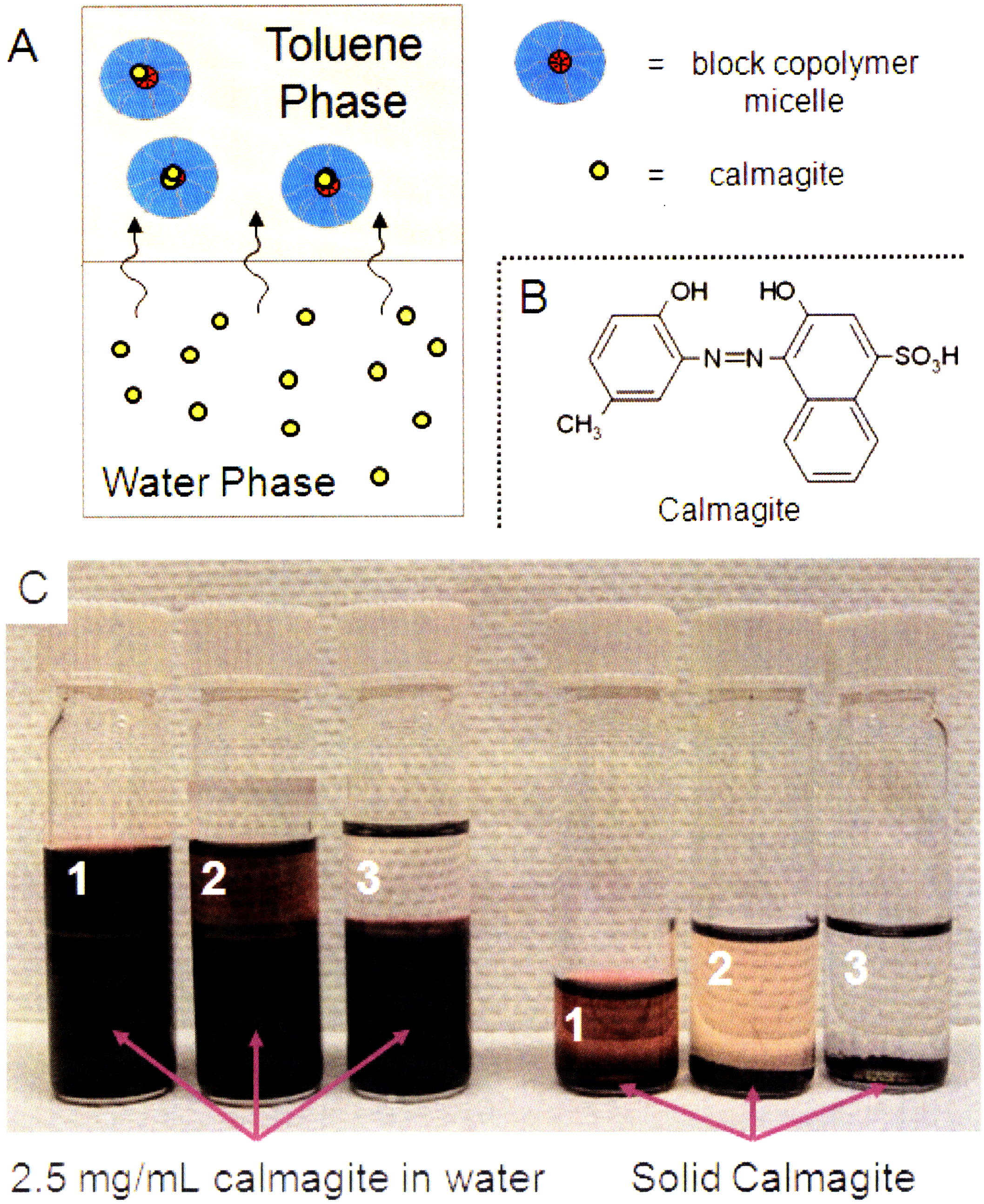

Figure 4-9: (A) Schematic of 'passive' loading experements. (B) Molecular structure of calmagite. (C) Transfer of calmagite from aqueous solutions of calmagite and solid calmgate powder into (1) 10 mg/mL PS-*b*-P2VP 81k-*b*-21k in toluene, (2) 10 mg/mL PS-*b*-PAA 42.5k-*b*-4.5k and (3) pure toluene.

We analyzed PS-*b*-PAA and PS-*b*-P2VP micellar thin films cast after loading with calmagite. AFM imaging showed that the block copolymer maintained its spherical micelle structure and fluorescence microscopy confirmed the presence of calmagite (Figure 4-10). Similar results were obtained for PS-*b*-PAA (data not shown).

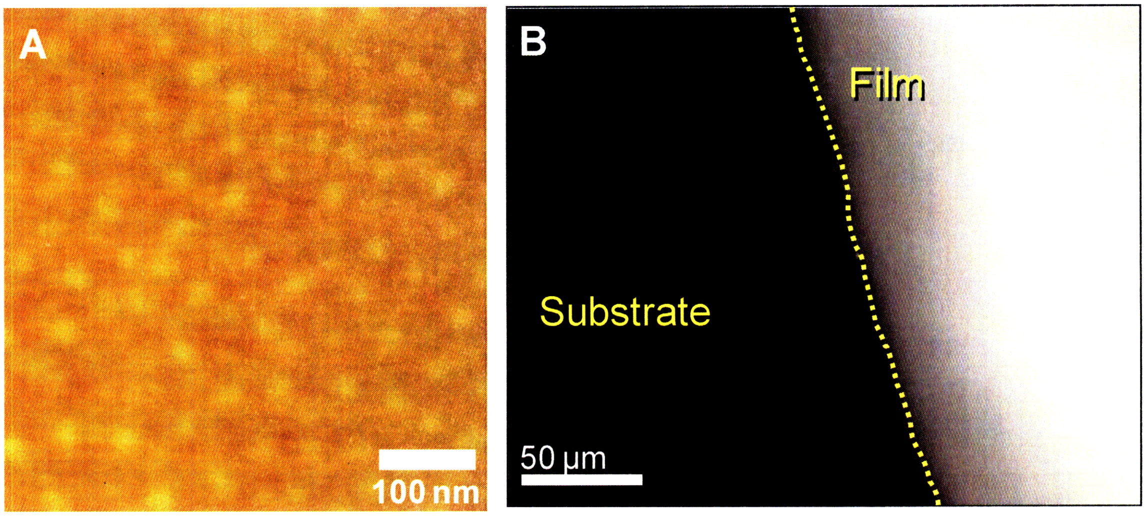

Figure 4-10: (A) AFM height image and (B) fluorescence optical microscope image of PS-*b*-P2VP 81k-*b*-21k micellar thin film cast from toluene after loading with calmagite. AFM height scale is 20 nm.

Analog experiments to those done with calmagite were done using 10 mg/mL aqueous solutions of the polysaccharide, dextran, for PS-*b*-PAA and PS-*b*-P2VP micelles in toluene. Fluorescene microscopy confirmed the presence of dextran in micellar thin films and AFM imaging revealed that the spherical morphology of the block copolymer was unchanged after dextran loading (Figure 4-11). The inconsistent intensity in the fluorescence image is due to variation of film thickness that is commonly observed at the edge of spin-cast films. Similar data was obtained for PS-*b*-PAA (not shown).

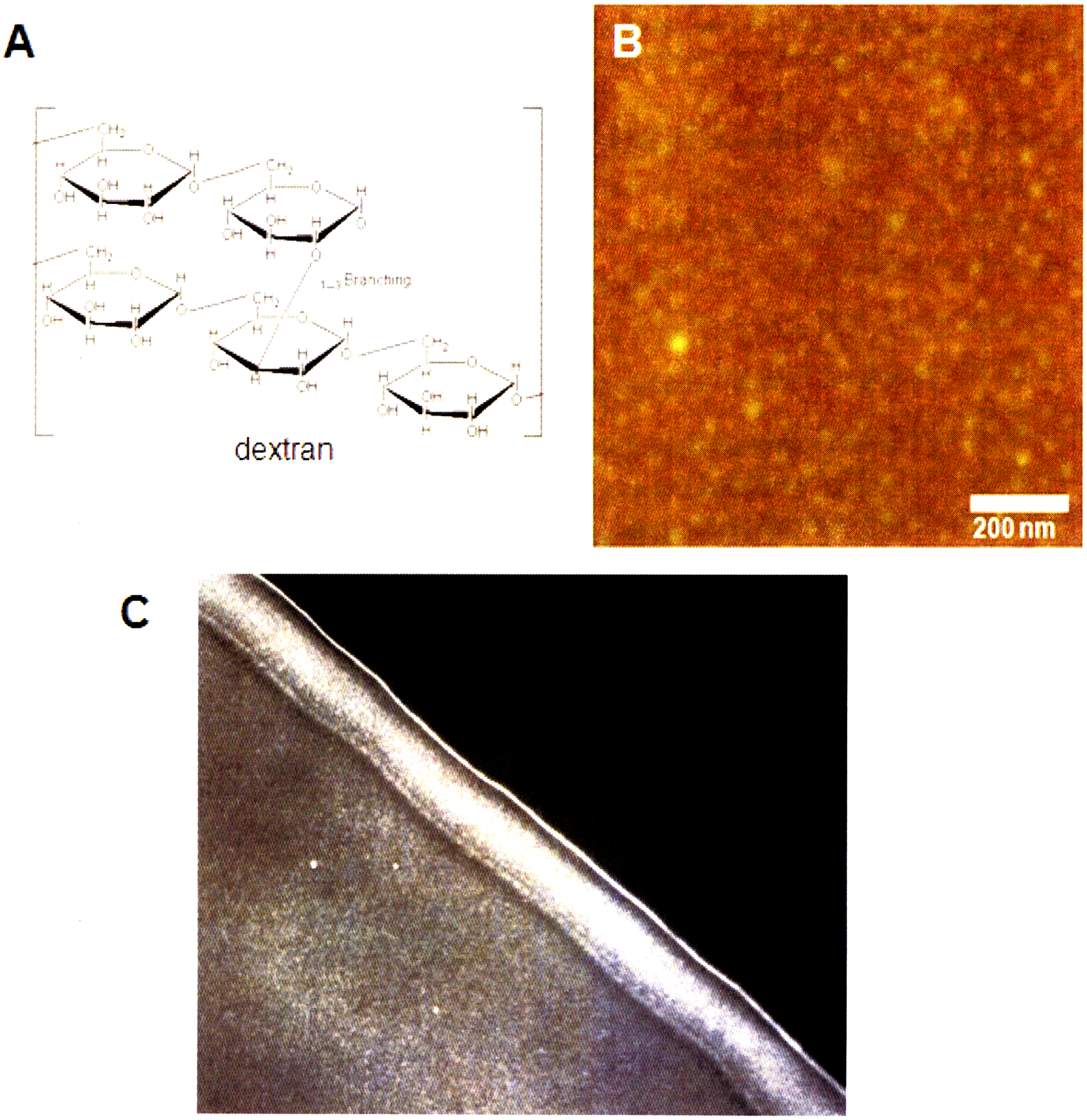

Figure 4-11: (A) Molecular structure of dextran. (B) AFM height image of PS-*b*-P2VP 81k-b-21k micellar thin film cast from toluene after passive loading with dextran(4k)-rhodamine conjugate. Hieght scale is 20 nm. (C) Fluorescence microscopy image of dextran(4k)-rhodamine loaded PS-*b*-P2VP 81k-*b*-21k micellar thin film.

4.3.7. Passive Loading of Dextran into PCL-*b*-P2VP Micelles in Toluene and Oleic Acid

Passive loading experiments were also perfomed with PCL-*b*-P2VP micelles in toluene and oleic acid, using the same method described above for PS-*b*-PAA and PS-*b*-P2VP micelles in toluene. We were able to investigate the effect of varying dextran molecular weight by using 3 different molecular weights (4 kDa, 55 kDa and 76 kDa) as well as the effect of PCL block length with PCL block lengths of 35k, 26k and 19k all paired with the same 21k P2VP block. The loadings achieved using this passive loading technique are several orders of magnitude lower than achieved by agitating solutions in the preceding sections. Here we report the loading as a function of total block copolymer weights (as opposed to per unit weight P2VP block as above) to better highlight the effect of varying the block length of PCL.

We generally observe a trend of increasing loading with decreasing dextran molecular weight and decreasing loading per unit weight of polymer with increasing PCL block length. Loadings are slightly higher in oleic acid compared to toluene. Loading results for PCL-*b*-P2VP 35k-b-21k in toluene do not agree with these trends. The experiments in toluene were only performed a single time and were done to provide a first pass comparison to results in oleic acid. It is possible that experimental error explains these results, as the experiments are sensitive to disturbing the solutions and causing mixing of the two phases, and that repetition of this experiment would produce different results in agreement with the overall trends.

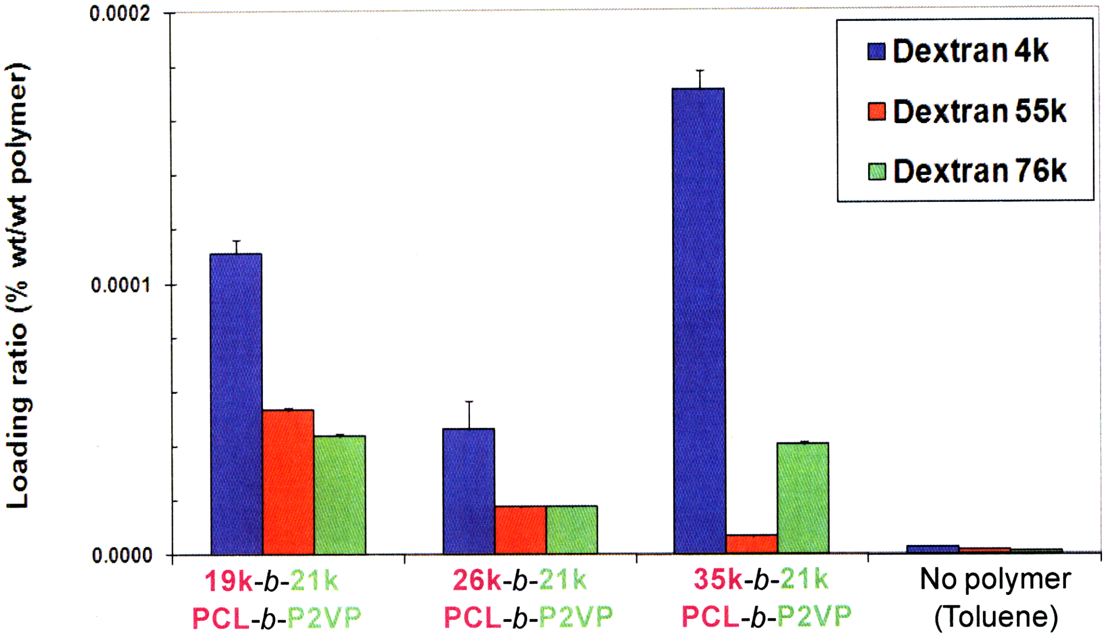

Figure 4-12: Passive loading of three dextran molecular weights into PCL-*b*-P2VP block copolymer micelle in toluene with three different PCL block lengths. Error bars represent the standard deviation of 3 different measurements of the same experiment.

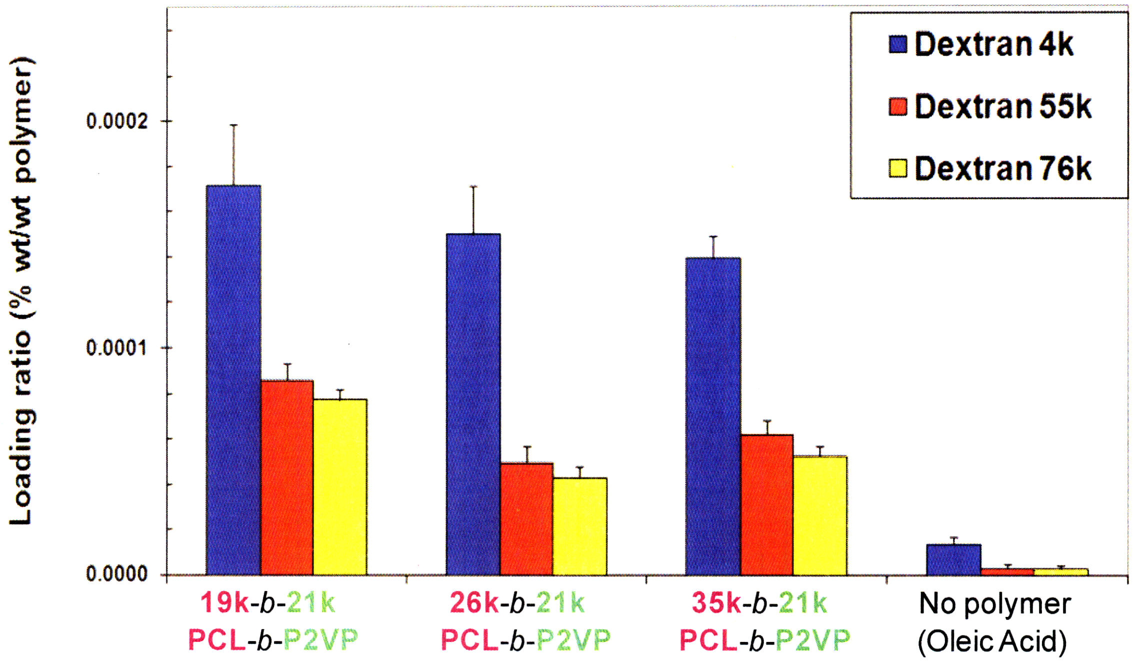

Figure 4-13: Passive loading of three dextran molecular weights into PCL-*b*-P2VP block copolymer micelle in oleic acid with three different PCL block lengths. Error bars represent the standard deviation of 3 independent experiments.

4.3.8. Release of Ovalbumin from PCL-*b*-P2VP Micellar Thin Films upon Exposure to Aqueous Solutions

Micellar thin films cast from toluene could serve as a film-based drug delivery system. To measure the release profile of ovalbumin from micellar thin films we solvent cast films into 96 well plates. The films contained 1 mg of polymer. We were not able to measure film thickness inside of the individual wells, but based on the surface area of the wells and the amount of polymer present, average film thickness was calculated to be around 20 μm. Films were then incubated in PBS with 1 % w/v BSA and the concentration of OVA-TR was monitored over time.

We observed release that was sustained for around 48 hours in the case of PCL-*b*-P2VP polymers. Less than 50% of the loaded ovabumin was released from the PCL-*b*-P2VP, but this was much more than was released from the PS-*b*-P2VP film, which released less than 10% of the loaded ovalbumin over 96 hours. The release profile for PS-*b*-P2VP displayed linear behavior for the 96 hour measurement window. We have studied the cavitation of micellar thin films in detail in chapter 3, however, we are only able to observe the behavior of the top layer of micelles with AFM imaging. So we would expect the degradable polymer, PCL-*b*-P2VP to release a higher percentage of the ovalbumin that was initially loaded. However, this polymer hydrolysis is expected to happen on a much longer time scale than we observed in this experiment. Further experiment with film thickness measurements would need to be performed to investigate the difference in behavior of the polymer micelle thin films. However, this shows the potential of the micelle film for release applications. Release experiments with 'actively' loaded micelles, where much higher loading were achieved, were not performed.

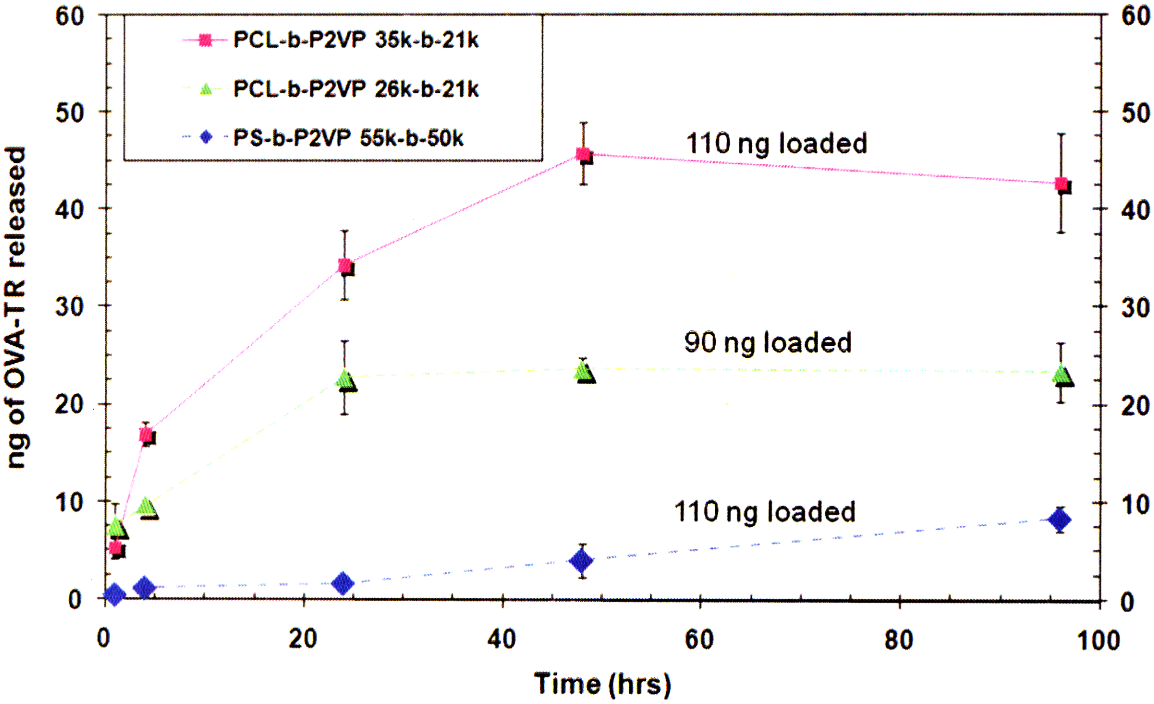

Figure 4-14: Release of ovalbumin from micellar thin films of PCL-*b*-P2VP 35k-*b*-21k and 26k-b-21k, as well as PS-*b*-P2VP 55k-b-50k. Error bars represent standard deviation of 3 samples within the same experiment.

4.3.9. AFM Analyses of Close-Packed PCL-*b*-P2VP Micellar Thin Films Loaded with Ovalbumin and Exposed to PBS

For the release experiment described above, we have cast close-packed micellar thin films, similar the PS-*b*-PAA films we studied in detail in chapters 2 and 3. We wanted to examine the rearrangement of these micelle thin films upon exposure to PBS solutions. Figure 4-1 shows the cavitation observed in micelle films where there was separation between adjacent micelles. This allowed for characterization of individual micelle size, but is not the type of film that would be used for controlled release applications. Figure 4-15 shows AFM images of close-packed PCL-*b*-P2VP cast from toluene and treated in PBS for 16 hours. Cavitation similar to that discussed in chapter 3 for PS-*b*-PAA and PS-*b*-P2VP was observed. The image of the as-cast films show distinct cracks in the micelles films. These cracks were observe intermittently in imaging of PCL-*b*-P2VP thin films and are believe to be cause by volume shrinking upon solvent evaporation. These did not observe this for PS based polymers and it may be due to the semicrystalline nature of PCL.

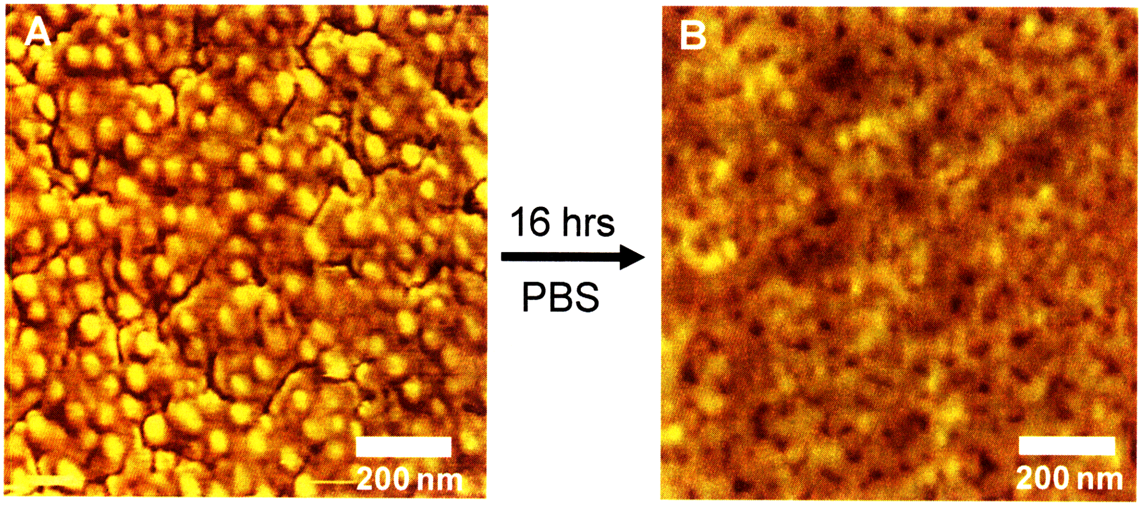

Figure 4-15: AFM images of PCL-*b*-P2VP close-packed micelle thin film (A) as-cast from toluene (phase image, scale = 50°) and (B) after 16 treatment in PBS (height image, scale = 20 nm.

We also investigated close-packed micelle films of OVA loaded PCL-*b*-P2VP and the resulting rearrangement upon PBS solution treatment via AFM. The same cavitation behavior (Figure 4-16) as seen in non-loaded micelles (Figure 4-15) was observed. Upon close inspection of the phase images of PBS treated films, small circular features are visible that are not seen in the cavitated non-loaded micelle thin films. These features are very similar to the streptavidin protein that is seen in Figure B-2. Based on this, we suggest that these features are ovalbumin protein which deposited on the surface of the film after release from micelles.

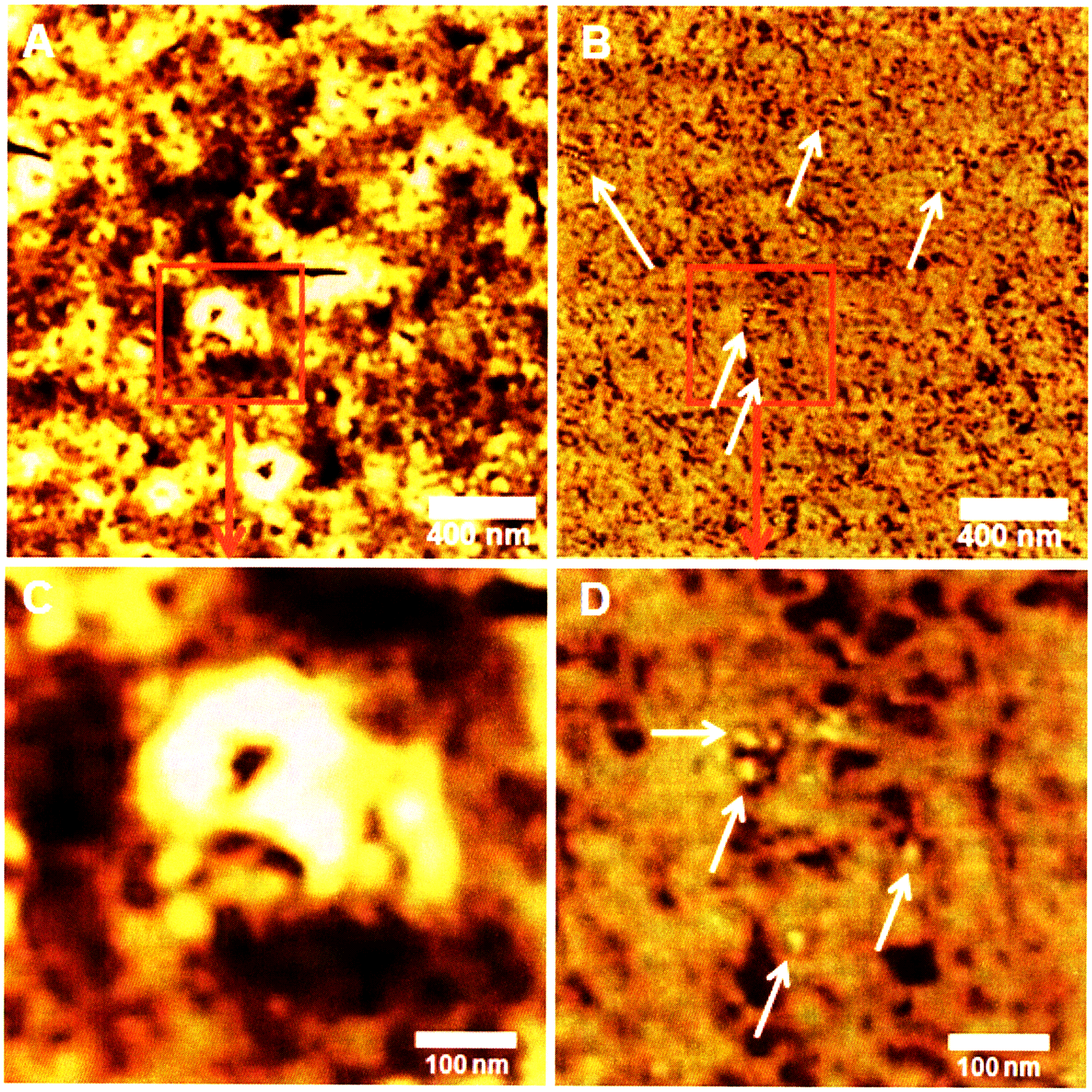

Figure 4-16: AFM height (A) and phase (B) images of ovalbumin loaded PCL-*b*-P2VP micellar thin films after 16 hr treatment in PBS. Zoom in of image A (C) and image B (D).

4.4. Conclusions

We characterized the self-assembly of PCL-*b*-P2VP block copolymers in both toluene and a pharmaceutically relevant solvent, oleic acid, and analyzed the loading of two model globular proteins into micelles formed in each of these solvents. In nonpolar toluene, PCL-b-P2VP formed spherical micelles (~150 nm diam.) with a P2VP core and

PCL corona, while in oleic acid, the data suggest that micelles (~ 150 nm diam.) with a PCL core and P2VP corona were formed. Both ovalbumin and bovine serum albumin could be loaded into micelles in either solvent, demonstrating the ability of PCL-b-P2VP micelles to sequester protein into a P2VP core or P2VP corona in organic phases. Notably, block copolymer micelles formed in oleic acid, where protein was sequestered in the P2VP corona, obtained the highest level of protein loading (~8% wt/(wt P2VP)). On contact of these protein-loaded oleic acid/block copolymer solutions with an aqueous reservoir, transfer of protein from the oil phase back into aqueous solution was sustained for ~30 hours. This work demonstrates a unique mode of protein cargo sequesterization for micelles formed in oil phases (solute loading in the micelle corona), and illustrates the potential of block copolymer micelles assembled in biocompatible oils to serve as carriers for sustained release of hydrophilic macromolecular cargos. We have also successfully loaded the small molecule calmagite and the polysaccharide dextran, into PCL-*b*-P2VP micelles and observed ova protein release form micelle thin films cast from toluene, suggesting the use of these micelles for film-based delivery.

Chapter 5 CONCLUSIONS

The work presented in this thesis has focused on block copolymer micelle self-assembly. When cast from volatile solvents, micellar thin films are created with ordered 2-D arrays of structures on the nanometer length scale, providing the opportunity for a range of applications. Control over the size and spacing of these films on the nanometer length scale and patterning of films on the micron length scale are important tool for the successful implementation of micellar thin films.

Chapter 2 presents strategies for control over these film properties using PS-*b*-PAA was used as a model block copolymer system. The strategies to control the size and spacing of micelle films on the nanometer length scale include alteration of the block copolymer molecular weight, addition of PS homopolymer, combination of different micellar solutions, and spin-casting from dilute solution. This work demonstrated the use of microcontact printing to create lined and circular periodic patterns of PS-*b*-PAA films on the micron length scale. Convective self-assembly using microfluidic channels was also used to create lined patterns. These strategies could be applied to a variety of block copolymer systems and further the potential of block copolymers systems for applications where control over the length scale of patterning is essential.

Creating a patterned film of molecules, such as proteins, by selectively functionalizing one polymer block of the micelle post-casting is one possible route to take advantage of the block copolymer micelle template. For PS-*b*-PAA, treatment in aqueous solution lead to the micellar rearrangement, creating cavities in the film. The work in Chapter 3 study this rearrangement, or cavitation process in detail. Solvent polarity, pH and ionic strength of the aqueous solution determine whether a micellar film of a given molecular weight and composition will cavitate and expose the PAA chains to film surface. The resulting cavity size is also dependent on these variables. Selective functionalization of the PAA domains of PS-*b*-PAA thin films using EDC chemistry with a biotin linker molecule and subsequently, the protein streptavidin were demonstrated. This confirmed the availability of the carboxylic acid moieties of the PAA domains to post-cavitation chemistry, illustrating the potential of this copolymer micelle system to act as a template for a variety of molecules using straight-forward conjugation chemistry. This cavitation phenomena was also demonstrated in cylindrical PS-*b*-P2VP micelles.

Chapter 4 presents work with block copolymer micelle for a different application direction. Block copolymer micelles formed in biocompatible oil phases could be of interest in biomedical applications as carriers for therapeutic molecules, imaging agents, or vaccine adjuvants. Micelles ability to encapsulate and solubilize molecules in phases in which they would be otherwise insoluble has been widely demonstrated. The work in chapter 4 demonstrates the loading and release of proteins from micelles of the block copolymer, PCL-*b*-P2VP. We characterized the self-assembly of PCL-*b*-P2VP block copolymers in both toluene and a pharmaceutically relevant solvent, oleic acid, and analyzed the loading of two model globular proteins into micelles formed in each of these solvents. In nonpolar toluene, PCL-b-P2VP formed spherical micelles (~150 nm diam.) with a P2VP core and PCL corona, while in oleic acid, the data suggest that micelles (~ 150 nm diam.) with a PCL core and P2VP corona were formed. Globular proteins could be loaded into micelles in either solvent, demonstrating the ability of PCL-b-P2VP micelles to sequester protein into a P2VP core or P2VP corona in organic phases.

Notably, block copolymer micelles formed in oleic acid, where protein was sequestered in the P2VP corona, obtained the highest level of protein loading (~8% wt/(wt P2VP)). On contact of these protein-loaded oil/block copolymer solutions with an aqueous reservoir, transfer of protein from the oil phase back into aqueous solution was sustained for ~30 hours. This work demonstrates a unique mode of protein cargo sequesterization for micelles formed in oil phases (solute loading in the micelle corona), and illustrates the potential of block copolymer micelles assembled in biocompatible oils to serve as carriers for sustained release of hydrophilic macromolecular cargos.

Chapter 6 APPENDIX

6.1. Appendix for: Strategies for Controlling the Size, Spacing and Patterning of Inverse Micelle Thin Films

6.1.1. Covalent Cross-linking of PS-*b*-PAA Micelle Cores

As discussed in chapter 2, the mixing of different micelle solutions could be a way to control the spacing of PAA domains in PS-*b*-PAA micelle thin films and their resulting carboxylic acid moieties available to solution after cavitation. One way to accomplish this would be to selectively suppress the cavitation of micelles from one solution by covalently cross-linking the PAA micelle core. We attempted to do this using EDC chemistry, the same chemistry we used to couple proteins to the surface of cavitated micelle thin films in Chapter 3. 5 mg of EDC (powder) and 5 mg of ethylene diamine (liquid) were added with stirring to 1 mL of a 10 mg/mL PS-*b*-PAA micelle solution in toluene. The solution was allowed to react at room temperature for one hour before the solution was washed with water in an attempt to scrub any extra EDC and ethylene diamine out of the toluene solution. Films were cast from micelle solution and analyzed by FTIR analysis in an attempt to observe amide bond formation. However, films cast from micelle solution exposed to this reaction showed no difference from as-assembled micellar films. Subsequently, NHS ester (5 mg per 1 mL micelle solution) was added to the reaction scheme and the solution was heated to 50 °C, but no crosslinking was detected by FTIR. We cast films of 'crosslinked' micelles and exposed them to 30 minute aqueous solution treatment, and the micelles cavitated. We were unsuccessful in detecting micelle core crosslinking by FTIR. We also tested films for cavitation, and 'crosslinked' micelles cavitated during 15 minute treatment in PBS, similar to as-assembled micelles. However, in the light of the micelle loading results in chapter 4 where hydrophilic compounds are able to be loaded in to micelle cores, it seems that micelle crosslinking should be possible. It is possible that by more vigorous mixing and the use of a more hydrophilic, multiarm amine molecule may facilitate PAA domain crosslinking.

6.2. Appendix for: Cavitation and Creation of Functional Nanocavities

6.2.1. Delamination of Individual Micelles from Close-packed Micelle Thin Films

In chapter 3, we demonstrated the rearrangement of PS-*b*-PAA and PS-*b*-P2VP micelle thin films upon exposure to aqueous solutions. One of the issues faced when exposing films to aqueous solution was micelle film delamination from the silicon or glass substrate. In order to prevent this film delamination, we used substrates that were coated with a polyelectrolyte multilayer (PEM) film. The PEM consisted of five bilayers of polyallylamine hydrochloride (PAH) dipped at a concentration of 10 mM on a repeat unit basis at pH 3.5 with 0.1 M NaCl and sulfonated polystyrene (SPS) at a concentration of 10 mM on a repeat unit basis at pH 3.5 with 0.1 M NaCl. A film consisting of three and a half bilayers of PAH dipped at pH 7.5 and a concentration of 10 mM on a repeat unit basis and poly(acrylic acid) dipped at pH 3.5 at a concentration of 10 mM on a repeat unit basis was then deposited on top. This results in a film with a PAH top layer and a water advancing contact angle of 70° as described elsewhere.[75] This adhesion layer prevented bulk film delamination for aqueous solution treatment time tested up to 8 days and alcohol (n-butanol, n-octanol) treatment times of the same durations. No bulk delamination was observed in these films but for films treated for 17 hours in 0.01M NaOH (pH 12) AFM analysis showed that films contained holes, which appear to correspond to individual or small numbers of micelles being extracted from the film (Figure 6-1:). The mechanism of this micelle extraction is not known and was not further investigated here.

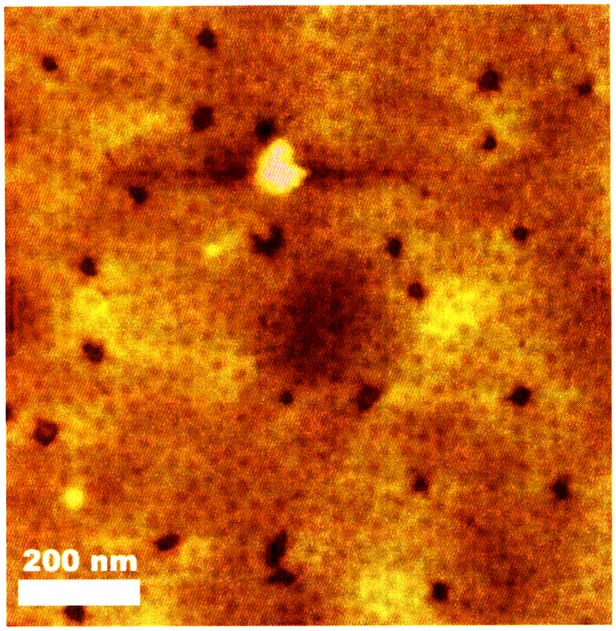

Figure 6-1: AFM height image showing delamination of individual micelles from micellar films treated for 17 hours in 0.01M NaOH. Height scale is 20 nm.

6.2.2. Protein Coupling to Micelle Films Cast from PS-*b*-PAA Solution Containing PS Homopolymer

In chapter 3, we demonstrate the selective coupling of a NH_2-triethylene glycol-biotin linker molecule and streptavidin, alexa fluor conjugate to cavitated PS-*b*-PAA 16.5-*b*-4.5 micelle thin films using EDC chemistry. The EDC link the carboxylic acid moiety of the PAA block to the primary amine of the biotin linker molecule. Combining this chemistry with our work in chapter 2 demonstrating the control over the size, spacing and patterning of PS-*b*-PAA micelle thin films could allow for the creation of well defined protein arrays, with potentially nanoclustered proteins of defined cluster size separated by a controllable distance from adjacent clusters. One of the ways by which control over the micelle spacing was achieved was by dilution the block copolymer solution in toluene with PS homopolymer before spin casting. This leads to films containing micelles spaced apart by regions of PS homopolymer (Figure 2-4). We have performed the same coupling reaction applied to close-packed PS-*b*-PAA micelle thin films to films created with PS homopolymer dilutions up to a molar ratio of [PS:PS-*b*-PAA) of 100:1. The fluorescence intensity of film exposed to the full coupling reaction was indistinguishable from film exposed to control reactions excluding the biotin linker molecule or EDC (data not shown). We additionally performed AFM imaging of films to investigate protein binding. Imaging showed a significant amount of protein bound to the PS homopolymer regions between micelles for film treated with a control reaction lacking the biotin linker molecule.

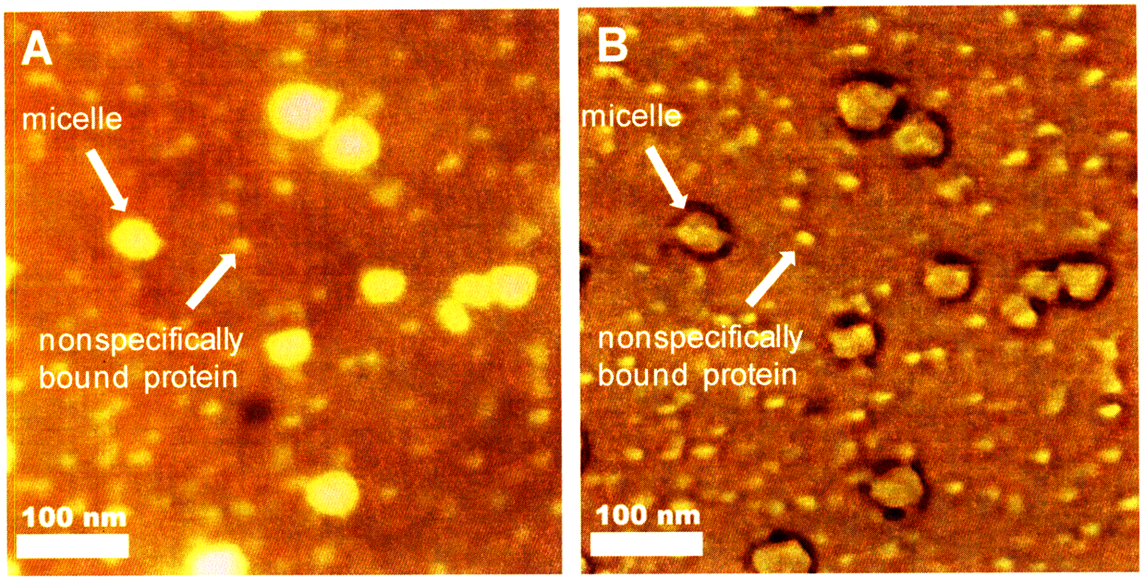

Figure 6-2: AFM height (A) and phase (B) images of PS-*b*-PAA micelle thin film cast from toluene with a 100:1 molar ratio of [PS:PS-*b*-PAA] exposed to control reaction excluding the NH_2-triethylene glycol-biotin linker molecule. Arrows point to micelle (larger objects) and nonspecifically bound protein (smaller objects) respectively.

6.3. Appendix for: Block Copolymer Micelles as Nanocontainers for Controlled Release

6.3.1. PCL-*b*-P2VP Micelle in Oleic Acid for Transdermal Drug Delivery

As discussed in chapter 4, one application that the oil phase, oleic acid, has been investigated for is as a chemical permeation enhancer for transdermal drug delivery delivery.[38-41] Oleic acid interacts with lipid membranes in the skin, particularly the stratum corneum, increasing the flux of therapeutic molecule through the skin. We performed pilot experiments to investigate the penetration of texas red labeled ovalbumin protein (ova-TR) into live mouse skin.

Experiments were peformed on C57BL/6 mice under isofluorene anesthesia. PDMS slabs approximately 1.5 cm x 1.5 cm were hand cut and subsequently hole-punched so that an annular region was cut through the PDMS. Double-sided medical adhesive tape was used to adhere the chambers to the skin. Tape was first applied to the chamber and then the annular region was cut out before applying on the skin. Incubation time was 3 hours. Experiments with three different solutions were performed: (1) ova-TR loaded 10 mg/mL PCL-*b*-P2VP 35k-*b*-21k in oleic acid, (2) PBS solution of ova-TR and (3) an emulsion of oleic acid and ova-TR in PBS. All solutions contained 0.3 ug/uL of ova-TR.

A general structure of the skin is seen in Figure 6-3. There are three particular cell type that we will use to benchmark skin penetration. The uppermost layers (closest to skin surface) consist of large keratinocytes. Directly below this layer are smaller keratinocytes and within these layers are langerhans cells (LCs). LCs are the resident dendritic cells in the epidermis, which serve to detect antigen and stimulate an immune response to foreign antigens by undergoing maturation and migration to the lymph nodes where they activate T-lymphocytes This cell type is of particular interest for transdermal vaccines, due to their ability to elicit an immune response.

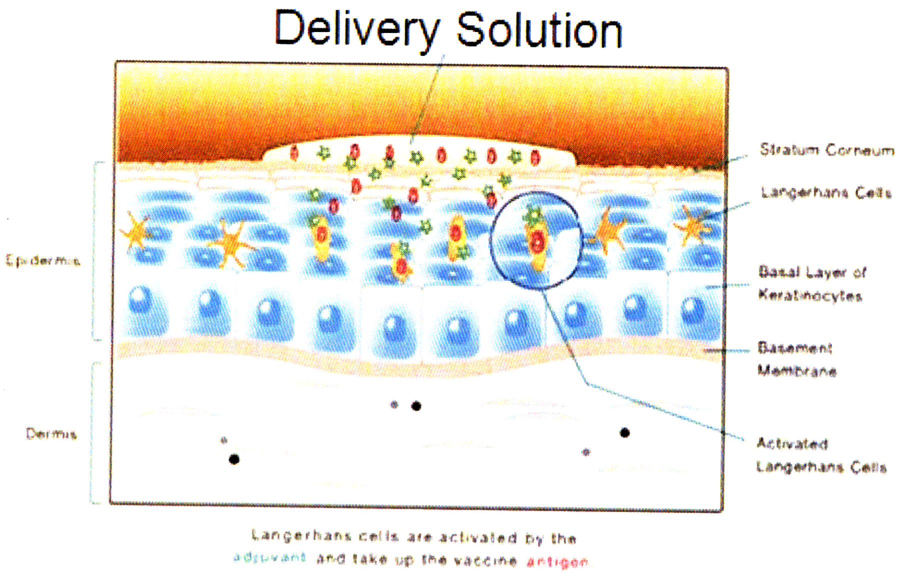

(from Iomai Vaccines)

Figure 6-3: Schematic cross-section of the skin.

To analyze the penetration of fluorescently labeled ova, we excised the mouse ear at the end of the experiment and imaged the skin in the confocal microscope. Z-sections were taken parallel to the skin. The skin cell types discussed above and their known sizes and locations were used to asses skin penetration. Skin sections were stained using anti-MHC class II antibody to stain the surface of LCs and cytosolic staining was performed for all cell types.

We can identifty each of these cell types from individual z-sections from the same experiment. We can see the larger keratinocytes in Figure 6-4, smaller keratinocytes in Figure 6-5 and LCs in Figure 6-6. The z-sections in Figure 6-5 and Figure 6-6 are 5 μm and 12 μm below the z-section Figure 6-4 respectively. These images are from a single experiment where mouse skin exposed to a PCL-*b*-P2VP micelle solution in oleic acid loaded with OVA-TR.

Similar penetration profiles to those in Figure C-1, C-2 and C-3 were observed for all experiments with PCL-*b*-P2VP micelles in oleic acid loaded with ova-TR, PBS OVA-TR solutions and PBS ova-TR solutions emulsified in oleic acid. Pentration was seen around the larger keratinocytes, and small areas where ova-TR reached the small keratinocyte layer, but no penetration to the depth of the langerhans cells was observed. This indicates that oleic acid, and PCL-*b*-P2VP micelles in oleic acid may not be an effective way of delivering antigen to langerhans cells, as similar penetration can easily be obtained with PBS solutions of ova-TR.

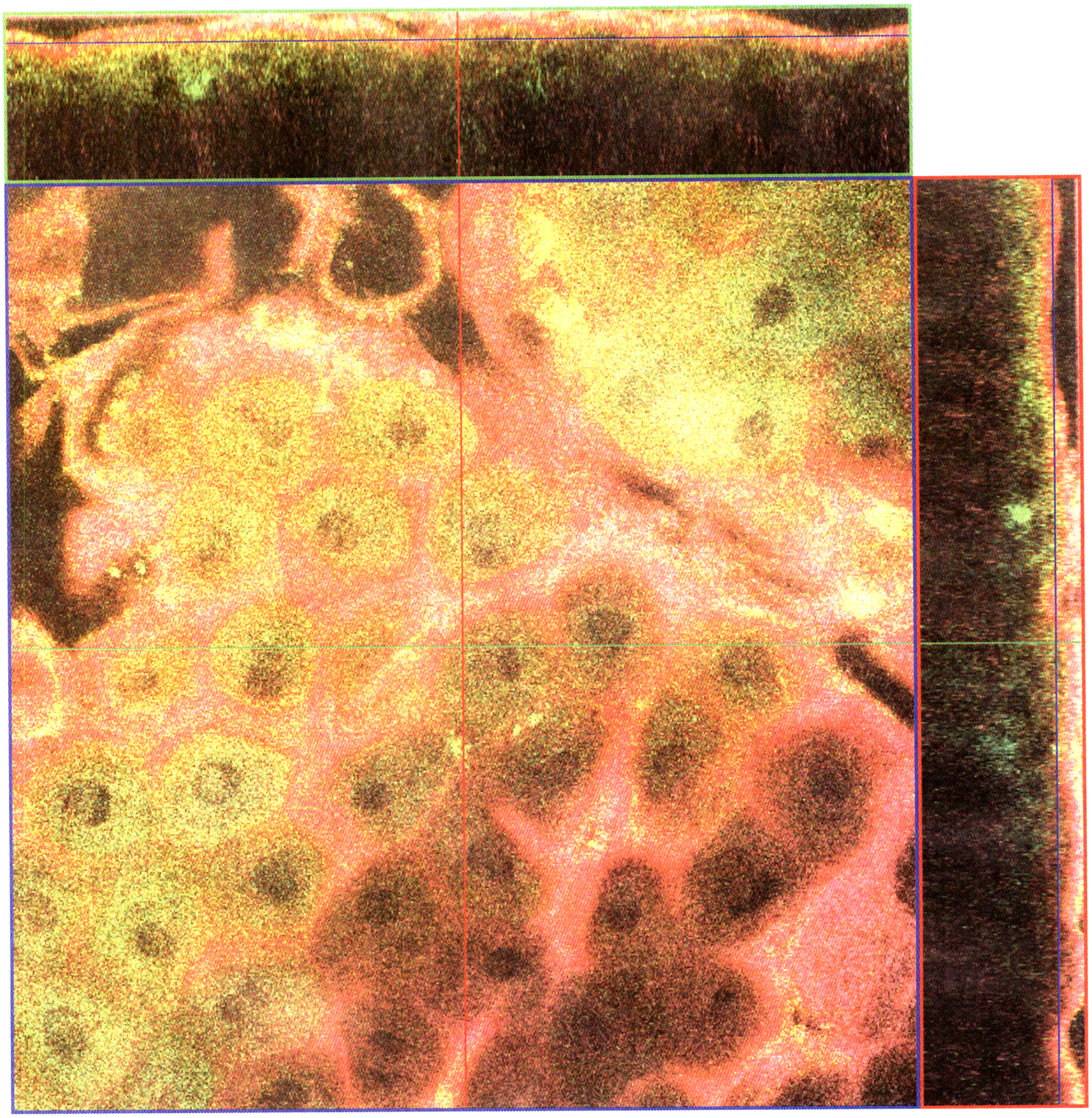

Figure 6-4: Penetration of OVA-TR (red fluorescence) around larger keratinocytes delivered from PCL-*b*-P2VP micelle solution in oleic acid. Green fluorescence is probably due to non-specific background staining of keratinocytes by the FITC anti-MHC II antibody and appears to accumulate in the cytosol. The dark central regions are the cell nucleus.

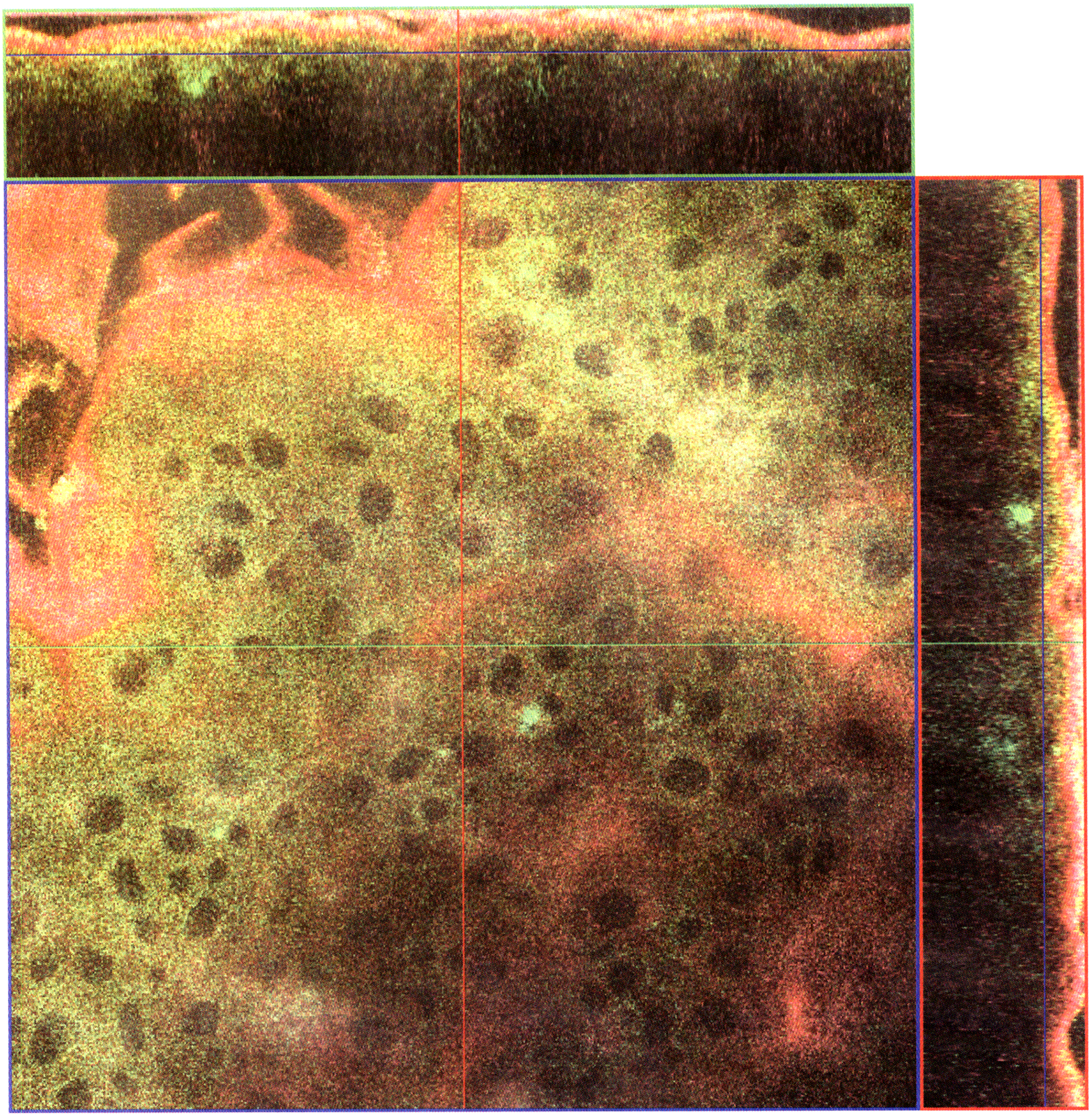

Figure 6-5: Skin sample exposed to PCL-*b*-P2VP micelles loaded with OVA-TR in oleic acid. Green fluorescence (showing smaller keratinocytes) is probably due to non-specific background staining of keratinocytes by the FITC anti-MHC II antibody and appears to accumulate in the cytosol. Dark regions represent the cell nucleus. This z-section is 5 um below Figure C-2, which shows the larger keratinocytes.

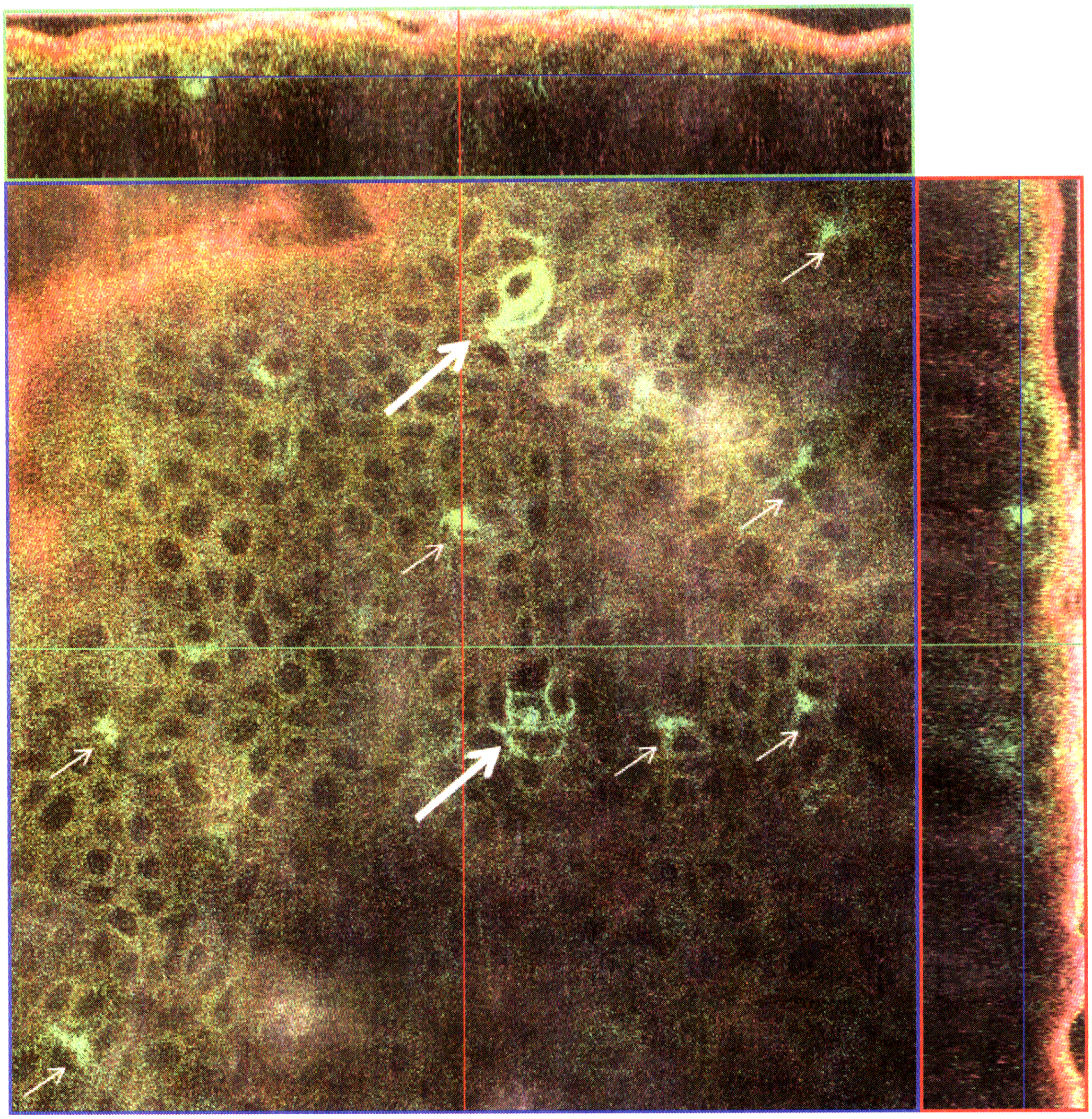

Figure 6-6: Antibody staining of the surface of Langerhans Cells (LCs) in the skin, after exposure to PCL-*b*-P2VP micelles loaded with OVA-TR in oleic acid.. The green fluorescence shows the FITC anti-MHC II antibody staining. Red fluorescene in ova-TR. Large white arrows indicate LCs and small arrows indicate what appear to be LCs, but are not stained effectively or out of focus in this z-section. This z-section is 12 um below Figure C-2, which shows the larger keratinocytes and 7 um below Figure C-3.

Chapter 7 REFERENCES

1. Price, C., In *Developments in Block Copolymers*, Goodman, I., Ed. Applied Science Publishers: London, 1982; Vol. 1, pp 39-79.
2. Moffitt, M.; Khougaz, K.; Eisenberg, A. *Accounts of Chemical Research* **1996,** 29, (2), 95-102.
3. Terris, B. D.; Thomson, T. *Journal of Physics D-Applied Physics* **2005,** 38, (12), R199-R222.
4. Hamley, I. W. *Nanotechnology* **2003,** 14, (10), R39-R54.
5. Harrison, C.; Park, M.; Chaikin, P. M.; Register, R. A.; Adamson, D. H. *Journal of Vacuum Science & Technology B* **1998,** 16, (2), 544-552.
6. Harrison, C. K.; Adamson, D. H.; Park, M.; Chaikin, P. M.; Register, R. A. *Abstracts of Papers of the American Chemical Society* **1997,** 214, 116-Pmse.
7. Park, M.; Harrison, C.; Chaikin, P. M.; Register, R. A.; Adamson, D. H. *Science* **1997,** 276, (5317), 1401-1404.
8. Harrison, C.; Park, M.; Chaikin, P.; Register, R. A. *Abstracts of Papers of the American Chemical Society* **1996,** 212, 143-Poly.
9. Glass, R.; Arnold, M.; Cavalcanti-Adam, E. A.; Blummel, J.; Haferkemper, C.; Dodd, C.; Spatz, J. P. *New Journal of Physics* **2004,** 6, -.
10. Gorzolnik, B.; Mela, P.; Moeller, M. *Nanotechnology* **2006,** 17, (19), 5027-5032.
11. Jung, J. M.; Kwon, K. Y.; Ha, T. H.; Chung, B. H.; Jung, H. T. *Small* **2006,** 2, (8-9), 1010-1015.
12. Bratton, D.; Yang, D.; Dai, J. Y.; Ober, C. K. *Polymers for Advanced Technologies* **2006,** 17, (2), 94-103.

13. Haupt, M.; Ladenburger, A.; Sauer, R.; Thonke, K.; Glass, R.; Roos, W.; Spatz, J. P.; Rauscher, H.; Riethmuller, S.; Moller, M. *Journal of Applied Physics* **2003,** 93, (10), 6252-6257.

14. Fu, Q.; Huang, S. M.; Liu, J. *Journal of Physical Chemistry B* **2004,** 108, (20), 6124-6129.

15. Yun, S. H.; Sohn, B. H.; Jung, J. C.; Zin, W. C.; Lee, J. K.; Song, O. *Langmuir* **2005,** 21, (14), 6548-6552.

16. Yoo, S. I.; Sohn, B. H.; Zin, W. C.; An, S. J.; Yi, G. C. *Chemical Communications* **2004**, (24), 2850-2851.

17. Cresce, A. V.; Silverstein, J. S.; Bentley, W. E.; Kofinas, P. *Macromolecules* **2006,** 39, (17), 5826-5829.

18. Cavalcanti-Adam, E. A.; Bezler, M.; Tomakidi, P.; Spatz, J. P. *Journal of Bone and Mineral Research* **2004,** 19, S64-S64.

19. Cavalcanti-Adam, E. A.; Micoulet, A.; Blummel, J.; Auernheimer, J.; Kessler, H.; Spatz, J. P. *European Journal of Cell Biology* **2006,** 85, (3-4), 219-224.

20. Groll, J.; Albrecht, K.; Gasteier, P.; Riethmueller, S.; Ziener, U.; Moeller, M. *Chembiochem* **2005,** 6, (10), 1782-1787.

21. Boontongkong, Y.; Cohen, R. E. *Macromolecules* **2002,** 35, (9), 3647-3652.

22. Whitesides, G. M.; Ostuni, E.; Takayama, S.; Jiang, X. Y.; Ingber, D. E. *Annual Review of Biomedical Engineering* **2001,** 3, 335-373.

23. Xia, Y. N.; Whitesides, G. M. *Annual Review of Materials Science* **1998,** 28, 153-184.

24. Kane, R. S.; Takayama, S.; Ostuni, E.; Ingber, D. E.; Whitesides, G. M. *Biomaterials* **1999,** 20, (23-24), 2363-2376.

25. Zhao, X. M.; Xia, Y. N.; Whitesides, G. M. *Journal of Materials Chemistry* **1997,** 7, (7), 1069-1074.

26. Jiang, X. P.; Zheng, H. P.; Gourdin, S.; Hammond, P. T. *Langmuir* **2002,** 18, (7), 2607-2615.

27. Qiu, L. Y.; Zheng, C.; Jin, Y.; Zhu, K. J. E. *Expert Opinion on Therapeutic Patents* **2007,** 17, (7), 819-830.

28. Mahmud, A.; Xiong, X. B.; Aliabadi, H. M.; Lavasanifar, A. *Journal of Drug Targeting* **2007,** 15, (9), 553-584.

29. Park, J. H.; Lee, S.; Kim, J. H.; Park, K.; Kim, K.; Kwon, I. C. *Progress in Polymer Science* **2008,** 33, (1), 113-137.

30. Peer, D.; Karp, J. M.; Hong, S.; FaroKHzad, O. C.; Margalit, R.; Langer, R. *Nature Nanotechnology* **2007,** 2, (12), 751-760.

31. Porter, C. J. H.; Charman, W. N. *Advanced Drug Delivery Reviews* **1997,** 25, (1), 71-89.

32. Holm, R.; Mullertz, A.; Pedersen, G. P.; Kristensen, H. G. *Pharmaceutical Research* **2001,** 18, (9), 1299-1304.

33. Wasan, K. M. *Drug Development and Industrial Pharmacy* **2002,** 28, (9), 1047-1058.

34. Strickley, R. G. *Pharmaceutical Research* **2004,** 21, (2), 201-230.

35. Fukui, H.; Murakami, M.; Yoshikawa, H.; Takada, K.; Muranishi, S. *Journal of Pharmacobio-Dynamics* **1987,** 10, (6), 236-242.

36. Aungst, B. J. *Journal of Pharmaceutical Sciences* **2000,** 89, (4), 429-442.

37. Tsutsumi, K.; Obata, Y.; Takayama, K.; Loftsson, T.; Nagai, T. *Drug Development and Industrial Pharmacy* **1998,** 24, (8), 757-762.

38. Williams, A. C.; Barry, B. W. *Advanced Drug Delivery Reviews* **2004,** 56, (5), 603-618.

39. Thong, H. Y.; Zhai, H.; Maibach, H. I. *Skin Pharmacology and Physiology* **2007,** 20, (6), 272-282.

40. Sinha, V. R.; Kaur, M. P. *Drug Development and Industrial Pharmacy* **2000,** 26, (11), 1131-1140.

41. Aungst, B. J. *Pharmaceutical Research* **1989,** 6, (3), 244-247.

42. Gupta, R. K.; Varanelli, C. L.; Griffin, P.; Wallah, D. F. H.; Siber, G. R. *Vaccine* **1996,** 14, (8), R1-R1.

43. Whitesides, G. M.; Mathias, J. P.; Seto, C. T. *Science* **1991,** 254, (5036), 1312-1319.

44. Thurn-Albrecht, T.; Schotter, J.; Kastle, C. A.; Emley, N.; Shibauchi, T.; Krusin-Elbaum, L.; Guarini, K.; Black, C. T.; Tuominen, M. T.; Russell, T. P. *Science* **2000,** 290, (5499), 2126-2129.

45. Li, R. R.; Dapkus, P. D.; Thompson, M. E.; Jeong, W. G.; Harrison, C.; Chaikin, P. M.; Register, R. A.; Adamson, D. H. *Applied Physics Letters* **2000,** 76, (13), 1689-1691.

46. Black, C. T.; Guarini, K. W.; Milkove, K. R.; Baker, S. M.; Russell, T. P.; Tuominen, M. T. *Applied Physics Letters* **2001,** 79, (3), 409-411.

47. Park, M.; Chaikin, P. M.; Register, R. A.; Adamson, D. H. *Applied Physics Letters* **2001,** 79, (2), 257-259.

48. Cheng, J. Y.; Ross, C. A.; Thomas, E. L.; Smith, H. I.; Vancso, G. J. *Applied Physics Letters* **2002,** 81, (19), 3657-3659.

49. Lazzari, M.; Lopez-Quintela, M. A. *Advanced Materials* **2003,** 15, (19), 1583-1594.

50. Bates, F. S.; Fredrickson, G. H. *Annual Review of Physical Chemistry* **1990,** 41, 525-557.

51. Spatz, J. P.; Herzog, T.; Mossmer, S.; Ziemann, P.; Moller, M. *Advanced Materials* **1999,** 11, (2), 149-153.

52. Spatz, J. P.; Mossmer, S.; Hartmann, C.; Moller, M.; Herzog, T.; Krieger, M.; Boyen, H. G.; Ziemann, P.; Kabius, B. *Langmuir* **2000,** 16, (2), 407-415.

53. Bennett, R. D.; Xiong, G. Y.; Ren, Z. F.; Cohen, R. E. *Chemistry of Materials* **2004,** 16, (26), 5589-5595.

54. Bennett, R. D.; Hart, A. J.; Miller, A. C.; Hammond, P. T.; Irvine, D. J.; Cohen, R. E. *Langmuir* **2006,** 22, (20), 8273-8276.

55. Bennett, R. D.; Miller, A. C.; Kohen, N. T.; Hammond, P. T.; Irvine, D. J.; Cohen, R. E. *Macromolecules* **2005,** 38, (26), 10728-10735.

56. Kumar, A.; Whitesides, G. M. *Applied Physics Letters* **1993,** 63, (14), 2002-2004.

57. Kumar, A.; Biebuyck, H. A.; Whitesides, G. M. *Langmuir* **1994,** 10, (5), 1498-1511.

58. Kumar, A.; Whitesides, G. M. *Science* **1994,** 263, (5143), 60-62.

59. Wang, M. T.; Braun, H. G.; Kratzmuller, T.; Meyer, E. *Advanced Materials* **2001,** 13, (17), 1312-1317.

60. Yan, L.; Huck, W. T. S.; Zhao, X. M.; Whitesides, G. M. *Langmuir* **1999,** 15, (4), 1208-1214.

61. Granlund, T.; Nyberg, T.; Roman, L. S.; Svensson, M.; Inganas, O. *Advanced Materials* **2000,** 12, (4), 269-273.

62. Jang, H.; Kim, S.; Char, K. *Langmuir* **2003,** 19, (8), 3094-3097.

63. Glass, R.; Moller, M.; Spatz, J. P. *Nanotechnology* **2003,** 14, (10), 1153-1160.

64. Glass, R.; Arnold, M.; Blummel, J.; Kuller, A.; Moller, M.; Spatz, J. P. *Advanced Functional Materials* **2003,** 13, (7), 569-575.

65. Yun, S. H.; Sohn, B. H.; Jung, J. C.; Zin, W. C.; Ree, M.; Park, J. W. *Nanotechnology* **2006,** 17, (2), 450-454.

66. Bennett, R. D.; Hart, A. J.; Cohen, R. E. *Advanced Materials* **2006,** 18, (17), 2274-2279.

67. Cong, Y.; Zhang, Z. X.; Fu, J.; Li, J.; Han, Y. C. *Polymer* **2005,** 46, (14), 5377-5384.

68. Li, X.; Tian, S. J.; Ping, Y.; Kim, D. H.; Knoll, W. *Langmuir* **2005,** 21, (21), 9393-9397.

69. Zhang, G. F.; Marie, P.; Maaloum, M.; Muller, P.; Benoit, N.; Krafft, M. P. *Journal of the American Chemical Society* **2005,** 127, (29), 10412-10419.

70. Laforgue, A.; Bazuin, C. G.; Prud'homme, R. E. *Macromolecules* **2006,** 39, (19), 6473-6482.

71. Xu, T.; Stevens, J.; Villa, J. A.; Goldbach, J. T.; Guarim, K. W.; Black, C. T.; Hawker, C. J.; Russell, T. R. *Advanced Functional Materials* **2003,** 13, (9), 698-702.

72. Xu, T.; Goldbach, J. T.; Misner, M. J.; Kim, S.; Gibaud, A.; Gang, O.; Ocko, B.; Guarini, K. W.; Black, C. T.; Hawker, C. J.; Russell, T. P. *Macromolecules* **2004,** 37, (8), 2972-2977.

73. Xu, C.; Fu, X. F.; Fryd, M.; Xu, S.; Wayland, B. B.; Winey, K. I.; Composto, R. J. *Nano Letters* **2006,** 6, (2), 282-287.

74. Xu, C.; Wayland, B. B.; Fryd, M.; Winey, K. I.; Composto, R. J. *Macromolecules* **2006,** 39, (18), 6063-6070.

75. Shiratori, S. S.; Rubner, M. F. *Macromolecules* **2000,** 33, (11), 4213-4219.

76. Katz, J. S.; Doh, J.; Irvine, D. J. *Langmuir* **2006,** 22, (1), 353-359.

77. Yaffe, M. B.; Kramer, E. J. *Journal of Materials Science* **1981,** 16, (8), 2130-2136.

78. Israels, R.; Leermakers, F. A. M.; Fleer, G. J.; Zhulina, E. B. *Macromolecules* **1994,** 27, (12), 3249-3261.

79. Israels, R.; Leermakers, F. A. M.; Fleer, G. J. *Macromolecules* **1994,** 27, (11), 3087-3093.

80. Zhulina, E. B.; Birshtein, T. M.; Borisov, O. V. *Macromolecules* **1995,** 28, (5), 1491-1499.

81. Biesheuvel, P. M. *Journal of Colloid and Interface Science* **2004,** 275, (1), 97-106.

82. Lyatskaya, Y. V.; Leermakers, F. A. M.; Fleer, G. J.; Zhulina, E. B.; Birshtein, T. M. *Macromolecules* **1995,** 28, (10), 3562-3569.

83. Zhulina, E. B.; Borisov, O. V. *Journal of Chemical Physics* **1997,** 107, (15), 5952-5967.

84. Biesalski, M.; Johannsmann, D.; Ruhe, J. *Journal of Chemical Physics* **2002,** 117, (10), 4988-4994.

85. Currie, E. P. K.; Sieval, A. B.; Fleer, G. J.; Stuart, M. A. C. *Langmuir* **2000,** 16, (22), 8324-8333.

86. Ferry, J. D., *Viscoelastic Properties of Polymers*. 3rd ed.; Wiley: New York, 1980.

87. Nishiyama, N.; Kataoka, K. *Pharmacology & Therapeutics* **2006,** 112, (3), 630-648.

88. Gaucher, G.; Dufresne, M. H.; Sant, V. P.; Kang, N.; Maysinger, D.; Leroux, J. C. *Journal of Controlled Release* **2005,** 109, (1-3), 169-188.

89. Torchilin, V. P. *Journal of Controlled Release* **2001,** 73, (2-3), 137-172.

90. Oishi, M.; Sasaki, S.; Nagasaki, Y.; Kataoka, K. *Biomacromolecules* **2003,** 4, (5), 1426-1432.

91. Saunders, R. S.; Cohen, R. E.; Schrock, R. R. *Macromolecules* **1991,** 24, (20), 5599-5605.

92. Kane, R. S.; Cohen, R. E.; Silbey, R. *Chemistry of Materials* **1996,** 8, (8), 1919-1924.

93. Sohn, B. H.; Cohen, R. E. *Chemistry of Materials* **1997,** 9, (1), 264-269.

94. Il Yoo, S.; An, S. J.; Choi, G. H.; Kim, K. S.; Yi, G. C.; Zin, W. C.; Jung, J. C.; Sohn, B. H. *Advanced Materials* **2007,** 19, (12), 1594-+.

95. Gross, M.; Maskos, M. *Polymer* **2005,** 46, (10), 3329-3336.

96. Gao, H.; Jones, M. C.; Tewari, P.; Ranger, M.; Leroux, J. C. *Journal of Polymer Science Part a-Polymer Chemistry* **2007,** 45, (12), 2425-2435.

97. Gao, H.; Jones, M. C.; Chen, J.; Prud'homme, R. E.; Leroux, J. C. *Chemistry of Materials* **2008,** 20, (9), 3063-3067.

98. Jungmann, N.; Schmidt, M.; Ebenhoch, J.; Weis, J.; Maskos, M. *Angewandte Chemie-International Edition* **2003,** 42, (15), 1714-1717.

99. Ballou, W. R.; Reed, J. L.; Noble, W.; Young, N. S.; Koenig, S. *Journal of Infectious Diseases* **2003,** 187, (4), 675-678.

100. O'Hagan, D. T.; Wack, A.; Podda, A. *Clinical Pharmacology & Therapeutics* **2007,** 82, (6), 740-744.

101. Rizvi, S.; Camci, C.; Yong, Y.; Parker, G.; Shrago, S.; Stokes, K.; Wright, H.; Sebastian, A.; Gurakar, A. *Transplantation Proceedings* **2006,** 38, (9), 2993-2995.

102. Dawson, L. A.; Guha, C. *Cancer Journal* **2008,** 14, (2), 111-116.

103. Johnson, N. P.; Kwok, R.; Stewart, A. W.; Saththianathan, M.; Hadden, W. E.; Chamley, L. W. *Human Reproduction* **2007,** 22, (11), 2857-2862.

104. Hagen, A. J.; Hatton, T. A.; Wang, D. I. C. *Biotechnology and Bioengineering* **2006,** 95, (2), 285-294.

105. Liu, Y.; Dong, X. Y.; Sun, Y. *Separation and Purification Technology* **2007,** 53, (3), 289-295.

106. Liu, Y.; Dong, X. Y.; Sun, Y. *Journal of Colloid and Interface Science* **2006,** 297, (2), 805-812.

107. Liu, Y.; Dong, X. Y.; Sun, Y. *Biochemical Engineering Journal* **2006,** 28, (3), 281-288.

108. Liu, Y.; Dong, X. Y.; Sun, Y. *Journal of Colloid and Interface Science* **2005,** 290, (1), 259-266.

109. Hebbar, H. U.; Sumana, B.; Raghavarao, K. S. M. S. *Bioresource Technology* **2008,** 99, (11), 4896-4902.

110. Hebbar, H. U.; Raghavarao, K. S. M. S. *Process Biochemistry* **2007,** 42, (12), 1602-1608.

111. Goto, M.; Ono, T.; Nakashio, F.; Hatton, T. A. *Biotechnology and Bioengineering* **1997,** 54, (1), 26-32.

112. Sugiura, S.; Ichikawa, S.; Sano, Y.; Nakajima, M.; Liu, X. Q.; Seki, M.; Furusaki, S. *Journal of Colloid and Interface Science* **2001,** 240, (2), 566-572.

113. Ichikawa, S.; Sugiura, S.; Nakajima, M.; Sano, Y.; Seki, M.; Furusaki, S. *Biochemical Engineering Journal* **2000,** 6, (3), 193-199.

114. New, R. R. C.; Kirby, C. J. *Advanced Drug Delivery Reviews* **1997,** 25, (1), 59-69.

115. Jones, M. C.; Tewari, P.; Blei, C.; Hales, K.; Pochan, D. J.; Leroux, J. C. *Journal of the American Chemical Society* **2006,** 128, (45), 14599-14605.

116. Qu, S.; Zhang, X. W.; Gao, Y.; You, J. B.; Fan, Y. M.; Yin, Z. G.; Chen, N. F. *Nanotechnology* **2008,** 19, (13), -.

117. Mossmer, S.; Spatz, J. P.; Moller, M.; Aberle, T.; Schmidt, J.; Burchard, W. *Macromolecules* **2000,** 33, (13), 4791-4798.

118. Miller, A. C.; Bennett, R. D.; Hammond, P. T.; Irvine, D. J.; Cohen, R. E. *Macromolecules* **2008,** 41, (5), 1739-1744.

119. Chan, S. C.; Kuo, S. W.; Lu, C. H.; Lee, H. F.; Chang, F. C. *Polymer* **2007,** 48, (17), 5059-5068.

120. Yang, D. Q.; Xiong, Y. Q.; Guo, Y.; Da, D. A.; Lu, W. G. *Journal of Materials Science* **2001,** 36, (1), 263-267.

121. Legleiter, J.; DeMattos, R. B.; Holtzman, D. M.; Kowalewski, T. *Journal of Colloid and Interface Science* **2004,** 278, (1), 96-106.

122. Miller, A. C. Amphiphilic Block Copolymer Micelles: Creation of Functional Nanocavities and Thier use as Nanocontainers for Controlled Release. Massachusetts Institute of Technology, Cambridge, In Preparation.

123. Lee, D.; Gong, Y. C.; Teraoka, I. *Macromolecules* **2002,** 35, (18), 7093-7099.

124. Tonelli, A. E. *Macromolecules* **1992,** 25, (26), 7199-7203.

125. Jones, A. A.; Stockmayer, W. H.; Molinari, R. J. *Journal of Polymer Science Part C-Polymer Symposium* **1976**, (54), 227-235.

126. Zhang, L. F.; Barlow, R. J.; Eisenberg, A. *Macromolecules* **1995,** 28, (18), 6055-6066.

127. Cogan, K. A.; Gast, A. P.; Capel, M. *Macromolecules* **1991,** 24, (24), 6512-6520.

128. Colombani, O.; Ruppel, M.; Burkhardt, M.; Drechsler, M.; Schumacher, M.; Gradzielski, M.; Schweins, R.; Muller, A. H. E. *Macromolecules* **2007,** 40, (12), 4351-4362.

129. Mcconnell, G. A.; Gast, A. P.; Huang, J. S.; Smith, S. D. *Physical Review Letters* **1993,** 71, (13), 2102-2105.

130. Moffitt, M.; Yu, Y. S.; Nguyen, D.; Graziano, V.; Schneider, D. K.; Eisenberg, A. *Macromolecules* **1998,** 31, (7), 2190-2197.

131. Schillen, K.; Yekta, A.; Ni, S. R.; Farinha, J. P. S.; Winnik, M. A. *Journal of Physical Chemistry B* **1999,** 103, (43), 9090-9103.

132. Brown, D. S.; Dawkins, J. V.; Farnell, A. S.; Taylor, G. *European Polymer Journal* **1987,** 23, (6), 463-467.

133. Mcconnell, G. A.; Lin, E. K.; Gast, A. P.; Huang, J. S.; Lin, M. Y.; Smith, S. D. *Faraday Discussions* **1994,** (98), 121-138.

134. Park, S. Y.; Chang, Y. J.; Farmer, B. L. *Langmuir* **2006,** 22, (26), 11369-11375.

135. Cui, H.; Hodgdon, T. K.; Kaler, E. W.; Abezgauz, L.; Danino, D.; Lubovsky, M.; Talmon, Y.; Pochan, D. J. *Soft Matter* **2007,** 3, (8), 945-955.

136. Danino, D.; Gupta, R.; Satyavolu, J.; Talmon, Y. *Journal of Colloid and Interface Science* **2002,** 249, (1), 180-186.

137. Hameed, N.; Guo, Q. P. *Polymer* **2008,** 49, (4), 922-933.

138. Paradkar, V. M.; Dordick, J. S. *Biotechnology and Bioengineering* **1994,** 43, (6), 529-540.

139. Hamilton, J. A.; Cistola, D. P. *Proceedings of the National Academy of Sciences of the United States of America* **1986,** 83, (1), 82-86.

140. Li, Y.; Jiang, H. L.; Zhu, K. J. *Journal of Materials Science-Materials in Medicine* **2008,** 19, (2), 827-832.

141. Yoo, H. S.; Choi, H. K.; Park, T. G. *Journal of Pharmaceutical Sciences* **2001,** 90, (2), 194-201.

142. Dai, W. G.; Dong, L. C. *International Journal of Pharmaceutics* **2007,** 336, (1), 58-66.

143. Powers, M. E.; Matsuura, J.; Brassell, J.; Manning, M. C.; Shefter, E. *Biopolymers* **1993,** 33, (6), 927-932.

144. Meyer, J. D.; Manning, M. C. *Pharmaceutical Research* **1998,** 15, (2), 188-193.